

**A NEUTRON MEASUREMENT SYSTEM DESIGN  
FOR PULSED TRIGA REACTOR EXPERIMENT  
AT TEXAS A&M UNIVERSITY**

A Thesis

Submitted to the Faculty of Graduate Studies and Research

In Partial Fulfillment of the Requirements

For the Degree of

Doctor of Philosophy

in

Electronic Systems Engineering

University of Regina

By

Sophit Pongpun

Regina, Saskatchewan

May, 2016

Copyright 2016: S. Pongpun

**UNIVERSITY OF REGINA**  
**FACULTY OF GRADUATE STUDIES AND RESEARCH**  
**SUPERVISORY AND EXAMINING COMMITTEE**

Sophit Pongpun, candidate for the degree of Doctor of Philosophy in Electronic Systems Engineering, has presented a thesis titled, ***Neutron Measurement System Design for Pulsed Triga Reactor Experiment at Texas A&M University***, in an oral examination held on April 25, 2016. The following committee members have found the thesis acceptable in form and content, and that the candidate demonstrated satisfactory knowledge of the subject material.

|                    |  |
|--------------------|--|
| External Examiner: | Dr. Anthony Waker, University of Ontario Institute of Technology |
| Co-Supervisor:     | Dr. Thomas Conroy, Electronic Systems Engineering                |
| Co- Supervisor:    | Dr. Christine Chan, Software Systems Engineering                 |
| Committee Member:  | Dr. Esam Hussein, Faculty of Engineering & Applied Science       |
| Committee Member:  | Dr. Paul Laforge, Electronic Systems Engineering                 |
| Committee Member:  | Joe M. Toth, Electronic Systems Engineering, Adjunct*            |
| Committee Member:  | Dr. George Lolos, Department of Physics                          |
| Chair of Defense:  | Dr. Andrew Wee, Department of Chemistry and Biochemistry         |

\*Not present at defense

## ABSTRACT

This thesis focuses on designing, building, and analyzing a neutron detection system to measure neutron fluxes of a TRIGA reactor at Texas A&M University to verify newly developed simulation codes. Such a system must be designed to cover a wide range of neutron fluxes in transient power surges (up to  $10^{15}$  neutrons/cm<sup>2</sup>/s, lasting 20 to 50 ms) and in steady-state operations ( $10^{13}$  neutrons/cm<sup>2</sup>/s at full power of one megawatt). The size of the detector is limited to a maximum of 9.525 mm outer diameter including housing.

The detection system consisted of slow neutron detectors, associated electronics, data acquisition and storage equipment, and an analysis software. The detector used boron-10 to capture slow neutrons, generating charged particles within an ionization chamber filled with air. Due to the low Q-value of the reaction, a high gain charge-sensitive preamplifier, which was a part of a miniature 16.9 mm x 298.5 mm electronic package, was placed within 1.7 m of the detector to minimize noise level. The preamplifier was designed to offer pulse mode, current mode, and high voltage current mode of operation. Experimental data were acquired at 20 MHz using a solid-state drive for data storage and were subjected to 250 MHz for up to eight-hour continuous operation using an array of five three-TB hard drives. Data analysis software was programmed using MATLAB. In addition to analysis using the shaping amplifier's output, an algorithm to generate a radiation pulse from the directly digitized preamplifier signal was proposed and tested with test pulses simulating neutron events.

The detection system was tested with isotopic sources and in a dry tube located near the TRIGA reactor. The latter showed an increase in the number of gamma events with the reactor power, whereas the number of neutron events was also proportional to the power. In addition, a trial run of in-core measurements was performed. The results suggested that high gamma radiation present in the core interfered with the neutron signal. Suggestions was made for modification of the mechanical assembly of the system, compensation for gamma signals, and additional tests to improve analysis of the neutron signal.

## **ACKNOWLEDGEMENTS**

I first would like to express my deepest gratitude to my supervisor, Dr. Tom Conroy, for his expertise, understanding, and endless support throughout my Ph.D. study. His patience and guidance helped me learn and overcome challenges in many difficult situations. I could never ask for a better mentor.

Besides my supervisor, I would like to acknowledge my co-supervisor and my thesis committee for their advice that helps me focus on my study and widen my perspective. I would like to thank Dr. Esam Hussein for his time and efforts to guide me in the right direction. I am also grateful to Dr. Leslie Braby for his immense knowledge and skills and Dr. Marvin Adams for the great opportunity and support he has provided. My very special thank goes to Jan Vermaak for his time, insights, and continuous assistance in all the experiments and research. The project would not be possible without their invaluable support.

I would like to acknowledge the Faculty of Graduate Studies and Research and the Faculty of Engineering and Applied Science of the University of Regina for funding that allowed me to contribute more time to my studies. This research is also being performed using funding received from the DOE Office of Nuclear Energy's Nuclear Energy University Programs.

Last but not least, I would like to thank my family who always encouraged and supported me to pursue a higher education. I could not have done this without them.

## **POST DEFENSE ACKNOWLEDGEMENT**

I would like to acknowledge the external examiner, Dr. Anthony Waker, for his time and advice that broaden my knowledge and greatly help improve my work.

## **DEDICATION**

I dedicate my thesis to my parents who always love and support me unconditionally. They are the reason why I am who I am today. I could not say thank you enough times. I also would like to dedicate this work to my special friends who have always been there for me whenever I need. Even though I have not mentioned their names, I am certain they know who they are and how important they are to me. They are not just my friends but a part of my family. I really could not have done this without them.

# TABLE OF CONTENTS

|   |     |
|---|-----|
| ABSTRACT .....  | i   |
| ACKNOWLEDGEMENTS.....                                     | iii |
| POST DEFENSE ACKNOWLEDGEMENT .....                        | iv  |
| DEDICATION .....  | v   |
| TABLE OF CONTENTS .....                                   | vi  |
| LIST OF TABLES .....                                      | x   |
| LIST OF FIGURES .....                                     | xi  |
| 1 INTRODUCTION.....                                       | 1   |
| 1.1 Research objectives .....                             | 1   |
| 1.2 Scope of the research .....                           | 3   |
| 1.3 System requirement .....                              | 3   |
| 2 BACKGROUND.....   | 5   |
| 2.1 NSC's TRIGA reactor .....                             | 5   |
| 2.1.1 Support structure for the in-core detector .....    | 7   |
| 2.1.2 Activation data.....                                | 8   |
| 2.2 Neutron detection.....                                | 8   |
| 2.2.1 Neutron detectors in the nuclear reactor.....       | 8   |
| 2.2.2 Neutron detection mechanism.....                    | 9   |
| 2.2.3 Neutron detectors.....                              | 11  |
| 2.2.3.1 Boron-loaded or lithium-loaded scintillator ..... | 11  |
| 2.2.3.2 Boron-lined gas-filled detector .....             | 13  |
| 2.2.3.3 Fission chambers.....                             | 16  |

|         |   |    |
|---------|---|----|
| 2.2.3.4 | Boron trifluoride (BF <sub>3</sub> ) detectors..... | 17 |
| 2.3     | Detector electric circuit.....                      | 18 |
| 2.4     | Modes of operation.....                             | 19 |
| 2.4.1   | Pulse mode.....                                     | 19 |
| 2.4.2   | Current mode.....                                   | 21 |
| 2.5     | Gamma-ray discrimination.....                       | 21 |
| 2.6     | Microphonic noise.....                              | 22 |
| 3       | DETECTION SYSTEM DESIGN.....                        | 24 |
| 3.1     | Slow neutron detector.....                          | 24 |
| 3.1.1   | Geometry of the detectors.....                      | 31 |
| 3.2     | Electronic circuits.....                            | 34 |
| 3.2.1   | Preamplifier.....                                   | 38 |
| 3.2.1.1 | Modes of operation.....                             | 41 |
| 3.2.1.2 | Expected dynamic range of neutron fluxes.....       | 48 |
| 3.2.2   | Shaping amplifier.....                              | 51 |
| 3.2.3   | Test pulse generator.....                           | 52 |
| 3.2.4   | Microcontroller.....                                | 52 |
| 3.2.5   | Communication circuit.....                          | 53 |
| 3.2.6   | Power supply.....                                   | 53 |
| 3.2.7   | High voltage generator.....                         | 53 |
| 3.3     | Data acquisition unit.....                          | 53 |
| 3.3.1   | Data acquisition.....                               | 54 |
| 3.3.2   | Data storage.....                                   | 58 |
| 3.4     | Data analysis software.....                         | 60 |
| 4       | ANALYSIS OF PREAMPLIFIER SIGNAL.....                | 65 |

|       |   |     |
|-------|---|-----|
| 4.1   | Preamplifier output .....                                   | 65  |
| 4.2   | Line fitting .....  | 66  |
| 4.3   | Effects of microphonic noise .....                          | 67  |
| 4.4   | Digital filtering .....                                     | 70  |
| 4.5   | Filter variables .....                                      | 72  |
| 4.5.1 | Rise time of the preamplifier .....                         | 73  |
| 4.5.2 | Time for line/curve fitting on each side of the event ..... | 74  |
| 4.5.3 | Sampling frequency .....                                    | 77  |
| 4.5.4 | Length and type of filter .....                             | 79  |
| 4.6   | Design for real-time processing .....                       | 79  |
| 5     | PRELIMINARY EXPERIMENTAL RESULTS .....                      | 81  |
| 5.1   | Exposure to an alpha source .....                           | 81  |
| 5.2   | Exposure to a gamma source .....                            | 87  |
| 5.3   | Testing outside of the reactor core .....                   | 89  |
| 5.3.1 | Results at steady-state power of 10 kW .....                | 90  |
| 5.3.2 | Results at 10 kW and 50 kW .....                            | 91  |
| 5.3.3 | System inherent noise .....                                 | 98  |
| 5.4   | Conclusion .....  | 100 |
| 6     | IN-CORE MEASUREMENTS .....                                  | 102 |
| 6.1   | Mechanical assembly .....                                   | 103 |
| 6.2   | Installation process .....                                  | 107 |
| 6.3   | Test procedure .....  | 109 |
| 6.3.1 | Settings .....  | 109 |
| 6.3.2 | Procedure .....   | 110 |
| 6.4   | Results and discussion .....                                | 112 |

|     |  |     |
|-----|--|-----|
| 6.5 | Conclusion .....   | 119 |
| 7   | CONCLUSIONS .....  | 121 |
| 7.1 | Mechanical parts and assembly .....  | 122 |
| 7.2 | Gamma compensated detector .....   | 124 |
| 7.3 | Pulse height distribution of gamma events .....                            | 126 |
|     | REFERENCES.....  | 127 |
|     | APPENDIX A: Analysis of shaping amplifier output .....                     | 132 |
|     | APPENDIX B: Characterizing pulse height distribution of gamma events ..... | 136 |

## LIST OF TABLES

|  |    |
|--|----|
| Table 1 Nuclear reactions for thermal-neutron detection .....  | 10 |
| Table 2 Geometry and materials of the detectors used in the experiment in this thesis .  | 27 |
| Table 3 Specification of the parts of the detectors .....  | 32 |
| Table 4 Connections from the circuit to the detector and to the user's end. The first had two signals while the latter had five connections..... | 37 |
| Table 5 Filter coefficients $b_j$ for $N = 4, 8,$ and $16$ and $k = 2$ .....   | 72 |
| Table 6 Reactor power and modes of the system in the experiments outside of the reactor core .....   | 90 |
| Table 7 PX14400D2 settings for the test outside of the reactor core at 10 kW and 50 kW .....   | 92 |

## LIST OF FIGURES

|  |    |
|--|----|
| Figure 1 A photograph of the TRIGA reactor at the NSC .  | 6  |
| Figure 2 Diagram of the reactor core   | 7  |
| Figure 3 Pulse height spectrum from a boron-lined detector   | 13 |
| Figure 4 The equivalent circuit of the ionization chamber and the preamplifier                                       | 18 |
| Figure 5 The voltage across the resistor when the time constant is larger than the charge collection time            | 20 |
| Figure 6 An aluminum pole consisting of a 0.9 m detector holder and a 9 m tube in which the electronics are located. | 26 |
| Figure 7 A photograph of detector A  | 27 |
| Figure 8 A sketch of the detector  | 31 |
| Figure 9 Possible paths of the reaction products (simplified to 2D)  | 33 |
| Figure 10 Spectrum of the detector by MCNP simulations   | 33 |
| Figure 11 Electronic circuit boards being assembled back to back   | 35 |
| Figure 12 Block diagram of the electronic system   | 36 |
| Figure 13 Example of the response of a neutron event.  | 39 |
| Figure 14 Simplified schematic of the charge-sensitive preamplifier with a feedback resistor reset                   | 40 |
| Figure 15 Outputs of the preamplifier when operating in pulse mode with unlatched reset                              | 42 |
| Figure 16 Outputs of the preamplifier and the shaping amplifier in response to a neutron event                       | 45 |
| Figure 17 A photograph of the Signatec PX14400D2 board   | 55 |

|   |    |
|---|----|
| Figure 18 Signatec scope application software screenshots .....   | 57 |
| Figure 19 The preamplifier, the digitally-filtered output, and the shaping amplifier output when the microphonic noise is present.....                              | 63 |
| Figure 20 Digitized preamplifier waveform in unlatched reset mode .....   | 66 |
| Figure 21 Preamplifier output to a test pulse when microphonic noise is present .....   | 68 |
| Figure 22 FWHM normalized by the maximum count versus the size of $N$ at sampling frequency of 1 MHz .....  | 76 |
| Figure 23 FWHM versus sampling frequencies for $t_a$ and $t_b$ of 32 $\mu$ s.....   | 78 |
| Figure 24 The alpha source, Am-241, was placed at two positions .....   | 83 |
| Figure 25 The output of the preamplifier and the shaping amplifier when the alpha particle travelled lengthwise inside of the detector.....                         | 84 |
| Figure 26 Pulse height distribution of the shaping amplifier output when the detector was exposed to the Am-241 alpha source .....                                  | 85 |
| Figure 27 The output of the preamplifier and the shaping amplifier when the alpha source was placed to emit the particle through the 2-mm hole of the detector..... | 86 |
| Figure 28 Pulse height distribution of the shaping amplifier output when the detector was exposed to the Am-241 alpha source .....                                  | 86 |
| Figure 29 The preamplifier output (a) when the gamma source was not present (b) when the detector was exposed to the Cs-137 gamma source. ....                      | 88 |
| Figure 30 Result from the test outside of the reactor operating at 10 kW .....  | 91 |
| Figure 31 Shaping amplifier signals at 10 kW .....  | 93 |
| Figure 32 Shaping amplifier signals at 50 kW .....  | 94 |
| Figure 33 Pulse height distribution at 10 kW and 50 kW.....   | 95 |
| Figure 34 Reactor gamma spectrum from MCNP simulations .....  | 96 |

|   |     |
|---|-----|
| Figure 35 Comparison of the results at 10 kW and at 50 kW when scaled by a factor of 5<br>.....   | 97  |
| Figure 36 Pulse height distribution of the test at 10 kW with the test pulse generator<br>turned on. ....                                       | 99  |
| Figure 37 Pulse height distribution of the test at 50 kW with the test pulse generator<br>turned on. ....                                       | 100 |
| Figure 38 Reference diagram of the positions in the core .....  | 103 |
| Figure 39 The 0.91 m (36") tip in which the detector was located and the guide tube ..  | 105 |
| Figure 40 A custom-built input capacitor made from a small magnet wire, a Teflon<br>insulator, and a brass tube .....                           | 107 |
| Figure 41 Photographs showing the guide tube in the core of the detector .....  | 108 |
| Figure 42 Pulse height distribution at 50 W power at position 37 .....  | 113 |
| Figure 43 Pulse height distribution at 0 W power at position 37 .....   | 113 |
| Figure 44 Pulse height distribution when the detector was located at position 37, 31, 27,<br>23, and 19 .....                                   | 115 |
| Figure 45 Plot of the number of all the pulses with the height above 23000 ADC unit<br>versus the detector's location in the reactor core ..... | 116 |
| Figure 46 Plot of the number of pulses with the height above 37000, 38000, and 39000<br>ADC units versus the detector's location. ....          | 118 |
| Figure 47 Plot of the number of events versus the detector's location from experiments<br>and the simulation .....                              | 119 |
| Figure 48 Current and proposed cable connections.....   | 124 |
| Figure 49 A sketch of a conceivable gamma compensated detector .....  | 125 |
| Figure 50 The shaping amplifier output .....  | 133 |
| Figure 51 The spectrum of the shaping amplifier output .....  | 135 |

Figure 52 A Gaussian function overlaid on the top of the spectrum of the in-core measurement at position 27 .....137

Figure 53 The spectrum at position 27 after the Gaussian function is subtracted off....138

Figure 54 The spectrum of the detector from the MCNP simulation.....139

Figure 55 The reference point (point A) which is used in the calculation of  $n'_{exp}$ .....141

# 1 INTRODUCTION

This research focuses on the development of an experimental system to monitor steady-state and transient operations in the Testing, Research, Isotopes, General Atomics (TRIGA) reactor core at the Nuclear Science Center (NSC), Texas A&M University. The system is a part of a Nuclear Energy University Programs (NEUP) project titled “Phenomena-based Uncertainty Quantification in Predictive Coupled-Physics Reactor Simulations” [1]. It is important in a nuclear reactor to determine neutron-flux distributions and quantify their values and associated uncertainties. Flux distributions are typically determined by simulation of steady-state and transient reactor behaviour. However, simulation codes need to be verified by comparing the predictions against experimental results. This thesis concentrates on designing, building, and analyzing a system to measure the neutron flux of the TRIGA reactor in steady-state and transient operations. This system has to be able to provide information in a wide range of the neutron flux with high precision. Additionally, an in-core measurement system has to overcome many challenges including the small size of the research reactor, the limited space for a detector, the thermal-hydraulic disturbance which has to be within the safety parameters, and the high gamma flux that is present along with the neutron flux [2].

## 1.1 Research objectives

The paramount goal of the project is to create a system to obtain information about the operation of the TRIGA reactor at the NSC. The ultimate system is to consist of a neutron detector, electronic circuitry, a data acquisition and storage apparatus, and post-processing software. The detector is to respond primarily to slow neutrons, whose

energy is lower than 0.5 eV, because it is these neutrons that determine the reactor power. However, a detector placed in the core of a nuclear reactor is also exposed to high fluxes of fast neutrons and gamma rays which interfere with its response to slow neutrons. A detector produces electric charges that need to be processed with an electronic circuit, which includes a preamplifier, an amplifier, a high voltage generator, a communication circuit, and a microcontroller. This circuit can be tested with the aid of a pulse generator simulating detector signals. Data acquisition and storage equipment also needs to handle digitization of the detector output at high rate and store detected values acquired over a long period of time. This will allow further analysis of the large amount of data obtained from the experiment by post-processing software.

This experimental system is composed of several components, many of which can operate independently as a standalone part or a subsystem. It is beneficial to design, construct, and test each component or subsystem separately before assembling them into the complete system. This provides an opportunity to optimize components' functions, verify operations, and make modifications without affecting other parts of the overall system. The focus of this thesis is the development of the neutron detector and the electronic circuitry. The data acquisition and storage unit as well as the post-process software are set-up in the simplest way to evaluate the capability of the system. This thesis focuses on preliminary study of the design with the following objectives:

- to check whether the design of the system is fundamentally sound
- to establish the baseline capabilities of the system for slow neutron detection
- to identify the modifications required for the system to work in the intended environment
- to investigate and troubleshoot potential issues that could exist within the

ultimate system.

## **1.2 Scope of the research**

To accomplish the objectives stated in section 1.1, the scope of the research includes:

- constructing a subsystem consisting of a neutron detector and electronic circuitry,
- setting up simple data acquisition and storage equipment necessary to record the data for system evaluation,
- developing basic analysis methodologies to preliminarily process the data,
- testing the subsystem and collecting the experimental data when placing the detector in the environment similar to the reactor core,
- addressing the design and analysis problem and determining the ability and limitation of the detector and the electronics, and
- providing a conclusion regarding the changes that need to be made to the subsystem after a trial test in the core of the reactor.

## **1.3 System requirement**

The key requirements of the system include the following:

- the detector must be small in size to meet the physical obligation of the in-core device (the diameter of the detector and its housing cannot exceed 9.525 mm),
- the design of the detector should be simple to build in order that the design can be replicated with other materials to provide more information for the simulation comparison purpose,
- the speed of data acquisition must be high enough to provide acceptable time

resolution, and

- the system should be compatible with other experiments at the NSC (with minimal modification) although the system is mainly developed as an in-core measurement device.

## **2 BACKGROUND**

### **2.1 NSC's TRIGA reactor**

TRIGA stands for Testing, Research, Isotopes, General Atomics. The TRIGA reactor was originally designed for use in education, training, and research programs, but the reactor was expanded for use in medical and industrial applications [3]. The reactor is an excellent source for neutron and gamma exposure for many researches and applications, especially neutron irradiation to produce a radioactive isotope [4], [5].

The TRIGA reactor at the NSC, as shown in the photograph of Figure 1, is a pool-type reactor. The core, which consists of cylindrical fuel elements, is immersed in an open pool of water. The reactor is capable of operating at a maximum steady-state power level of one megawatt (1 MW) [4]. The thermal neutron flux provided by the reactor ranges from  $1 \times 10^{12}$  neutrons/cm<sup>2</sup>/s to  $1.4 \times 10^{13}$  neutrons/cm<sup>2</sup>/s, depending on the location in the core [4]. The gamma dose of  $2 \times 10^5$  Gy/hr ( $2 \times 10^7$  rad/hr) can be expected on the reactor face at this power level [4].



Figure 1 A photograph of the TRIGA reactor at the NSC (in original color).

Jan Vermaak, Manager of Engineering at the NSC, provided some information about the reactor [6]. The core consists of fuel rods and six control rods. Uranium zirconium hydride (UZrH) is used as the fuel. The control rods are composed of four shim rods, one transient rod, and one regulating rod. These rods are arranged in bundles of four as shown in Figure 2. The location of each group in the core is identified by the column number starting from 1 and the row character starting from A. At the crossing point between each row and each column there is a small diamond gap into which a sample, or in this work a detector, can be inserted for exposure to radiation.

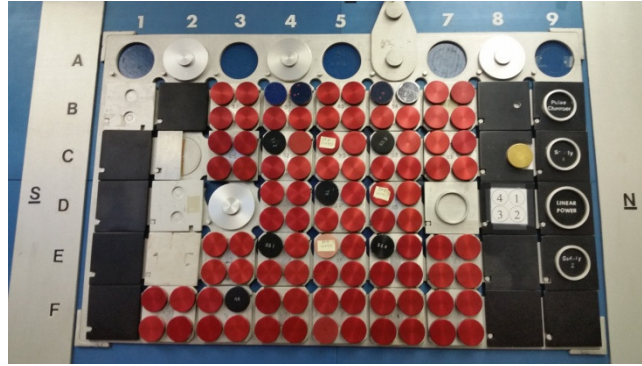


Figure 2 Diagram of the reactor core (in original color). The core consists of the fuel rods and six control rods.

### 2.1.1 Support structure for the in-core detector

In order to place a detector in the desired location between the rods of the core, the system needs a mechanical support which is stable but minimally disturbs the operation of the core. The detector must fit into the support structure which was modeled, designed, and built by the NSC staff as described in [2], [7]. The fundamental design concept is to have a supporting structure of a cylindrical geometry and leave a space between the structure and the fuel rods no less than the space between the rods themselves. The resulting design is a guide tube with a diameter of 12.7 mm (0.50”), which is to be centered in the space between the rod bundles. The tube is to be held in place by the support foot in the bottom of the core. The top section has a support leg to lock the structure on the top of the rod bundle tool hooks. The tube contains several holes along its length to let the coolant flow in and out. A photograph of the support structure is shown in Figure 39 in Chapter 6.

This support structure perturbs the reactor in terms of neutron fluxes, power distribution, and reactivity worth. Therefore, the neutronic design was modeled by Jan Vermaak by

Monte Carlo N-Particle (MCNP) code to study these effects [2]. The thermal-hydraulic design was modeled using the STAR-CCM+ and RELAP5/MOD3.3 code to determine changes in cladding temperature and in the minimum departure from nucleate boiling ratio [2], [7]. Both the neutronic and thermal-hydraulic safety parameters are found within limits [2]. The simulations were validated by a number of qualification tests [2]. The details of these design aspects are described in [2], [7]. The detector is to be placed inside of this guide tube.

### **2.1.2 Activation data**

A few materials, such as gold foils and copper wires, were exposed to the radiation at select locations in the core [7]. The activation data can inform the steady-state flux in the core. There is a data pack available which includes the wire activation data [7]. Both the axial and semi-radial profiles of the flux are provided. Examples from two different locations, close to the center of the core and at the core's peripheral, are given in [7] showing the copper wire activation measurements of the count rate versus the distance from the center of the core in comparison with MCNP calculations. This information can be used as a first step in evaluating the system developed in this work for in-core measurements. The detector can be moved to different positions in the core to find the axial distribution of the steady-state flux, which can be compared to the wire activation data.

## **2.2 Neutron detection**

### **2.2.1 Neutron detectors in the nuclear reactor**

Slow neutron detectors in a reactor can be placed either in-core or out-of-core [8]. Out-of-core detectors monitor neutrons escaping the reactor, which can be related to overall

flux in the reactor core, and are located outside the reactors. More than one type of these sensors and operating modes may be used to cover different power ranges in the reactor. For example, routine monitoring in pressurized water reactors utilizes gas-filled proportional counters operating in pulse mode during the source start-up and in mean square voltage mode during the intermediate power range. When the reactor is at full operating power, the neutron flux is monitored by ionization chambers. On the other hand, in-core sensors, which are the focus of this research project, are placed within a nuclear reactor to provide information on the spatial and temporal variation of the neutron flux. Therefore, these sensors must be small in size and able to tolerate high flux of neutrons and gamma rays inside a nuclear reactor.

### **2.2.2 Neutron detection mechanism**

Radiation is detected from its interaction with detector materials [8]. Most radiation detectors interact with electric charges carried by charged particles through the coulomb force. Thus, uncharged radiations, which do not interact through the coulomb force, must first undergo some interactions to transfer their energy to charged particles. Gamma rays, which are neutral in electrical charge, interact with atomic electrons, freeing up from their bound state. On the other hand, neutrons, which are also neutral in charges, need typically to interact with nuclei of material to liberate charged particles. These secondary electrons or particles are then used to produce an electronically measurable detection signal.

There are several interactions that are useful for neutron detection. The usefulness of a particular interaction for detection depends on the value of its neutron cross section, which is a measure of the probability of neutron interaction with a material (express per

nucleus in a unit called “barn”, which is equal to  $10^{-28}$  m<sup>2</sup>). The cross section varies considerably with the energy of the incident neutron. Fast neutrons, whose energy is higher than 0.5 electron volt (eV), are more likely to undergo elastic scattering more than a nuclear reaction. In contrast, slow neutrons with energy below 0.5 eV have higher cross section for nuclear reactions.

Neutron detection in a reactor focuses mostly on slow neutrons because they are responsible for fission in water-moderated reactors, such as the TRIGA reactor, in which the fast neutron accompanying fission are slowed-down to the thermal energy. In order to detect these thermal neutrons, a material with a high neutron-absorption cross section are needed. Table 1 lists the materials most suited for thermal-neutron detection. The Q-value in this table indicates the energy released in the interaction, which is shared between the charged particles resulting from the interaction, in inverse proportionality to their mass. The cross section in the table is the absorption cross section for thermal neutrons. The energy dependent cross section can be found in [9].

Table 1 Nuclear reactions for thermal-neutron detection [8], [10]

| Material      | Reaction  | Q-value (MeV) | Cross sections (barns) |
|---------------|---|---------------|------------------------|
| Boron-10      | $^{10}_5B + \frac{1}{0}n \xrightarrow{(94\%)} \frac{7}{3}Li + \frac{4}{2}\alpha$  | 2.310         | 3835                   |
|               | $^{10}_5B + \frac{1}{0}n \xrightarrow{(6\%)} \frac{7}{3}Li^* + \frac{4}{2}\alpha$ | 2.792         |                        |
| Lithium-6     | $\frac{6}{3}Li + \frac{1}{0}n \rightarrow \frac{3}{1}H + \frac{4}{2}\alpha$       | 4.78          | 940                    |
| Helium-3      | $\frac{3}{2}He + \frac{1}{0}n \rightarrow \frac{3}{1}H + \frac{1}{1}p$            | 0.764         | 5333                   |
| Uranium-235   | Various fission fragments   | 200 (approx.) | 680.9                  |
| Plutonium-239 | Various fission fragments   | 200 (approx.) | 1017.3                 |

One of the materials often used as a target is an isotope of boron, boron-10 (<sup>10</sup>B), due to its high cross section and its availability. Boron-10 makes up 20% of natural abundance

[10], and highly enriched  $^{10}\text{B}$  in gas form or solid form can be made from natural boron. A neutron-induced nuclear reaction in boron results in an alpha particle and a lithium nucleus, either in the excited state or in the ground state, emitted in opposite directions. This is represented by the (n,  $\alpha$ ) reaction which is expressed as [8], [11]:



The reaction energy or Q-value is 2.310 MeV and 2.792 MeV for excited and ground-state lithium nucleus, respectively. This is a large energy compared with the energy of a slow neutron (which is less than 0.5 eV). Therefore, the energy of the reaction products is dominated by the reaction energy. As a result, it is not possible to deduce the information about the energy of the incident neutron.

### 2.2.3 Neutron detectors

The charged particles produced in neutron detection are converted into electronic signals in gas-filled detectors, scintillators, or semiconductors [8], [11], [12]. The operation of a few detectors are summarized in this section.

#### 2.2.3.1 Boron-loaded or lithium-loaded scintillator

In a scintillation detector, the kinetic energy of charged particles is absorbed by the detector's material resulting in its excitation. To return to its original state, a light output is produced. Scintillators used in slow neutron detection are commonly loaded with boron or lithium to capture slow neutrons and produce charged particles. They are available in many forms including plastic, crystal, liquid, or glass scintillators [8]. One example of slow neutron scintillation detectors is a lithium glass fiber scintillator which is

capable of generating light output that can travel in its fiber as long as several meters [8]. This allows the detector to be coupled to a light sensor, which is always required to convert scintillation photons to an electrical output, located at some distance away from the detector.

Light sensors that are widely used with scintillation detectors are photomultiplier tubes or photodiodes. Although photomultiplier tubes are widely used in many applications, a newer technology of semiconductor photodiodes offers many advantages including better efficiency to create photoelectrons, smaller size, insensitivity to magnetic field, and resistance to mechanical vibration [8], [13]. One category of photodiodes is called a silicon photomultiplier (SiPM) or a multi-pixel photon counter (MPPC) which is an array of small-dimension photodiodes, each of which ideally responds to only one scintillation photon. In other words, each photodiode in the SiPM acts as a counter. Therefore, a number of total counts is then proportional to the number of scintillation photons. Many array sizes are commercially available ranging from as  $1 \times 1 \text{ mm}^2$  to  $6 \times 6 \text{ mm}^2$  [14].

One of the disadvantages of scintillation detectors is an ability to discriminate against gamma rays. A secondary electron from a gamma ray can deposit more energy in some scintillators, such as lithium iodide crystals, than in gas-filled detectors [8]. A pulse height resulting from an incident gamma ray can be as large as one from a neutron event. Therefore, gamma discrimination is more difficult. A size of the detector can be reduced to allow these gamma-induced electrons to deposit less energy before escaping the detector.

### 2.2.3.2 Boron-lined gas-filled detector

Boron-lined detectors use  $^{10}\text{B}$  in a solid form as a coating material on the inner wall of the detector chamber [11], [12]. The boron-neutron interaction occurs in the wall of the chamber. Since two reaction products are emitted in two opposite directions, only one product per interaction travels toward the inside of the gas-filled chamber and deposit its energy in the fill gas. The energy deposited by that reaction product ranges from zero to its full energy, which is 0.84 MeV and 1.47 MeV for an excited lithium recoil and an alpha particle, respectively. Figure 3 illustrates two separate ideal energy distributions for lithium recoil in the excited state and for the alpha particle and a combined ideal distribution. Because the nuclear reaction has equal probability to occur in any location in the detector walls, the distribution of the energy deposited by each product displays a rectangular shape. The combined distribution for a boron-lined detector then has a shape of a stair case.

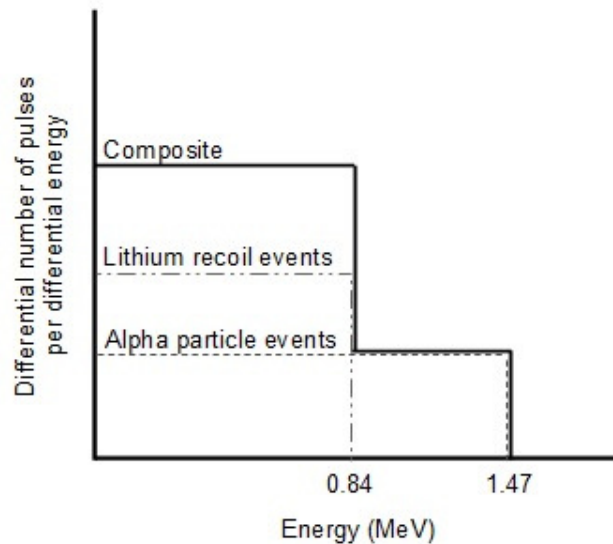


Figure 3 Pulse height spectrum from a boron-lined detector [8]

The efficiency of a boron-lined detector depends on the thickness of the coating which should be approximately the maximum range of the alpha particle emitted in the nuclear reaction. Additional thickness reduces the efficiency as it adds an extra layer the reaction products have to travel through in order to reach the fill gas.

The electric charges carried by charged particles, lithium recoils or alpha particles, interact with the electrons in gas molecules along their track through the coulomb force. Using the energy from the charged particle, the electron either elevates to a higher shell resulting in an excited molecule or ejects completely leading to an ionized molecule. Even though the excitation can be used to derive an output signal, boron-lined detectors are among the detectors whose output is based on the ionization created by charged particles. Ionization of a gas molecule results in an ion pair consisting of a positive ion and a free electron. As the energy required to create an ion pair, referred to as a  $W$ -value, only varies slightly with the type of gas and radiation and is very close to a constant of 25 to 35 eV, the number of ion pairs created by a charge particle is proportional to the energy deposited in the fill gas. However, there is some variation in this number and its fluctuation will set the statistical limit of the energy resolution of the detector.

The common geometry of the detector consists of an anode wire in the middle of a hollow cylindrical cathode shell filled with air or a fill gas, such as hydrogen [12] or argon with a small fraction of carbon dioxide [11]. When the electric field is applied to the electrodes, the electrostatic force accelerates the free electrons and the positive ions toward the anode and cathode, respectively. An electrical signal is then generated through the collection of the charges. The drift velocity of the ions depends not only on

the electric field strength and the gas pressure but also on the mobility parameter ( $\mu$ ) of the charged particles. Although the mobility varies with gas species, the mobility value of the electron is typically much higher, approximately three orders of magnitude, than that of the positive or negative ion [8]. Therefore, the ion transit time is significantly longer. In general, the collection time for ions and electrons in typical detector dimensions are in the worst case on the order of milliseconds and microseconds, respectively [8].

Positive ions and free electrons may collide with one another or with neutral gas atoms or molecules in their path to the electrodes. The collision possibly leads to charge transfer, electron attachment, or recombination [8]. The charge transfer occurs when a positive ion collides with a neutral gas atom or molecule. The positive ion becomes a neutral atom when the electron is transferred from the gas atom or molecule which in turn carries a positive charge. On the other hand, when a free electron collides with a neutral gas atom or molecule, there is a possibility that the electron will attach to the atom or molecule and form a negative ion. Another significant collision effect is recombination which takes place either when an electron collides with a positive ion and recombine to a neutral atom or molecule, or when a positive ion captures an extra electron from the negative ion which neutralizes both ions. As a result, the recombination can affect the charge collection and cause some losses. As the irradiation rate is higher, the probability of recombination among different events increases. The high electric field is therefore applied in order to minimize the charge collection time and reduce the losses due to the recombination.

When the electric field reaches a threshold value, gas multiplication occurs in the detector. The electrons originally generated by the lithium recoils or alpha particles are

accelerated by the field. When they gain enough energy, collision between these electrons and other neutral gas molecules creates additional ion pairs which also drift by the field applied to the detector. They may collide with other gas molecules and generate more ion pairs. Therefore, with a sufficiently high applied voltage to the detector, the number of ion pairs created by a neutron incident is multiplied and forms a chain reaction. This mechanism results in a higher output signal than a normal ionization chamber. The detector is referred to as a proportional counter because a number of charges collected at the electrodes are proportional to the number of original charges prior to the chain reaction.

#### *2.2.3.3 Fission chambers*

Fission chambers operate in the same mechanism as a boron-lined detector, except that they are lined with a fissile material such as uranium-235 ( $^{235}\text{U}$ ) instead of boron. The nuclear reaction results in fission fragments with much larger amount of energy (Q-value of the reaction is about 200 MeV) compared with the boron-neutron interaction. Therefore, fission chambers are usually operated as ionization chambers with no gas multiplication required since they already produce a large enough output signal. In-core fission chambers are commercially available [15].

Miniature fission chambers are used in in-core monitoring of research reactors [16], [17], where such a detector is constructed in a parallel plate geometry consisting of two small discs as the electrodes. One of the discs is lined with the fission material. The disc diameter and the separation between them can be as small as 1 mm and 0.5 mm, respectively. The detector is filled with Argon. The detector is able to measure the neutron flux in the pulse mode linearly ranging from  $4 \times 10^5$  neutrons/cm<sup>2</sup>/s to  $8 \times 10^{12}$

neutrons/cm<sup>2</sup>/s [17]. MCNP simulations in [17] shows that such a detector has low sensitivity to background gamma rays because the energy deposited by a neutron is sufficiently high to keep a large signal to background ratio (close to 10<sup>4</sup> eV higher for the less than 1 mm chamber).

Fissile materials are usually unstable and radioactive. Licensing and safety issues of these materials make them less than ideal to obtain and work with in a research lab. Therefore, the use of such detector was not considered in the work, but it is a candidate for future development. Its large reaction energy for neutron interactions makes discrimination against gamma-ray background radiation relatively easy.

#### *2.2.3.4 Boron trifluoride (BF<sub>3</sub>) detectors*

BF<sub>3</sub> detectors are one of the gas-filled detectors commonly used in slow neutron detection [8], [11], [12]. BF<sub>3</sub> serves both as a target material for neutron-to-charged particle conversion, due to its boron content, and as the ionizing gas, typically as a proportional counter. Since the interaction happens inside of the chamber, both of the charged particles from the boron-neutron interaction, lithium recoils and alpha particles, are released and deposit their energy in the fill gas.

There are some disadvantages of BF<sub>3</sub> detectors compared with boron-lined detectors. Because the target for conversion process in BF<sub>3</sub> tubes is in the gas form, the detectors operate at the high gas pressure so as to improve the detection efficiency. Higher pressure and higher operating voltage lead to a larger gamma-ray signal compared with a neutron signal; therefore, BF<sub>3</sub> detectors are more sensitive to gamma rays [11]. Additionally, the thicker wall is required to withstand the pressure. BF<sub>3</sub> is also toxic and

not compatible with aluminum which is normally a common choice of material for detector construction. Also, boron-lined detectors provide faster timing and better chemical resistance in high gamma-ray environment [8].

### 2.3 Detector electric circuit

A detector is almost always electronically connected to a preamplifier placed as close to the detector as possible to promptly amplify the detected electronic signal and avoid its degradation in subsequent transmission cables. The equivalent electric circuit for a detector (say an ionization chamber) and the associated preamplifier is shown in Figure 4. The circuit consists of the input resistance of the measuring circuit ( $R$ ) and the equivalent capacitance of the detector and the measuring circuit ( $C$ ). The value of  $C$  is equal to a sum of the detector capacitance, the capacitance of the short cable connecting the detector to the preamplifier, and the input capacitance of the measuring circuit. The input resistance and capacitance in the preamplifier are varied for two different modes of operation which are discussed next. A voltage source ( $V_0$ ) is connected to the detector or the ionization chamber to provide an electric field for charge collection.

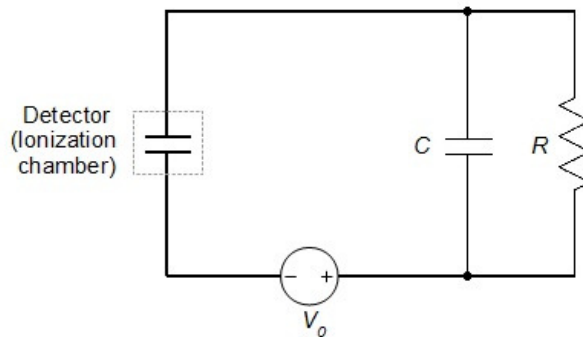


Figure 4 The equivalent circuit of the ionization chamber and the preamplifier [8]

The preamplifier provides the output voltage which is proportional to the number of charges collected from the detector. Typically, this output is small and has a long tail which is not suitable to be monitored directly. For example, if two events occur close in time, the output from the second event will lay on the top of the tail of the first output [8]. Therefore, the preamplifier is usually connected to a shaping amplifier circuit which, as its name suggests, performs pulse shaping and amplification [8], [12]. The shaping amplifier raises the level of the original preamplifier output and transforms its shape to a pulse that is more appropriate for the subsequent pulse processing circuit.

## **2.4 Modes of operation**

### **2.4.1 Pulse mode**

When operating in pulse mode, the detector records and provides information about each radiation event individually. The voltage across the input resistance  $R$  in Figure 4, referred to as  $V_R$ , serves as a basic signal being monitored by the measuring circuit.

When no electric charge is present in the detector, the voltage  $V_R$  is zero and the voltage across the ion chamber is equal to the source voltage  $V_0$ . After a radiation event, ion pairs are formed and drift to the electrodes due to the electric field. During this charge collection time, the chamber voltage decreases below  $V_0$ , and the current is integrated on the capacitor resulting in the increase in the value of  $V_R$ . Due to higher mobility of electrons than ions, their transit time is much shorter. In other words, electrons usually arrive at the electrode first, which quickly raise the voltage at the beginning of the charge collection period. Slower-drifting ions, which reach the electrode sometime later, gradually increase the voltage. This voltage reaches its maximum value when all the

electric charges are collected at the corresponding electrodes. During the time before the next radiation event, the capacitance discharges through the resistance. As a result,  $V_R$  slowly decreases to zero and the voltage across the ion chamber returns to the original source voltage. The time required for the voltage across the resistor to reach its maximum value depends on the charge collection time and does not rely on the parameter in the measuring circuit. In contrast, the time required for the capacitor to fully discharge depends on the time constant of the measuring circuit,  $\tau = RC$ . In normal operation, the time constant is larger than the charge collection time. Therefore, a single pulse is produced per one radiation event as illustrated in Figure 5.

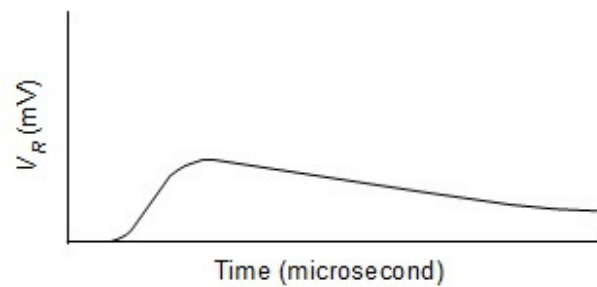


Figure 5 The voltage across the resistor when the time constant is larger than the charge collection time [8]

As the tail of the signal can be very long (to increase the signal-to-noise ratio,  $R$  is chosen as large as possible), a special capacitor-resistor and resistor-capacitor (CR-RC) shaping circuit is used to sharpen and narrow each radiation event. Typical shaping times are on the order of microseconds [8], [18]. Although pulse mode operation provides information about single radiation events, the shaping times restrict the use of this mode to low neutron flux environments. As the flux increases, the time between events becomes shorter and the possibility of the pulse overlap or pulse pile-up

increases. Therefore, the current mode is usually adopted in high event rates.

The amplitude of the pulse is directly proportional to the charges produced within the detector or  $V_{R_{max}} = Q/C$  where  $Q$  is the total charge generated from the radiation. In pulse mode, every voltage pulse above a set threshold is a detected neutron. The total counts over a specific time is then the neutron detection rate.

#### **2.4.2 Current mode**

In the current mode, the value of the input resistance  $R$  in Figure 4 is made significantly lower than that in the pulse mode allowing the current produced in the charge collection time to flow through. According to ohm's law, the current is then converted to voltage which serves as the basic signal for the measurement.

The measured current is an average value of the individual current pulses generated from many radiation interactions occurring over a response time. Therefore, this average current depends on the interaction rate and the charges generated per interaction, and responds slowly to the rapid changes in the event rate. Even though information about each radiation event is not preserved, the current mode is suitable for the operation in high event rate where the possibility of pulse pile-up is strong in the pulse mode. In the current mode, the neutron detection rate is determined by the ratio between the measured current and the average charge collected per neutron.

#### **2.5 Gamma-ray discrimination**

Gamma rays are usually present together with neutrons. A nuclear fission not only immediately releases gamma rays along with neutrons, but its fission products also

usually emits gamma rays [19]. Additionally, the detector itself can be a source of gamma rays from a decay process of an excited lithium recoil produced in the boron-neutron interaction [12]. Regardless the sources, the interaction of gamma rays usually takes place in a detector's wall [11] and generates secondary electrons which may also cause ionization in the fill gas. However, because these electrons generally have low stopping power, they can reach the opposite detector wall after depositing only part of their energy. Consequently, gamma-ray radiation gives rise to low-amplitude pulses. If the gamma-ray flux is not significantly high, pulses produced from the background gamma rays can be eliminated by simple amplitude discrimination in pulse mode of operation. However, when the detector operates in current mode, these gamma ray pulses can make a contribution to the average current and cannot be discriminated against. In that case, a gamma compensated detector is needed. This is especially true in boron detectors which has a Q-value two orders of magnitude lower than that of fission chambers.

## **2.6 Microphonic noise**

Microphonic noise is a low frequency noise caused by mechanical vibrations that pass on to the output of a detector and consequently the input of its preamplifier. The vibration leads to fluctuations in the input capacitance and results in a low frequency signal on which the output signal is superimposed. Some detectors are more sensitive to microphonic noise than others. It can become a serious issue if the pulse is small and is hidden in the large magnitude of noise. Although analog pulse shaping is a common method in radiation instrument to reduce the effect of the microphonic noise [20], the noise may not be completely eliminated. Standard band-pass digital filters are another alternative to analyze data to separate microphonic noise; however, the process is

cumbersome and complicated to apply. Several digital filters were proposed such as an adaptive filter using system identification [20] or a low frequency rejector (LFR) filter for a hyper-pure germanium gamma ray detector [21]. The first technique uses a sensor to estimate the mechanical vibration and create an adaptive filter that effectively removes the impact from the measurement [20]. The LFR filter creates a modified trapezoidal weighing function that takes into account the changing baseline due to microphonic noise [21].

### **3 DETECTION SYSTEM DESIGN**

The detection system designed for determining the flux distribution in the core of the NSC reactor must cover a wide range of neutron fluxes, especially when pulsing the reactor. The design should also be compatible with many types of detectors potentially to be used at the NSC.

A detection system consists of three main hardware components and a data analysis software. The hardware includes the detector, electronic circuits, and a data acquisition unit. A slow neutron detector is needed in this work since slow neutrons induce nuclear fission in the reactor. The detector is connected to the electronic circuits which include preamplifier, analog shaping amplifier, and control and communication circuit. The outputs of the preamplifier and the shaping amplifier are then digitized by the data acquisition unit and stored on a disk drive. This allows the outputs to be post-processed by the data analysis software to derive information after an experiment is completed.

#### **3.1 Slow neutron detector**

In this work a prototype of a slow neutron detector was built with the primary purpose of investigating whether the design is fundamentally sound. The detector was designed to be placed in the core of the reactor to monitor neutron events during a reactor pulse. However, testing of the prototype detector was mainly performed outside the reactor core to determine its characteristics before in-core measurements.

A confined space inside of the reactor core puts limits on size of the detector. The

detector can be introduced into the core of the TRIGA reactor only through very narrow gaps between fuel rods or control rods. In addition, the detector must be small to avoid disturbing the flux distribution with the reactor, as well as not to interfere with the water flow system and/or other operations of the reactor. Therefore, the detector was designed to be encapsulated in an aluminum pole consisting of two separable sections, as shown in Figure 6. A bottom section is a detector holder which is approximately 0.9 m (36") long and has outer and inner diameters of 9.525 mm (0.375") and 7.747 mm (0.305"), respectively. The electrically insulated detector is to be positioned in the middle of the holder which is to be inserted into a small hole located between fuel rods and control rods inside the reactor core. The length of the detector holder is long enough to extend the top of the section, which connects to the other tube section, outside of the reactor core. The second section of the pole, the 9 m aluminum tube, has an outer diameter of 31.75 mm (1.25") and is where the electronic circuits reside. The circuit board is to be placed approximately 1 m from the bottom end of the this tube section. This makes the total distance between the detector and the electronic circuits slightly over 1.5 m. Aluminum was a preferred material for the pole due to its low cross section to thermal neutrons (0.231 barns) [10], its light weight, and its low impurities.

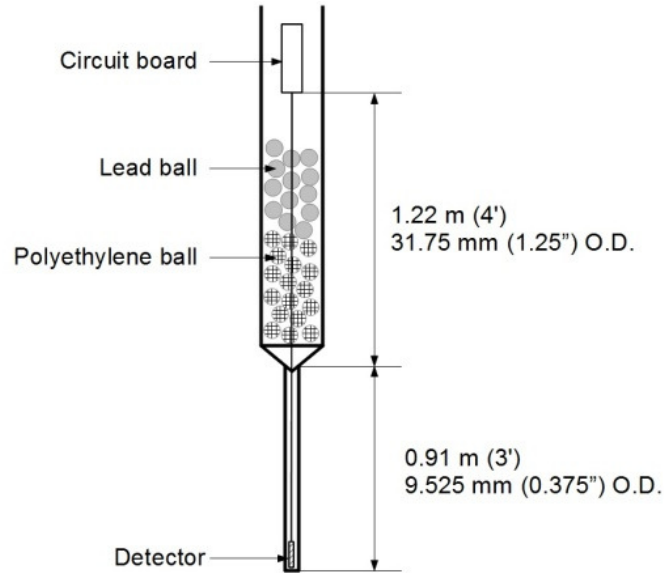


Figure 6 An aluminum pole consisting of a 0.9 m detector holder and a 9 m tube in which the electronics are located (drawing is not to scale). The polyethylene and lead balls are used for neutron and gamma shielding.

The experimental data reported in this thesis were collected from two detectors: detector A and detector B. Both of the detectors share the same geometry and materials except detector A does not have any target material to capture slow neutrons. A photograph of detector A is shown in Figure 7, and the detectors' parts and materials are listed in Table 2. The rationale for selecting the particular materials shown in Table 2 is given shortly.

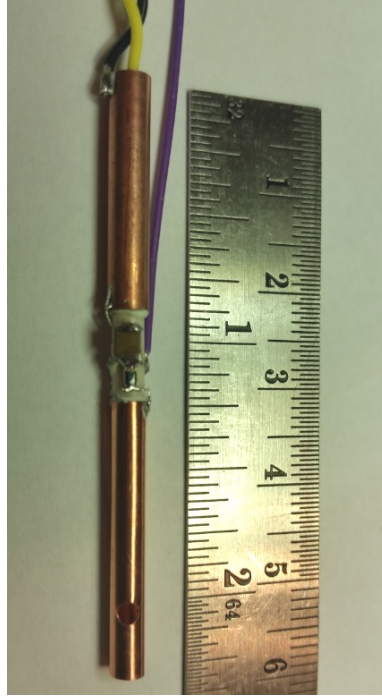


Figure 7 A photograph of detector A (in original color)

Table 2 Geometry and materials of the detectors used in the experiment in this thesis

| Detector | Anode Wire    |                            | High Voltage Tube      |                            | Target Material/<br>Area   |
|----------|---------------|----------------------------|------------------------|----------------------------|--|
|          | Diameter (mm) | Material                   | Inner Diameter<br>(mm) | Material                   |  |
| A        | 0.50          | Copper (99.997%<br>Purity) | 3.175                  | Copper (99.998%<br>Purity) | None   |
| B        | 0.50          | Copper (99.997%<br>Purity) | 3.175                  | Copper (99.998%<br>Purity) | 1- $\mu\text{m}$ thick boron-10/<br>$\varnothing$ 2-mm curved disc |

The neutron flux inside the core of the reactor, up to  $10^{13}$  neutrons/cm<sup>2</sup>/s, at 1 MW steady state power [4], leads to high reaction rate in the detector. Operating the detector in proportional region can cause complete ionization of the active volume, and the detector takes some time to return to its normal neutral condition. Once the whole detector volume is fully ionized, the detector cannot identify any further events.

Therefore, the high voltage applied to the detectors must be kept within the ionization region to avoid generating further electrons. In addition, the center anode of both the detectors has a large enough diameter to prevent intense electric field near the wires which can cause electron avalanche.

Air was used as fill gas at atmospheric pressure for both detectors. The use of air instead of common fill gas, such as methane or propane, offers the benefit of ease construction. The detector does not need to be tightly sealed to prevent a gas leak or withstand any pressure. This reduces unnecessary costs and construction complication. The detectors were built with a copper end cap to shield the anode conductor from electronic noise. Nonetheless, there are drawbacks to use air, one of which is due to electron and ion mobility. Because air has lower mobility compared with traditional fill gases using in neutron detection, the secondary electrons and ions generated from the neutron reaction take a longer time to drift to the corresponding electrodes. However, this longer collection time does not have a significant impact on the system as the electronics do not have a fast enough response to benefit from a higher mobility offered by a common fill gas. Another disadvantage of using air is electron attachment. Oxygen in air is notorious for high probability of electron attachment [8]. Secondary electrons generated from a neutron event could be lost by attaching to oxygen molecules. Similar to positive ions, negative oxygen molecules have much lower mobility than electrons; therefore, longer collection time is required. This drawback is then overcome by waiting long enough, say 20 to 40  $\mu\text{s}$ , to collect all charges, regardless of their source.

The detectors were made from pure copper (99.998% copper-63 and copper-65), because copper has a low cross section for thermal neutron (3.78 barns) [10]. Boron-10

was used as a slow-neutron capture material. Even though the Q-value of boron-neutron reaction is very low compared with other thermal neutron capture materials as shown in Table 1, boron was chosen for a target material in these first few prototypes developed. Using uranium, plutonium, or some other fissile material, which is radioactive, requires extra licensing and regulation. Also special care must be given to handling such material to ensure safety of the researchers, public, and the environment. These procedures can be complicated, time consuming, and unnecessary for initial studies of the system.

The solid form of boron as boron carbide ( $B_4C$ ) was used in the detectors. Although the gas form is also commonly found in slow neutron detectors, such as  $BF_3$  detectors, for the detector to function as a proportional counter, the advantage of proportional gas gain is not desired in this work to avoid saturating the detector in the high-flux environment of the reactor core. Additionally, solid boron does not required complex detector structure, and is easy to handle in the research lab. In initial trial experiments (not included in this thesis), a test was performed using a detector whose inner wall of the high voltage tube was entirely lined with boron to examine the detector's response to slow neutrons. However, this amount of boron was too much to test the detector in the reactor. A high neutron reaction rate can saturate the detector so quickly that not enough information about the reactor operation can be obtained especially during reactor pulsing. On the other hand, too little boron results in fewer detected neutrons. Therefore, the detector should have enough target material to give a reasonable neutron reaction rate before saturating the preamplifier. Detector B has a 2-mm hole on the high voltage tube which is covered with boron-lined copper piece. Consequently, the detector is not fully lined, and the area of detector B that is sensitive to slow neutrons is reduced to approximately 2 mm in diameter. Detector A was made with no target material in order to investigate

the operation of the design as an ionization chamber. The detector is to be tested with an alpha source before proceeding with detector B for neutron detection. Additionally, while detector B interacts to both neutrons and gamma rays, detector A responds to gamma rays only. Therefore, neutron information can be derived by placing both of the detectors at the same location and subtracting off the gamma-ray information, which is obtained from detector A, from the results from detector B. This method gives the results about neutron flux without gamma-ray contribution. The boron coating in detector B was chosen to be 1.4  $\mu\text{m}$  thick. The thickness of boron is an important factor in detector efficiency because it adds an additional layer through which alpha particles or lithium ions must travel through to the detector volume. They will lose some of their energy in the boron wall before reaching the inside of the detector. Lower energy leads to smaller pulses. The worst case scenario is when the reaction product loses all of its energy in the boron. When that happens, the neutron will not be detected even though it is captured by boron. In high rate imaging applications where  $\text{B}_4\text{C}$  was used, thermal neutron detection efficiency was predicted at approximately 3% for a planar  $\text{B}_4\text{C}$  with a thickness of 1  $\mu\text{m}$  [22]. The efficiency did not improve significantly with the boron thickness and reached a maximum of 4.7% at 3.2  $\mu\text{m}$  [22]. The ranges of an alpha particle and a lithium ion in  $\text{B}_4\text{C}$  are 3.36  $\mu\text{m}$  and 1.71  $\mu\text{m}$ , respectively [23].

Because the low reaction energy of  $\text{B}(n, \alpha)$  results in a small number of charges generated, a small signal is expected from the detector. Therefore, to maximize the signal-to-noise ratio, attention must be paid to the design of electronics or other sources of noise, such as cable type and/or length. Details on the electronic design, charge generated in the detector and other details of electronic implementation, especially the

preamplifier, are given in section 3.2.1.

### 3.1.1 Geometry of the detectors

Both detectors A and B share the same design as shown in Figure 8. The detectors have a right circular cylindrical shape with an anode wire in the center. Both the cylindrical tube connected to the high voltage and the anode wire were made from high-purity copper (99.99%) to avoid a neutron reaction from material impurities. Small Teflon tubing was used to center the anode wire in the middle of the larger ceramic tube, which provided insulation between the anode and the high voltage and the ground tubes. The details are summarized in Table 3.

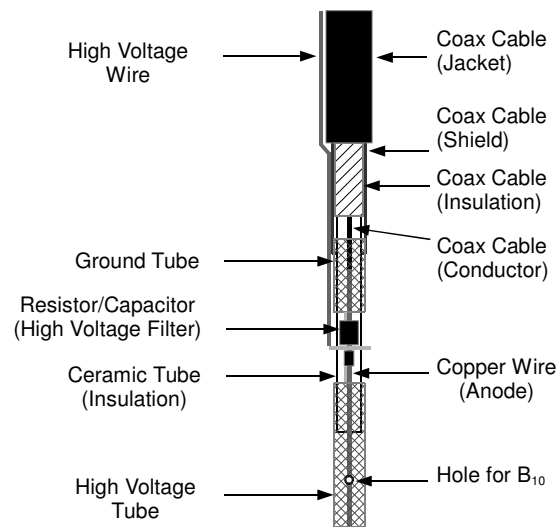


Figure 8 A sketch of the detector (Drawing is not to scale). The detector is made from a copper anode wire with a diameter of 0.50 mm and a copper high voltage tube with an inner diameter of 3.175 mm. A 2-mm hole was drilled out for boron at the center of the active volume.

Table 3 Specification of the parts of the detectors

| Parts                       | Details   |
|-----------------------------|---|
| Length of the active volume | 12.7 mm long  |
| Anode wire                  | Ø0.50 mm, high-purity copper (99.997%)  |
| High voltage tube           | 3.175 mm inner diameter, 0.10 mm wall thickness, high-purity copper (99.998%)   |
| Target material             | 1-µm thick boron coated on copper, Ø2mm curved disc on the high voltage tube  |
| Ceramic insulation          | 1.6 mm (0.063") inner diameter, 3.175 mm (0.125") outer diameter  |
| High voltage filter         | 100 kΩ resistor and 0.01 µF capacitor   |
| Cable                       | Anode wire: coaxial cable RG-62A, Ø6.15 mm, 22 AWG, 1.68 m (5.5 ft) from the detector to the preamplifier, capacitance 13.2 pF/ft,<br>High voltage cable: 28 AWG, 600 V |

The longest track in air of an alpha particle which is a product of  $B(n, \alpha)$  reaction and has an initial energy of 1.47 MeV is approximately 7.35 mm [24]. Because the energy of an alpha particle ranges from 0 to 1.47 MeV, the path length varies starting from 0 to 7.35 mm. However, in a detector not all of the alpha particles will lose all of their energy. Small size and cylindrical shape of the detector put limitations on the path length. In some directions, an alpha particle cannot travel to its full range in air and will crash into the wall or the anode wire before losing all of its energy in the detector. Figure 9 shows the simplified two dimensional cross section of the detector crosswise and lengthwise, respectively. In some angles the particle can travel further than others which results in more energy absorbed in the detector considering equal initial energy when the particle enters the detector active volume. As a result, the spectrum of the detector will not have a rectangular shape as ideally shown in Figure 3. A simulation of the detector using MCNP software was performed by Jan Vermaak [25]. Because only one of the reaction products enters the detector per one captured neutron, the final spectrum of the detector is a combination of the spectrum due to the alpha particle or the lithium ions separately. Figure 10 shows the spectrum due to each product and the final spectrum from the simulation [25].

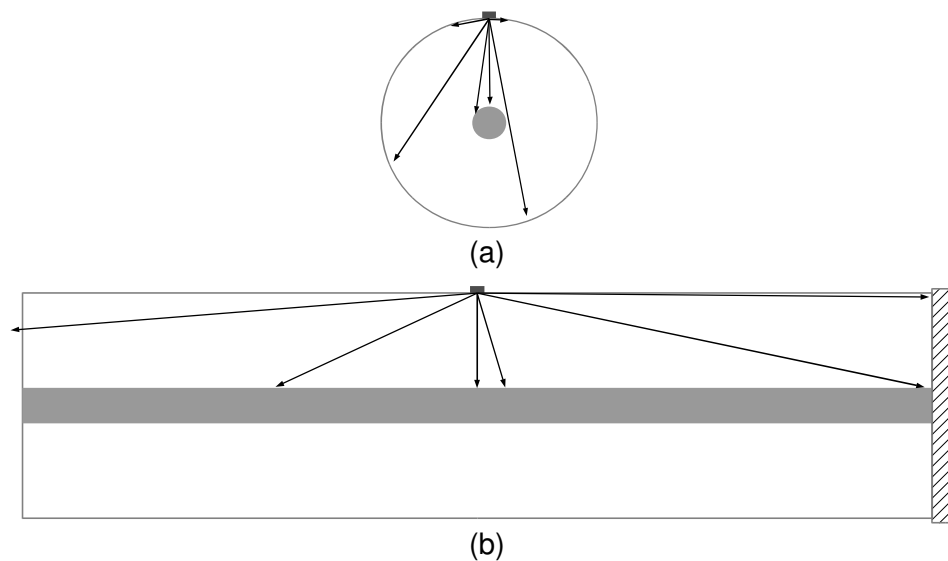


Figure 9 Possible paths of the reaction products (simplified to 2D) (a) crosswise cross section (b) lengthwise cross section

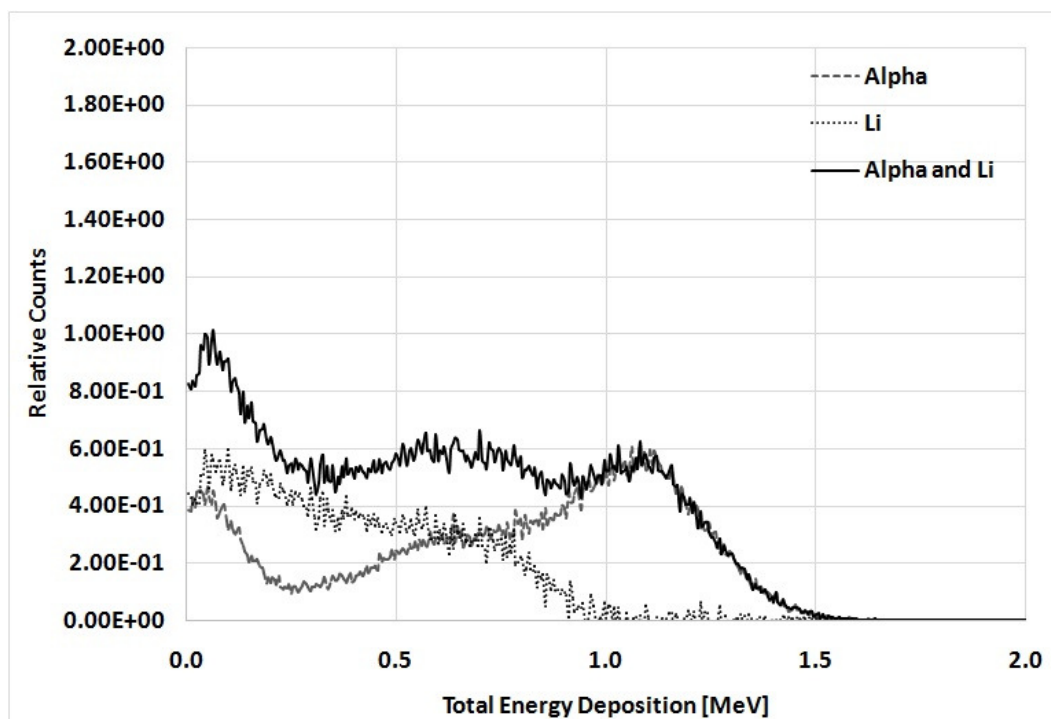


Figure 10 Spectrum of the detector by MCNP simulations [25]

The number of charges created in the detector during one radiation interaction depends on the number of ion pairs formed along the track of the reaction product which is in turn directly proportional to the energy it loses in the detector. In the best case scenario the reaction product will lose all of its energy inside the detector, and the highest possible energy loss is 1.47 MeV by an alpha particle. The average energy per ion pair created is typically around 25 to 35 eV/ion pair [8]. Therefore, the possible maximum number of ion pairs formed in the detector is between 42000 and 58800 pairs resulting in the total charge of  $6.72 \times 10^{-15}$  C to  $9.408 \times 10^{-15}$  C from the electrons and negative ions (the number of charges carried by one electron or one positive ion is  $1.6 \times 10^{-19}$  C). With a typical preamplifier gain of  $10^{12}$  V/C, this gives a maximum voltage peak of 6.72 mV to 9.408 mV.

### **3.2 Electronic circuits**

The electronic circuits are responsible for processing charges that are collected from the detector. Since a small number of secondary charges are generated from a boron-lined ionization chamber due to low reaction energy, a high gain charge sensitive preamplifier is required to amplify the signal. This high gain also results in amplification of noise. Consequently it is very important to keep the noise level at a minimum including shortening the cable length between the detector and the preamplifier circuit.

For simplicity, the electronics should be located near the control room and at a distance from the reactor to avoid radiation damage, especially inside or near the reactor core. Silicon is one of the common elements in integrated circuits (ICs) that is easily damaged and can have a short life in a high radiation environment. The damage includes both single-event effects, such as alteration of the memory, and long-term effects, such as

crystal structure disruption [26]. However, parasitic capacitance in the cable from the detector to the electronics is one of the common sources of noise in the system [8]. A long cable usually introduces a several fold increase in noise to the signal. Therefore, the preamplifier, especially the charge sensitive preamplifier for low level signal produced by boron, must be located close to the detector. To compromise between the damage from the radiation and the increased noise from the cable, the design decision was made to place the electronic circuits at approximately 1.68 m (5.5 ft) from the detector. The electronics were laid out on two printed circuit boards (PCBs): a 16.9 mm x 298.5 mm (0.664"x11.75") board and a 16.3 mm x 198.8 mm (0.640"x7.825") board as shown in Figure 11. They were assembled back to back and then shielded in a 300 mm long grounded copper tube. The tube will be placed 1.2 m (four feet) up from the bottom end of the second section of the pole as shown in Figure 6. Below the circuit boards, the pole was filled with layers of polyethylene balls and lead balls both of which were 6.35 mm (0.25") in diameter. Polyethylene and lead are effective at absorbing neutrons and gamma rays, respectively; therefore, they provide some radiation shielding to the circuits.

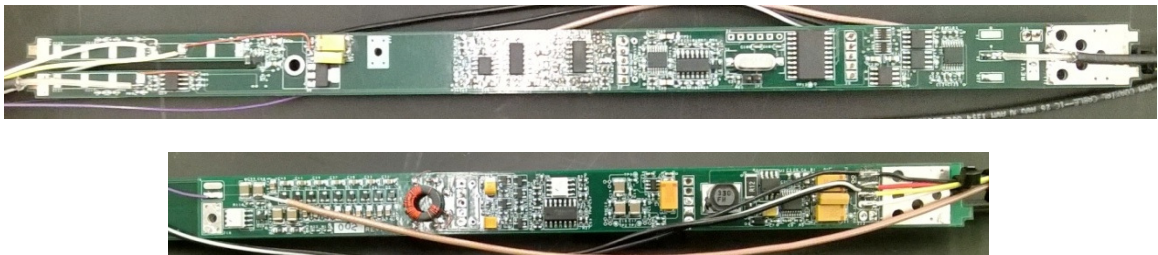


Figure 11 Electronic circuit boards being assembled back to back (in original color)

Figure 12 shows the block diagram of the electronic system. The circuits used in the experiment reported in this thesis consisted of a preamplifier, an analog shaping amplifier, a test pulse generator, a microcontroller, a communication circuit and a power supply. Each component is discussed later in this chapter. Two connections were made between the detector and the electronics: the output of the detector and the filtered high voltage. There were seven wired connections between the circuit and the user's end. The outputs from the preamplifier and the shaping amplifier were connected to the data acquisition unit for digitization. Other connections were power lines, high voltage line, and communication signals. The connections are listed in Table 4.

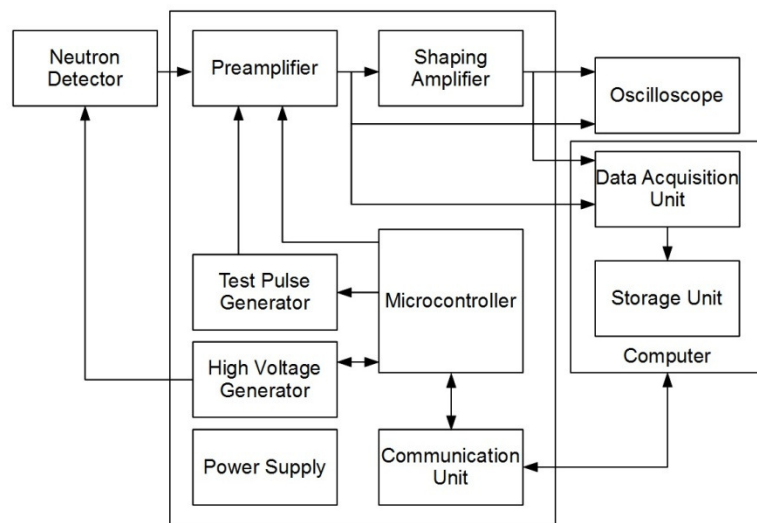


Figure 12 Block diagram of the electronic system. The circuit includes a preamplifier, an analog shaping amplifier, a pulse generator, a power supply, and a control and communication circuit

Table 4 Connections from the circuit to the detector and to the user's end. The first had two signals while the latter had five connections.

| Signal                | Connection  | Cable details  | Length (m (ft)) |
|-----------------------|---|--|-----------------|
| Detector output       | From the detector to the circuit,<br>ground shielded cable                              | Coaxial cable RG-62A<br>Wire gauge 22 AWG solid<br>Polyethylene dielectric insulation<br>Ø 6.15 mm<br>Characteristic impedance 93 Ohm<br>Ground capacitance 13.2 pF/ft | 1.68 (5.5)      |
| Filtered high voltage | From the circuit to the detector  | 28 AWG, 600 V  | 1.68 (5.5)      |
| High voltage line     | From the high voltage generator to<br>the circuit                                       |  | 27.43 (90)      |
| Preamplifier          | Output of the preamplifier to the data<br>acquisition unit and the oscilloscope         | Coaxial cable RG-174/U<br>Wire gauge 26 AWG<br>Characteristic impedance 50 ohm   | 27.43 (90)      |
| Shaping amplifier     | Output of the shaping amplifier to the<br>data acquisition unit and the<br>oscilloscope | Coaxial cable RG-174/U<br>Wire gauge 26 AWG<br>Characteristic impedance 50 ohm   | 27.43 (90)      |
| Power line            | 9 V DC power and ground from an<br>AC/DC adaptor to the circuit                         |  | 27.43 (90)      |
| Tx and Rx             | RS232 Rx and Tx between the circuit<br>and the user's computer                          |  | 27.43 (90)      |

The cable between the detector and the preamplifier has two important characteristics: size and capacitance. When comparing between two coaxial cables, a thinner cable typically has higher capacitance which leads to more noise in the system. Although a low-capacitance cable is preferred to lessen the noise, size of the cable is limited by the detector holder. The diameter of the cable must be less than 7.747 mm or 0.305" to fit inside of the holder. In the current system, the cable is 6.15 mm (0.242") in diameter and has a capacitance of only 13 pF/ft. Thus, 1.68 m or 5.5 foot of cable adds approximately

70 pF of capacitance. In the initial design of the previous prototype circuit, the preamplifier alone had about 400 electrons rms, and 4 electrons rms was added per pF of capacitance. As a result, the noise was increased by 280 electrons rms; in other words, a 1.68 m cable introduced 70% increase in noise from the original 400 electrons rms noise (without the cable connected) to 680 electron rms noise.

### **3.2.1 Preamplifier**

The preamplifier is the most critical part of the circuit. The signal from the detector is quite small because of the low Q-value of the neutron-boron interaction; therefore, a high-gain charge sensitive preamplifier is required. The preamplifier has a pulse mode operation in which each neutron event can be observed; therefore, it provides an opportunity to obtain as much information as possible about the neutron and gamma interactions. The electric field of the high voltage applied to the detector forces the secondary charges created from the neutron-induced interaction to drift toward the corresponding electrodes where these charges are collected. During charge collection time these charges are integrated on the input capacitor which results in an increase of the preamplifier output voltage. In the current design, the input capacitor is approximately 1 to 2 pF providing a conversion gain of  $5 \times 10^{11}$  to  $1 \times 10^{12}$  V/C (1 F is equal to 1 C/V). An example of the preamplifier output is shown on channel 1 or the top line in Figure 13. It was the test performed at the University of Ontario Institute of Technology (UOIT), Oshawa, Ontario, Canada, in November 2014. Neutron events were created by a P385 neutron generator, and a 50 mm thick polyethylene block was used to moderate the generated neutrons. The detector used in this test had the full boron-lined wall (not just an area of 2 mm as for detector B). The preamplifier output shows an approximately 5 mV rise in the voltage in an order of a few tens of microseconds suggesting a neutron

event. Channel 2 or the bottom line in Figure 13 shows the output of the analog shaping amplifier.

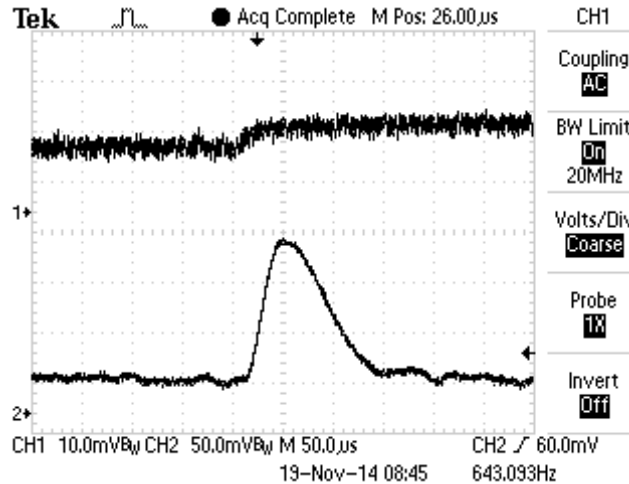


Figure 13 Example of the response of a neutron event. Channel 1 (the top line) and channel 2 (the bottom line) show the outputs from the preamplifier and the shaping amplifier, respectively.

To reset the output of the preamplifier, the capacitor must be discharged which can be accomplished in a number of ways. One method is pulsed optical feedback where the input field-effect transistor (FET) of the operational amplifier (op-amp), which is connected to the capacitor, is briefly illuminated to discharge the capacitor [27]. Alternatively the input of the op-amp and the capacitor may be temporarily connected to ground through a transistor [28]. This method is called transistor reset. Another common approach called feedback resistor reset discharges the capacitor through a resistor [29]. A simplified schematic of such a circuit is shown in Figure 14. The charges in the capacitor bleed off through the feedback resistor  $R_f$  which is typically permanently connected. Generally a large resistor is preferred as the resistor value is inversely

proportional to the noise level [8]. In other words, a smaller resistor causes more noise in the system than a larger one. However, a large feedback resistor may be replaced by a small one in series with a switch [29]. The resistor is then only connected to the circuit momentarily during the reset period. In reference [29], a relay was used as a switch, and the feedback resistor was 10 M $\Omega$  which limits the current and prevents the relay from oscillation.

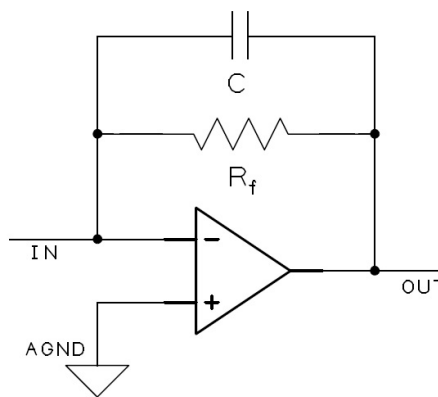


Figure 14 Simplified schematic of the charge-sensitive preamplifier with a feedback resistor reset [29]

In this work, a feedback resistor reset was implemented. However, instead of connecting the feedback resistor permanently to the preamplifier circuit, the connection was made through a reed relay, similar to that of reference [29], but a large resistor, 100 M $\Omega$ , was used to preserve the low noise level. The relay switch was controlled by an on-board microcontroller; as a result, the reset mechanism of the preamplifier had two modes of operation: unlatched and latched. The latched mode was identical to a charge-sensitive amplifier with a large feedback resistor permanently connected for reset. The output of the preamplifier is connected to the data acquisition unit as well as a shaping circuit.

### 3.2.1.1 Modes of operation

The preamplifier circuit currently operates in pulse mode with a large feedback resistor and offers two modes of reset mechanism: unlatched and latched.

#### Mode 1: pulse mode – unlatched reset

In this mode of operation, the feedback resistor is normally disconnected from the preamplifier output. Without a resistor to discharge, charges generated from neutron events will accumulate. Ideally, the capacitor will not have any leakage and will keep all of the collected charges; therefore, after all the charges from a neutron event are collected, the number of charges in the capacitor will remain constant. Consequently, the output voltage of the preamplifier will rise only when there is a neutron event and will keep a constant level in between the events. Figure 15 shows an example of the preamplifier output. Channel 1 (the top line) and channel 2 (the bottom line) are the responses of the preamplifier and the analog shaping amplifier, respectively, to two neutron events (two smaller events in the middle of the screenshot) and three test pulses (three events with the same height and evenly spaced on the left, right, and in the middle). From the experiment, the estimated rise time of a neutron event was 20 to 35  $\mu\text{s}$ , and the observable pulse height was approximately 5 mV. The maximum number of charges collected along the track of the reaction product in the detector is  $9.408 \times 10^{-15}$  C, as per section 3.1. The one-pF input capacitor in the preamplifier circuit provided a gain of  $1 \times 10^{12}$  V/C. As a result, the maximum voltage for each neutron event was 9.408 mV.

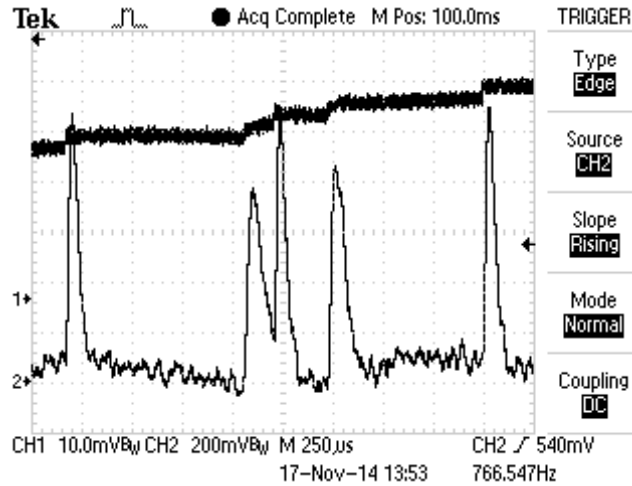


Figure 15 Outputs of the preamplifier when operating in pulse mode with unlatched reset. Channels 1 (the top line) and 2 (the bottom line) shows the preamplifier output and the shaping amplifier output, respectively.

If there is no leakage, the output level of the preamplifier will increase with every neutron event, and all the collected charges will remain in the capacitor until the microcontroller issues a reset signal to connect the feedback resistor to the circuit. The capacitor will then discharge, and the preamplifier will restore its baseline potential output. For the best results, the reset must occur before the preamplifier saturates. Once the saturation level is reached, no further information can be derived from the output signal which is simply a flat line.

One of the benefits the pulse mode with unlatched reset offers is that the information about both neutron and gamma events can be obtained from the output signal. When the detector is exposed to gamma rays, the secondary electrons are generated in the detector volume and will also drift to the collecting electrodes under the influence of the high voltage electric field. As a result, the charges stored in the input capacitor are

generated not only from neutron interactions but also from gamma events. However, because a gamma ray photon usually loses only a small fraction of its energy in the detector volume, very few charges are generated from a gamma event compared with the number created by a neutron event. These charges will be quickly discharged before producing a detectable signal if the feedback resistor is connected. Without the resistor, the small but frequent gamma contribution will result in a slowly increasing slope between sharp rises from neutron events. Steepness of the slope suggests the intensity of gamma radiation. The more gamma rays the detector is exposed to, the steeper the slope is. Therefore, in this mode of operation both neutron and gamma information can be derived from the preamplifier output. However, the unlatched reset preamplifier does not work well in a high gamma ray environment. Intense gamma rays will cause a very steep slope on the output and the preamplifier will quickly saturate. The system is then no longer useful until the circuit is reset.

One of the basic pieces of information derived from this mode is the average charges created by a neutron, referred to as  $Q_{avg}$ . The number of charges depends on the product of the input capacitance and the average size of neutron pulses. This relationship can be written as:

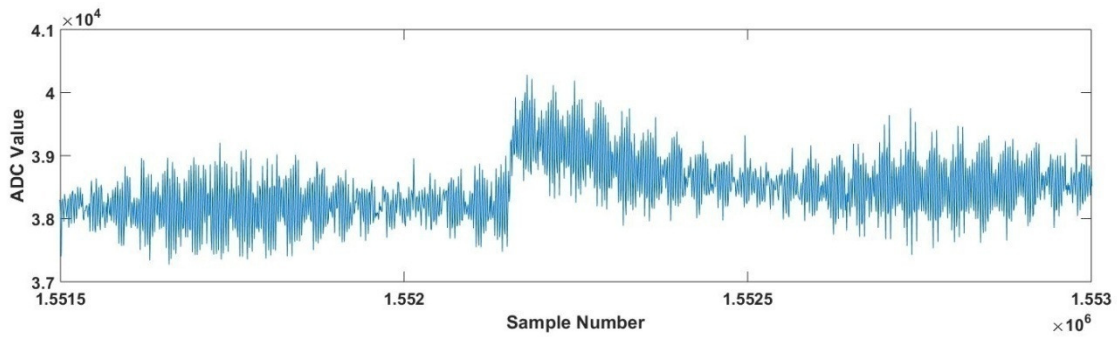
$$Q_{avg} = CV_{avg} \quad (3.1)$$

where  $Q_{avg}$  is the average charges created along the track of the reaction product,  $C$  is the input capacitor, and  $V_{avg}$  is the average size of the neutron pulses. For example, if the neutron pulse is 1 mV on average, the number of charges is equal to  $1 \times 10^{-15}$  C per neutron event (assuming the input capacitance is 1 pF). This information can be used in the analysis in other modes of operation.

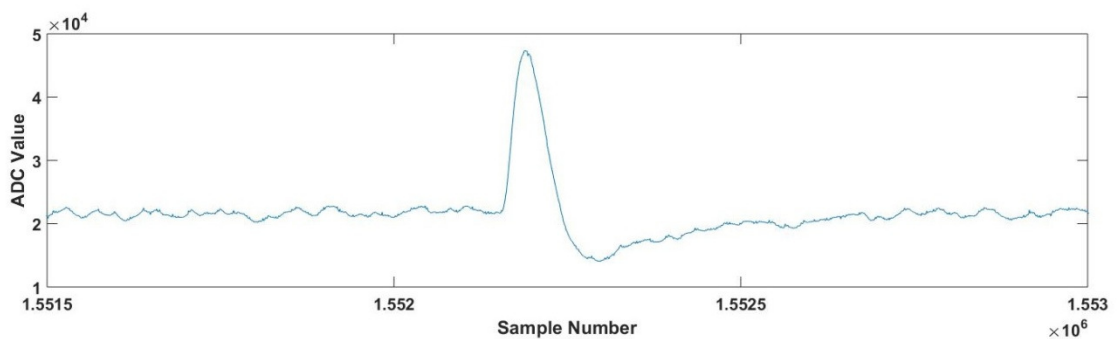
## Mode 2: pulse mode – latched reset

The reset signal is issued by the microcontroller and controls the connection between the feedback resistor and the circuit. The connection is mechanical rather than electrical to reduce the leakage to the minimum; however, it requires longer time to make a good connection and also longer recovery period. The mechanical part normally vibrates when the connection is switched on and off. Since the preamplifier is sensitive to vibration, the output signal can be unstable for a short period of time (in an order of microseconds) after the reset occurs. Therefore, the system operating in the unlatched reset mode only works well up to a certain radiation intensity. Frequent resets which are required in high neutron and gamma environments to prevent saturation of the preamplifier leads to a longer reset and recovery time than operating period. In this situation, it is better to permanently connect the feedback resistor to circuit or, in other words, to latch the reset to avoid the frequent dead time from mechanical movement of the reset mechanism.

Because the feedback resistor is permanently connected to the circuit, the capacitor will continuously discharge. Thus, if the reaction rate is not too high, the preamplifier output will return to its baseline potential shortly after each radiation event. An example of the preamplifier output is shown in Figure 16. The discharge time constant is equal to the product of the feedback resistance and the input capacitance. This restoration allows the preamplifier to operate in pulse mode longer in the high radiation environment before the saturation level is reached.



(a)



(b)

Figure 16 Outputs of the preamplifier and the shaping amplifier in response to a neutron event (a) the preamplifier output (b) the shaping amplifier output

Even though the latched reset has an advantage in high radiation environment, the information about small events including gamma interaction could be missed. This happens when the number of charges generated in the radiation event is too small such as a gamma event or when only a small proportion of the energy of the boron-neutron interaction energy is deposited in the detector. The feedback resistor will remove the charges from the capacitor before an observable output signal is generated. Also, more noise is expected in the output signal compared with the unlatched reset mode due to the additional resistor is connected to the preamplifier. The lower resistance in the circuit

will result in more noise in the signal.

The preamplifier circuit used in this work switches between these two modes of operation by a user command sent to the on-board microcontroller. The microcontroller then unlatches or latches the reset. Mode 1, a pulse mode with unlatched reset, is a default power on mode of operation. Because the event rates in the reactor can vary largely, one mode of operation may be better than the other or some experiments may require the test to be repeated in both of the modes to gather the information needed.

### Mode 3: current mode

Although pulse mode gives more detailed information about the radiation event, pulse pile-up and saturation can become problematic at very high radiation intensity. In this case, current mode is more suitable for the preamplifier. In current mode, the feedback resistor is permanently connected similar to the pulse mode with latched reset (mode 2); however, the value of the resistor is different. The current mode has much lower feedback resistance which allows current to flow through. The size of the feedback resistor has an impact on the preamplifier in two aspects: the noise of the preamplifier output and the gain of the current-to-voltage conversion. The signal becomes noisier when the lower resistor is used, but it is necessary in the current mode. For the same amount of current flowing through two different resistors, the circuit with the smaller resistor value will produce a lower output voltage. The output voltage is equal to the current multiplied by the feedback resistor.

Because the current is monitored instead of the direct charge, a current-mode system is less sensitive to individual events. Current mode provides information about the event

rate which can be derived from the measured output voltage. First the voltage is converted back to the current by dividing the output by the feedback resistance or  $I = V/R_f$ . Because the current is the number of charges per second, one can estimate the neutron event rate. Refer to the pulse mode, the average number of charges per neutron event  $Q_{avg}$  is previously derived in Equation (3.1). The number of the detected neutrons per second, referred to as the event rate  $Rt$ , is then equal to the current divided by the average charges per neutron or

$$Rt = I/Q_{avg}. \quad (3.2)$$

Although in the high radiation the preamplifier is better operating in the current mode, it is not suitable in the environment where the gamma flux is strongly present. This is because the current is the result from all the charges collected at the electrodes no matter how the charges are created. One cannot tell the difference between the charges created by the neutron and the gamma interactions. Therefore, it is important that the number of charges from the neutron event be sufficiently higher than from the gamma event so that the gamma charges are negligible. A gamma compensated detector is also recommended.

In this work, a feedback resistor of 100 M $\Omega$  is used; however, it can be replaced by different values to give a larger dynamic range. Automatic switching between these modes of operation is also possible.

Mode 4: high voltage current mode

The system can operate in another mode of operation in which the radiation is not

directly measured at the preamplifier output. In the situation where the count rate is very high, the radiation can be alternatively measured by monitoring the current through the high voltage line. The high voltage is normally filtered by an RC circuit to eliminate voltage variation and keep the line stable. This provides an opportunity to measure the current by observing the voltage across the resistor of the filtering circuit. Normally the large resistor is used for the high time constant; however, it causes a slow response of the circuit to the radiation event. For example, the filtering circuit with 10 M $\Omega$  resistor and 0.01  $\mu$ F capacitor has the time constant of 100 ms, so the response of the circuit is in the Hz range. Then the lower resistor value is preferred. The current filter used 100 k $\Omega$  resistor giving a 1 ms time response.

Since this mode operates in a similar manner to the current mode (mode 3), the neutron information can be derived using the same method. The difference is the voltage across the feedback resistor is substituted with the voltage across the high voltage resistor. The high voltage current mode was not tested in the current system.

### *3.2.1.2 Expected dynamic range of neutron fluxes*

Between these modes of operation, the system can operate over a wide range of neutron fluxes. A rough calculation was made to determine whether the system capability was within an acceptable range.

#### *High voltage current mode*

The maximum neutron flux in this mode is limited by the voltage across the resistor that is measured by the analog-to-digital (ADC) circuit. For an input from 0 to 5 V the

maximum current through the high voltage resistor (100 k $\Omega$ ) is 50  $\mu$ A. From Equation (3.1) and the example in section 3.2.1.1, the average charges per neutron event or  $Q_{avg}$  is  $1 \times 10^{-15}$  C. According to Equation (3.2), the event rate  $Rt$  or the number of detected neutrons per second is equal to  $5 \times 10^{10}$  neutrons/s. Given that the rate of detection is less than 1 in 1000 and that the boron area is approximately 3 mm<sup>2</sup> which is 3/100 of cm<sup>2</sup>, the maximum neutron flux is in the range of  $5 \times 10^{10} \times 1000 \times 33 = 1.65 \times 10^{15}$  neutrons/cm<sup>2</sup>/s which is approximately the maximum core flux during a large power pulse. Steady-state reactor power is  $10^{13}$  neutrons/cm<sup>2</sup>/s.

The minimum neutron flux depends on the resolution of the ADC circuit. A 13-bit resolution provides approximately 8000 levels or 0.625 mV per channel. If an accuracy of 10% is desired, the voltage across the high voltage resistor must be 6.25 mV or higher or the current must be at least 62.5 nA. Applying Equation (3.1) and (3.2),  $Rt$  is  $62.5 \times 10^6$  neutrons/s. The minimum core flux is then approximately  $62.5 \times 10^6 \times 1000 \times 33 = 2 \times 10^{12}$  neutrons/cm<sup>2</sup>/s approximately.

#### *Current mode – latched reset*

The current mode supports the range of neutron fluxes in between the pulse mode and the high voltage current mode. Similar to the high voltage mode, the maximum neutron flux is determined by the maximum voltage of 5 V across the feedback resistor of 100 M $\Omega$ . The maximum current is then equal to 50 nA which is 1/1000 the maximum current of the high voltage mode. Therefore, the minimum and maximum neutron fluxes are  $10^9$  and  $10^{12}$  neutrons/cm<sup>2</sup>/s, respectively. The corresponding detected neutron rates  $Rt$  are  $10^4$  to  $10^7$  neutrons/s, respectively. If a different resistor is used such as 1 G $\Omega$ , the

minimum and maximum neutron fluxes becomes  $10^8$  and  $10^{11}$  neutrons/cm<sup>2</sup>/s, respectively.

#### *Current mode – unlatched reset*

When the reset is unlatched, each boron-neutron event adds the charges to the capacitor until the preamplifier is saturated at 5 V. Given the average increased voltage per neutron event is 1 mV (from the previous example in section 3.2.1.1), the preamplifier will saturate if 5000 neutrons are detected. If the preamplifier is reset every second, this is equivalent to the maximum neutron flux on the order of  $10^8$  neutrons/cm<sup>2</sup>/s (5000 neutrons/s, 1 in 1000 neutrons are detected, and the area of the detector is 3/100 cm<sup>2</sup>). However, the reset circuit is capable of resetting the preamplifier at every 100 ms. Therefore, the maximum neutron flux can be as high as  $10^9$  neutrons/cm<sup>2</sup>/s.

Similar to the high voltage current mode, the minimum neutron flux depends on the ADC resolution. For 10% accuracy, the increased voltage of at least 6.25 mV is required which is 1/800 of the full scale of 5 V. Consequently, the minimum neutron flux is 1/800 of the maximum flux. For the 100 ms reset interval, the minimum flux is then on the order of  $10^6$  neutrons/cm<sup>2</sup>/s.

#### *Pulse mode*

In pulse mode of operation the neutron flux range is bounded by the time required to recognize one pulse. The separation between pulses must be sufficient not to create too much pulse overlap; however, with some dead-time corrections some pulse pile-ups can be resolved. The shaping circuit normally takes 50  $\mu$ s to process a neutron pulse. The

average separation between pulses should be at least double or 100  $\mu\text{s}$ . For 100  $\mu\text{s}$  separation between pulses, the number of detected neutrons per second is limited to  $1 \times 10^4$  neutrons. Thus, the preamplifier can operate in pulse mode from 0 to  $10^8$  neutrons/cm<sup>2</sup>/s.

From these calculations, the preamplifier is expected to support neutron fluxes in the range from 0 to  $10^{15}$  neutrons/cm<sup>2</sup>/s by switching from one mode to another. Pulse mode is preferred in low fluxes and high voltage current is needed in high flux situation. The current mode is used in the intermediate range.

It is important to note that when the event rate  $Rt$  is low, one has to wait for a period of time to accumulate enough pulses to achieve the desired accuracy. For example, a minimum of 100 pulses are needed for 10% accuracy. If  $Rt$  is equal to 10 neutrons/s, one has to acquire the data for 10 seconds in order to detect 100 pulses. In reactor transient analysis, the rate at 10 ms interval are of interest. The count rate or the number of the detected neutron must then be  $1 \times 10^4$  neutrons/s at the minimum to get 10% accuracy. However, the rate of the detected neutrons is limited to  $1 \times 10^4$  in pulse mode of operation. Therefore, the pulse mode will not be able to achieve 10% accuracy in the analysis of 10-ms intervals.

### **3.2.2 Shaping amplifier**

The shaping amplifier performs analog pulse processing as a differentiator by a capacitor-resistor (CR) circuit followed by an integrator which is a resistor-capacitor (RC) circuit. Figure 13 shows the output of the CR-RC shaping circuit (channel 2 or the bottom line of the screenshot). The circuit used had a shaping time constant of 10  $\mu\text{s}$ .

The shaped pulses correspond to the neutron events or the test pulses simulating neutron events. Under normal circumstance the CR-RC shaping circuit generates pulses due to gamma events only when gamma rays lose enough energy in the detector and raise the preamplifier output level high enough to produce low-amplitude pulses.

Since the shaping circuit amplifies the preamplifier signal to a much larger pulse (approximately 80 times), it can provide preliminary information about neutron events that cannot be observed instantly from the preamplifier output. This allows the shaped pulses to be easily observed once low-amplitude signals from electronic noise are discriminated against. The shaping amplifier is also connected to the data acquisition unit so that the output can be used as reference and for comparison between the conventional analog circuit and digital post-analysis of the preamplifier output.

### **3.2.3 Test pulse generator**

A test pulse generator was used to simulate charge collection of neutron events by the detector. The ability to create test pulses greatly helped in debugging and verifying the operation of the electronic system.

### **3.2.4 Microcontroller**

A microcontroller was used to control several components on the circuit board. This includes the operation of the preamplifier, such as the reset mechanism, test pulse generation, and possibly high voltage management. The microcontroller communicates with the user to receive user's commands such as to latch or to unlatch the reset, to turn on or off the test pulse generator, or to set the size of the test pulses.

### **3.2.5 Communication circuit**

A communication channel is provided between the user and the microcontroller through a standard 3-wire RS-232 serial interface. The cable and transmission speed can maintain reliable communication over 27-meter (90-foot) distance which is required between the location of the circuit and the user's computer. The system offered one-character commands including turning on the test pulse generator, increasing or decreasing the size of the test pulses, and latching or unlatching the reset mechanism of the preamplifier.

### **3.2.6 Power supply**

Dual supply voltages were generated on the circuit board to supply both analog and digital circuits. A 9-V DC input was required.

### **3.2.7 High voltage generator**

An external high voltage generator, Tennelec TC950, was used in this work. The generator offered one output in either negative or positive polarity up to 5 kV. This voltage was sufficient to accelerate the charged particles before they are neutralized by recombination.

## **3.3 Data acquisition unit**

The data acquisition unit is responsible for digitizing and storing the output from the electronic circuit. It was connected to the preamplifier and the shaping amplifier. The digitized outputs were stored on the acquisition unit to be post-processed by the data analysis software after an experiment was completed. The data acquisition unit was partitioned into a data acquiring component and a storage component.

### 3.3.1 Data acquisition

The data acquiring component is responsible for digitizing analog input signals at high speed. Since in this application air was used as the fill gas in the detector, the low mobility of air results in slow rise time of the preamplifier output. According to Figure 13, the rise time was approximately 25  $\mu$ s. According to the Shannon sampling theorem, the sampling frequency is required to be at least twice the signal frequency (This minimum frequency is commonly called Nyquist rate) [30]. Therefore, the minimum sampling frequency for this particular system was 80 kHz. However, the data acquisition unit was designed to be flexible to interface with other systems that could have much faster rise time. Therefore, the acquisition system was designed to sample at a frequency up to 250 MHz. At this rate, the system is theoretically capable of working with an application that has a rise time in the nanosecond range.

The transfer rate from the digitizer to the storage disk was selected to be high enough to keep up with the sampling frequency. If each digital sample is two bytes long, the transfer speed of 500 MB/s is required for the sampling frequency of 250 MHz.

An off-the-shelf product that meets the requirement has recently become available from DynamicSignals LLC. The brand and model of the product used in the current system was Signatec PX14400D2. A photograph of the card is shown in Figure 17, and the important features are summarized below [31]:

- 2 DC-coupled analog input channels
- 6 full scale peak-to-peak voltage ranges from 200 mV to 3 V
- 14-bit analog-to-digital resolution

- 20 MHz – 400 MHz sampling rate per channel
- 512 MB RAM for raw data capture
- 8-lane PCI express (PCIe) bus interface for data transfer (up to 1400 MB/s)

The card has two acquisition modes: continuous and buffered modes. In continuous mode RAM is used as FIFO memory when digital samples are streamed directly to PCIe. This mode requires the sample data to be further transferred from the PCIe interface to the storage component before the FIFO is full; otherwise, the data acquisition will stop and an error will be notified. In buffered mode, which has a selectable buffer size, the samples are first stored in RAM before transferred to the computer. Thus, the speed of the storage unit is not an issue when operating in this mode. However, during the data transfer no additional samples can be taken which means some parts of the signals will be lost. The data reported in this work was taken in the buffered mode.

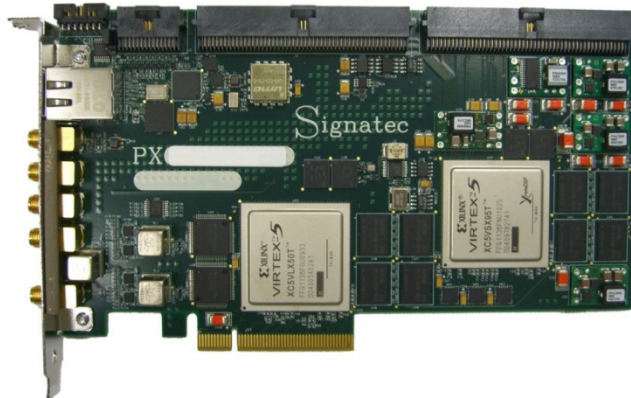
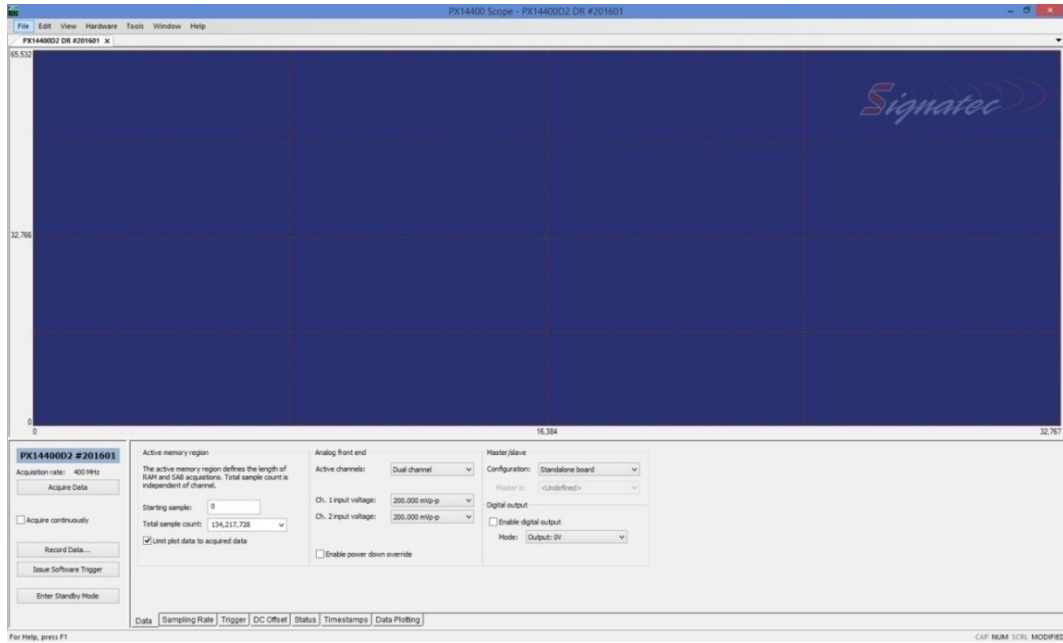


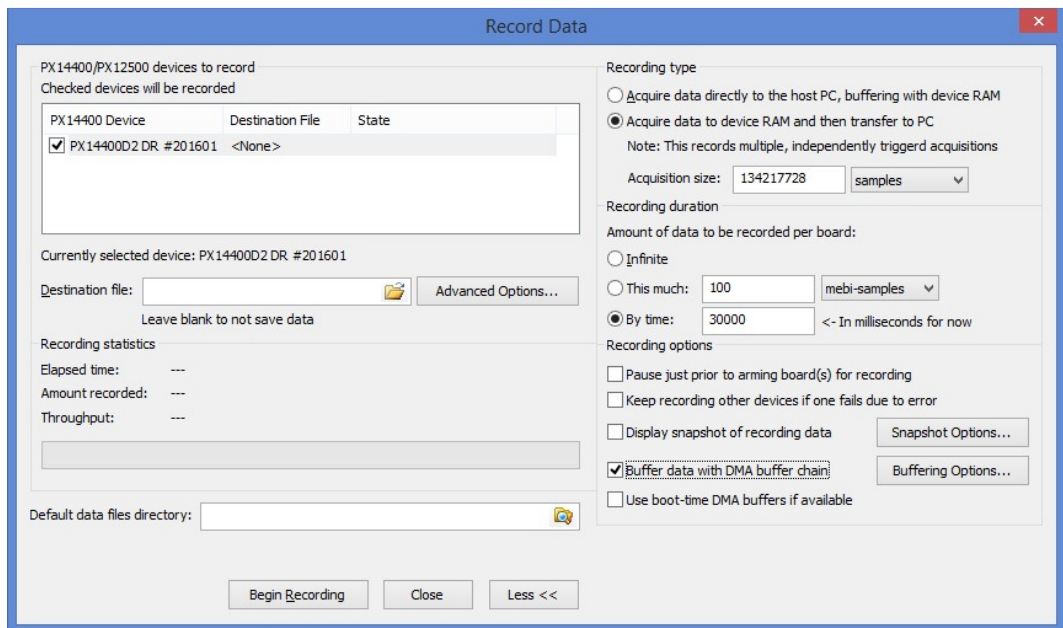
Figure 17 A photograph of the Signatec PX14400D2 board [31] (in original color)

A scope application software was provided with the digitizer board. Through its graphical user interface (GUI), the sampling frequency and the input voltage range can be set. In

addition, several recording options are available such as acquisition mode settings or selection of the buffer size. Some screenshots of the GUI are shown in Figure 18. This application has sufficient features to accomplish the preliminary tests of the detector and the electronics. Therefore, it was used in the experiments reported in this thesis.



(a)



(b)

Figure 18 Signatec scope application software screenshots (a) Main screen (b) Record data window

### **3.3.2 Data storage**

The analog inputs were sampled by a PX14400D2 acquisition card. The output, consisting of two-byte converted digital values, was transferred through PCIe to a storage device. The recording speed does not depend only on how fast the data are moved to the computer but also on write speed of the storage component itself. For example, a device with high write speed, such as a solid state drive (SSD), allows data to be saved faster than a conventional storage device such as a hard disk drive (HDD); hence, data transfers are completed quicker. In this work, most of the data were collected from two channels, one for the preamplifier output and another for the shaping amplifier output, at 20 MHz resulting in a recording speed of 80 MB/s.

The experiments in this work were performed in buffered acquisition mode in which a selectable-size block of data was buffered on the PX14400D2's RAM before being transferred to the storage component. The acquisition was paused during the data transfer period and restarted after a whole block of data was completely saved on the drive. Therefore, the write speed of the storage device affects the total recording time of the test. To lessen this time a single SSD was used for data storage in the current system because the SSD generally offers much higher performance than the HDD does.

The purpose of the experiments in this thesis is to establish the baseline performance of the system. Therefore, the current system was designed to have only a few necessary components and to operate in the simplest mode. The simple set-up of the data acquisition unit, which consists of a PX14400D2 card operating in buffered mode and an SSD, requires considerably less development time and is sufficient to accomplish the goal.

### *High-speed continuous recording system*

Although data acquisitions performs reliably in a buffered mode, the pause in acquisition during data transfer can become problematic in the experiments that require continuous data recording. Nevertheless, the acquisition system, PX14400D2 and the scope application software, can also function in continuous data acquiring. After some experimentation, it was found that the write speed of the simple storage structure was not high enough to sustain long continuous data saving especially at high sampling rate. The sampling frequency of 250 MHz resulted in a raw data throughput of 500 MB/s. PCIe technology is capable of transferring the data to the computer at this rate (250 MB/s per lane for PCIe 1.x [32], 8 lanes for a PX14400D2 card [31]); therefore, the limitation of the system is usually the speed of the storage device. An SSD generally has high read and write performance. For instance, a 1-TB solid state drive from Samsung (model MZ-7KE1T0BW) offers up to 520 MB/s sequential write speed [33]. However, the experiments suggested that the drive could not sustain its maximum speed for long continuous periods, and eventually the acquisition will stop. In addition, for long experiments a massive amount of data will be generated. For example, for an eight-hour experiment the total of 14.4 TB of disk capacity is required to store all of the raw data. Therefore, multiple disk drives are then needed to create enough storage space.

The proposed design for high-speed continuous recording system for the ultimate system is to use an array of disk drives for data storage. The data are to be written to the drives in cycles. The first block of samples is to be sent to the first drive. The next block is to be sent to the second drive in the array and so forth. After the last drive is reached, the writing process cycles back to the first drive. Although the performance of each disk may not meet the required speed, this structure provides an individual disk enough time

to manage the received data before the next set of samples arrives. This configuration can be performed by a customized software or driver, or another option is to configure the disks as RAID in which RAID controller is in charge of data management. Either way this structure is a cost-effective approach to store a large amount of data at very high speed. Low performance but high capacity disk drives can be combined in the array. For example, five 3-TB HDDs from Seagate (Model: ST3000NM0053) will form 15-TB disk space. Even though the data transfer rate of an individual drive is sustained at 175 MB/s [34], the cost is only \$100 CAD per 1 TB (from bestbuy.ca as of July 2015). The SSD is much more expensive even if, similar to the HDD, its price decreases over time. For example, a 1-TB SSD from Samsung (MZ-7KE1T0BW) costs \$800 CAD (from bestbuy.ca as of July 2015).

This design of a disk array to perform high-speed continuous data acquisition has not yet been implemented; however, this structure is definitely beneficial to future use of the system in upcoming experiments.

### **3.4 Data analysis software**

The analysis software is responsible for processing the output from the preamplifier and the shaping amplifier stored on the acquisition unit. Each digitized sample was a raw 16-bit unsigned binary number. The software analyzes the stream of data samples to find radiation pulses. These can be accomplished by processing either the preamplifier directly or the output already shaped by the analog circuit.

Most of the preliminary studies of the system were performed based on analysis of the output shaped by the analog circuit. The shaping amplifier converted the sharp rise in

the preamplifier output to a pulse which has a much higher amplitude as shown in Figure 15. As the analog shaping circuit implemented a CR-RC filter, a significant level of noise was removed from the signal. Pulse processing only involved locating the pulses that fall under specific criteria and finding the height of the pulses. The analysis procedure of the shaping amplifier output is discussed in Appendix A.

Although the shaping circuit provides some noise filtering, the ability of noise rejection of the analog filter can be limited by the electronic hardware. Some noise can still be present in the output of the shaping amplifier including microphonic noise. Alternatively, the preamplifier output can be directly digitized, and a digital filter can be applied to eliminate noise coupled in the signal. Since the data were post-processed, different types of filters can be applied to the data and the variables of the filter can be adjusted to find the most suitable filter for the characteristics of the preamplifier signal which can improve the test results.

Another approach of generating a radiation pulse and removing the periodic low-frequency noise, such as microphonic noise, is proposed. This approach is accomplished by considering the preamplifier signal before and after an event as two separate lines or curves which meet at the point of an event. However, their voltages at the meeting point are not the same and are unknown due to the distortion from the noise. An example of the microphonic effect is shown in Figure 19(a). The height of the event caused by a neutron is then equal to the difference between the estimated levels at the time prior to and after the event. When linear or quadratic regression is used to find the lines or curves that fit the data the best, these processes are mathematically equivalent to applying a finite impulse response (FIR) filter to the preamplifier output. As

shown in Figure 19(b) a sharp rise in the preamplifier is now converted to a pulse similar to the one generated by an analog shaping amplifier. The filtered output is theoretically equal to zero where there are no radiation pulses and is equal to the height of the event when a rise is present. A few variables in this process can be adjusted to match the characteristics of the preamplifier signal which will result in different filter length and coefficients. The output of the shaping amplifier is shown in Figure 19(c). The shaped pulse showed the impact of the microphonic noise which coupled through the circuit.

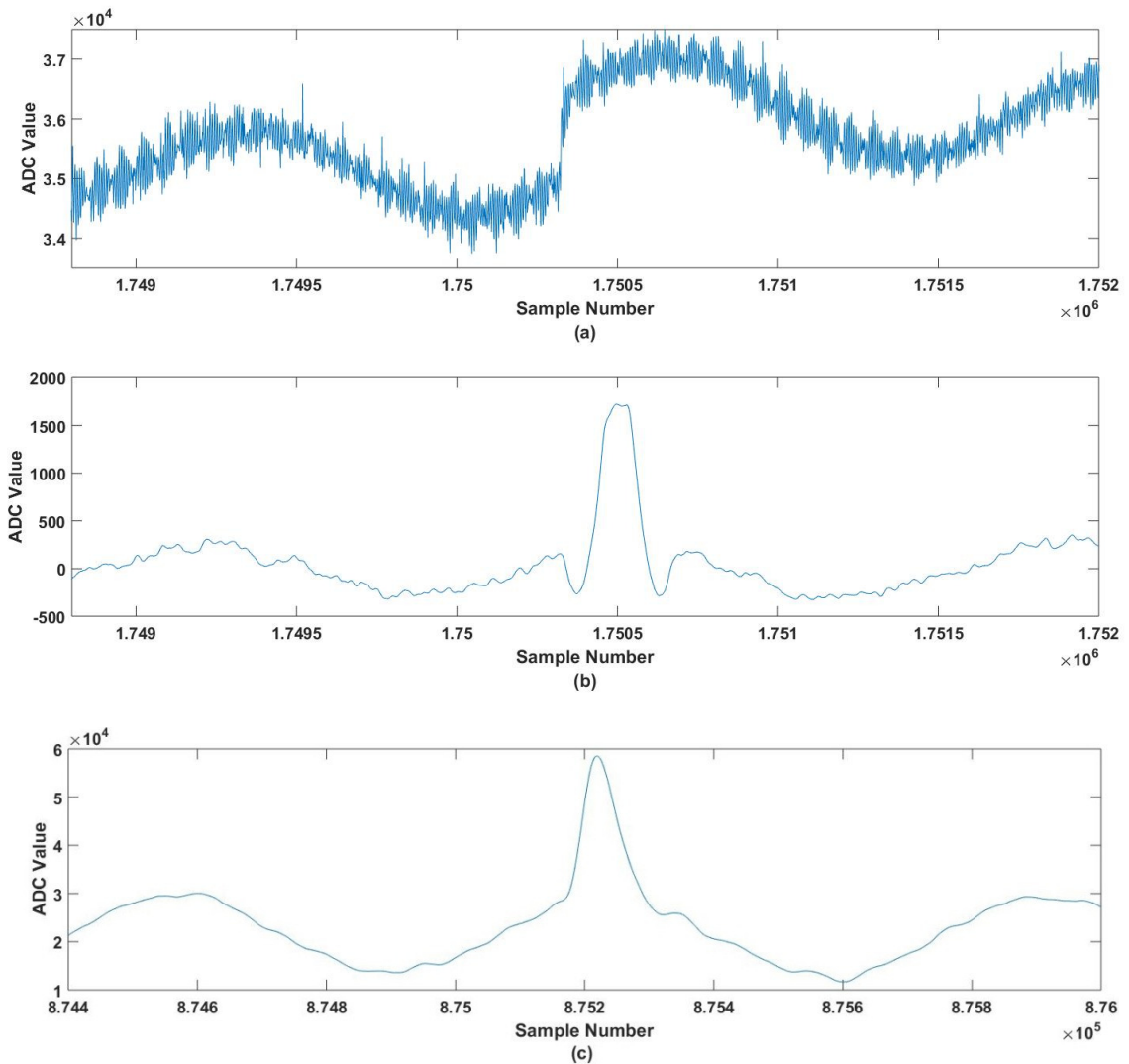


Figure 19 The preamplifier, the digitally-filtered output, and the shaping amplifier output when the microphonic noise is present (a) the preamplifier response to a test pulse (b) the digitally filtered output (c) the shaping amplifier output

The filtered output is further processed in the same steps as the analysis of the shaping amplifier discussed in Appendix A; however, the running average filter in step 1 is no longer required because the preamplifier signal is already pre-filtered. Pulse processing then includes identifying the pulse in the filtered signal and creating the spectrum (step 2

and 3).

The current system uses MATLAB to perform computations for pulse processing of both analysis methods. However, custom analysis software may be required for the future system to collect and process large amounts of data in a reasonable amount of time.

## 4 ANALYSIS OF PREAMPLIFIER SIGNAL

Due to the small Q-value of the boron-neutron interaction, a detection system that uses a high-gain charge-sensitive preamplifier, as in this work, would be sensitive to microphonic noise. The latter noise is produced by movement nearby the preamplifier, such as that induced by a moving rod in a reactor core. Such noise can, however, be suppressed by digital filtering which provides accuracy and flexibility in signal processing. A digital filter is less complicated to change its features to better suit the characteristics of signals and noises than an analog filter, which is limited by the electronic hardware. When the preamplifier signal is directly processed, a digital filter is required to eliminate this noise. This chapter introduces such a filtering approach. Filter variables were investigated using simulated test pulses.

### 4.1 Preamplifier output

The characteristics of the preamplifier signal vary depending on the detector and the circuit. For example, in the unlatched mode an event will quickly raise the output level during charge collection time similar to a step waveform. Because air is used in the detectors in this work, the collection time is approximately 20 to 40  $\mu\text{s}$ . Charge collection does not happen at an equal rate due to different mobility between electrons and negative ions. At the beginning more charges are collected so the signal presents a steeper rise. During the time where there is no neutron event and no leakage in the circuit, the signal will remain at the same level. When there is leakage in the preamplifier, a slow increase is expected in the output. Figure 20 shows a waveform of the digitized preamplifier signal. Ten samples,  $y'_4$  to  $y'_0$  and  $y''_0$  to  $y''_4$ , are taken from time

$t = 0$  to  $t = 9$ .

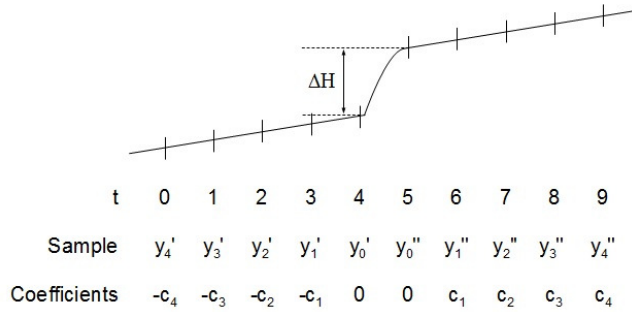


Figure 20 Digitized preamplifier waveform in unlatched reset mode. Ten data points,  $y_N'$  and  $y_N''$ , are sampled from time  $t = 0$  to  $t = 9$ . Variables  $c_i$  are coefficients of a filter.

Height of an event is equal to  $\Delta H$ .

In signal processing, the preamplifier's output pulse is digitized to capture the magnitude of the rise in each neutron event or  $\Delta H$  in Figure 20. The height of the pulse is equal to the difference between the two output levels of the preamplifier, one before and one after the event, or the values taken at time  $t = 4$  to  $t = 5$ ,  $y_0'$  and  $y_0''$  respectively. In practice, because of the system noise, the exact levels at these two locations are unknown. However, an estimate of the sample  $y_0'$  can be made by fitting a line to the samples taken prior to an event or  $y_N', y_{N-1}', \dots, y_1'$  where  $N$  is a number of samples. The same method can be done for the samples taken after the event,  $y_1'', y_2'', \dots, y_N''$ , to find an estimate of  $y_0''$ .

## 4.2 Line fitting

Line fitting can be performed by applying a least square linear regression. Each straight line can be represented by a linear equation:  $y = bx + a$ ; therefore,  $y_0'$  is the crossing

point when  $x = 0$  for the line fitted to the samples before an event while  $y_0''$  is the crossing point when  $x = 0$  for the line fitted to the samples after an event. In other words,  $y_0' = a'$  and  $y_0'' = a''$  where  $a'$  and  $a''$  are derived from the straight lines fitted to the samples before and after an event, respectively. The pulse height  $\Delta H$ , which is  $y_0'' - y_0'$ , is then equal to  $a'' - a'$ .

A least square linear regression model is used to find the line of best fit. For a straight line  $y = bx + a$ ,

$$a = \frac{\sum y}{N} - b \frac{\sum x}{N}$$

$$b = \frac{N \sum xy - \sum x \sum y}{N \sum x^2 - (\sum x)^2}$$

Thus,  $y_0'' = a'' = \sum_{i=1}^N c_i y_i''$  for the samples after an events and  $y_0' = a' = \sum_{i=1}^N c_i y_i'$  for the samples before an events where  $c_i$  is a constant for  $i = 1, 2, \dots, N$ . Therefore,

$$\Delta H = y_0'' - y_0' = a'' - a = \sum_{i=1}^N c_i y_i'' + (-c_i) y_i' \quad (4.1)$$

where the coefficient

$$c_i = -i \frac{\sum x}{N \sum x^2 - (\sum x)^2} + \frac{1}{N} \left( 1 + \frac{(\sum x)^2}{N \sum x^2 - (\sum x)^2} \right). \quad (4.2)$$

### 4.3 Effects of microphonic noise

Microphonic noise is a low frequency signal, imposed on the preamplifier's output. An example is illustrated in Figure 21. The microphonic noise was generated by an alarm sound. The detector was placed on a test bench with a noise source, which is a cell phone, positioned beside it. The signal shows the discontinuity in the sinusoid where the

output level abruptly rises from an event caused by a neutron or in this case a test pulse.

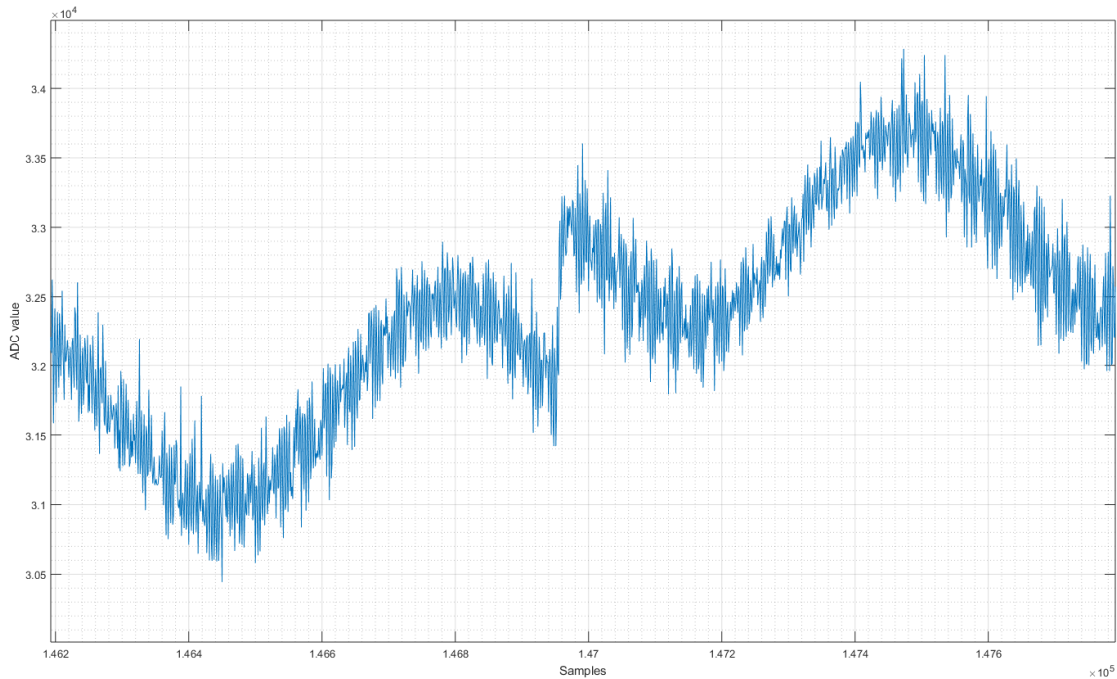


Figure 21 Pre-amplifier output to a test pulse when microphonic noise is present. The pre-amplifier operated in the unlatched mode.

If a period of time before and after an event considered in the calculation is long enough to include curves of the noise, the signal before and after an event is no longer two straight lines. In this case, using line fitting to find the pulse height will result in large error in the estimation; therefore, it is not the best option. Instead two curves, such as quadratic curves, can be fitted to two portions of the signal, one before and one after the event. The pulse height can still be calculated by finding the difference between the predicted values before and after the discontinuity, i.e.  $y'_0$  and  $y''_0$ , respectively. This method allows a radiation pulse to be found and to eliminate the effect of microphonic noise.

Similar to line fitting, curve fitting can be performed by using a least square quadratic regression. For a least square quadratic regression model,

$$a = \frac{1}{N} \sum y - \frac{1}{N} b \sum x - \frac{1}{N} c \sum x^2$$

$$b = \frac{S_{22}S_{y1} - S_{12}S_{y2}}{S_{11}S_{22} - S_{12}^2}$$

$$c = \frac{S_{11}S_{y2} - S_{12}S_{y1}}{S_{11}S_{22} - S_{12}^2}$$

where  $s_{11} = \sum x^2 - \frac{(\sum x)^2}{N}$ ,

$$s_{12} = \sum xx^2 - \frac{\sum x \sum x^2}{N},$$

$$s_{22} = \sum (x^2)^2 - \frac{(\sum x^2)^2}{N},$$

$$s_{y1} = \sum yx - \frac{\sum y \sum x}{N}, \text{ and}$$

$$s_{y2} = \sum yx^2 - \frac{\sum y \sum x^2}{N}.$$

With a similar analysis to the line fitting, the pulse height

$$\Delta H = y_0'' - y_0' = a'' - a = \sum_{i=1}^N c_i y_i'' + (-c_i) y_i' \quad (4.3)$$

where the coefficient

$$c_i = \frac{1}{k_4 N} (k_1^3 - k_2^2) i^2 + \frac{1}{k_4 N} (k_1^2 k_2 - k_1 k_3) i$$

$$+ \frac{1}{k_4 N^2} (N k_4 + k_1^2 k_3 + k_2^3 - 2 k_1^3 k_2) \quad (4.4)$$

where  $k_1 = \sum x$ ,

$$k_2 = \sum x^2,$$

$$k_3 = \sum x^4, \text{ and}$$

$$k_4 = k_2 k_3 - k_1^4 - \frac{k_2^3}{N} - \frac{k_1^2 k_3}{N} + \frac{2k_1^3 k_2}{N}.$$

Considering Equation (4.3), the pulse height equation derived for the quadratic curve fitting is exactly the same as the equation for the line fitting (Equation (4.1)) but with more complex coefficients. Choice between line fitting or curve fitting is to be made from characteristics of noise, such as its frequency, and length of time before and after an event considered in the calculation. More details are discussed later in section 4.5.4.

#### 4.4 Digital filtering

Equation (4.1) shows that the process of finding the pulse height  $\Delta H$  results in a sum of the product of the coefficients and the data samples. This is mathematically equivalent to implementation of an FIR filter:

$$y[m] = b_0 x[m] + b_1 x[m-1] + b_2 x[m-2] + \dots + b_M x[m-M] = \sum_{j=0}^M b_j x[m-j] \quad (4.5)$$

Therefore, the preamplifier pulse processing can be implemented as if the signal is filtered with a FIR filter (note that the  $x$  variable in the FIR filter notation is the  $y$  variable in the regression model). However, the filter coefficients are specifically generated. Comparing Equation (4.5) to Equation (4.1), the filter coefficients,  $b_j$  where  $j = 0$  to  $M$ , can be divided into three groups:

- $-c_i$  where  $i = 1, 2, \dots, N$

This group is the first part in the filter,  $j = 0$  to  $N - 1$ , and is applied to the first group in the data. The values of  $c_i$  are generated from Equation (4.2) and (4.4) for line fitting and curve fitting, respectively. The number of the coefficients in this group together with the sampling frequency determines the length of time for

which a line or a curve is intended to be fit to the samples. If the time is too short, not enough samples will be processed and the line or the curve could be off which will degrade the result. If the time is too long, the opportunity of running into another event will increase which can also become the cause of the incorrect result.

- 0

A number of zeros, referred to as  $k$ , are filled in the middle of the filter from  $j = N$  to  $N + k - 1$ . The purpose is to zero out the samples which are taken when the charges are still collected at the anode. This is because during the collection time the preamplifier output continues to rise and does not yet reach the maximum level. The number of zeros varies depending on how long the rise time is. For the best performance the filter should have enough zeros to cover the whole length of the collection period; for example, two zeros are needed for the diagram in Figure 20.

- $c_i$  where  $i = 1, 2, \dots, N$

This last group,  $j = N + k$  to  $M$ , has the same number of coefficients as the first. The coefficients are the negative values of the first group and are in reverse order.

The total length of the filter,  $M + 1$ , is equal to  $2N + k$ . Examples of the filter coefficients  $b_j$  are given in Table 5 for  $N = 4, 8$ , and  $16$  and  $k = 2$ . However, for most cases a longer filter,  $N \geq 128$ , are required to have better results.

Table 5 Filter coefficients  $b_j$  for  $N = 4, 8,$  and  $16$  and  $k = 2$

| j  | N = 4  |           | N = 8   |           | N = 16 |           |
|----|--------|-----------|---------|-----------|--------|-----------|
|    | Linear | Quadratic | Linear  | Quadratic | Linear | Quadratic |
| 0  | 0.5    | -0.75     | 0.25    | -0.375    | 0.125  | -0.1875   |
| 1  | 0      | 1.25      | 0.1429  | 0.0536    | 0.1    | -0.0875   |
| 2  | -0.5   | 0.75      | 0.0357  | 0.3036    | 0.075  | -0.0054   |
| 3  | -1     | -2.25     | -0.0714 | 0.375     | 0.05   | 0.0589    |
| 4  | 0      | 0         | -0.1786 | 0.2679    | 0.025  | 0.1054    |
| 5  | 0      | 0         | -0.2857 | -0.0179   | 0      | 0.1339    |
| 6  | 1      | 2.25      | -0.3929 | -0.4821   | -0.025 | 0.1446    |
| 7  | 0.5    | -0.75     | -0.5    | -1.125    | -0.05  | 0.1375    |
| 8  | 0      | -1.25     | 0       | 0         | -0.075 | 0.1125    |
| 9  | -0.5   | 0.75      | 0       | 0         | -0.1   | 0.0696    |
| 10 |        |           | 0.5     | 1.125     | -0.125 | 0.0089    |
| 11 |        |           | 0.3929  | 0.4821    | -0.15  | -0.0696   |
| 12 |        |           | 0.2857  | 0.0179    | -0.175 | -0.1661   |
| 13 |        |           | 0.1786  | -0.2679   | -0.2   | -0.2804   |
| 14 |        |           | 0.0714  | -0.375    | -0.225 | -0.4125   |
| 15 |        |           | -0.0357 | -0.3036   | -0.25  | -0.5625   |
| 16 |        |           | -0.1429 | -0.0536   | 0      | 0         |
| 17 |        |           | -0.25   | 0.375     | 0      | 0         |
| 18 |        |           |         |           | 0.25   | 0.5625    |
| 19 |        |           |         |           | 0.225  | 0.4125    |
| 20 |        |           |         |           | 0.2    | 0.2804    |
| 21 |        |           |         |           | 0.175  | 0.1661    |
| 22 |        |           |         |           | 0.15   | 0.0696    |
| 23 |        |           |         |           | 0.125  | -0.0089   |
| 24 |        |           |         |           | 0.1    | -0.0696   |
| 25 |        |           |         |           | 0.075  | -0.1125   |
| 26 |        |           |         |           | 0.05   | -0.1375   |
| 27 |        |           |         |           | 0.025  | -0.1446   |
| 28 |        |           |         |           | 0      | -0.1339   |
| 29 |        |           |         |           | -0.025 | -0.1054   |
| 30 |        |           |         |           | -0.05  | -0.0589   |
| 31 |        |           |         |           | -0.075 | 0.0054    |
| 32 |        |           |         |           | -0.1   | 0.0875    |
| 33 |        |           |         |           | -0.125 | 0.1875    |

#### 4.5 Filter variables

The performance of the detector depends on four important variables: rise time of the preamplifier, time extended from the point of the event to apply line/curve fitting,

sampling frequency, and length and type of the filter.

#### **4.5.1 Rise time of the preamplifier**

The preamplifier output increases during the rise time, due to the charge collection process in the detector. The length of the rise time depends on the characteristics of the system, such as the geometry and materials of the detector and the design and part specification of the preamplifier circuit. In this work, the rise time ranged from 20  $\mu\text{s}$  to 35  $\mu\text{s}$ . To capture the full height of the radiation pulse and minimize error in the calculations, this period should be excluded from line/curve fitting. The samples used to fit the line/curve before an event should end right before the output starts to rise from the event. Similarly, the samples after the event that are taken into the calculation should start right after the charge collection is finished. Rise time must be estimated to an appropriate length. If the estimated time is too short, part of the line/curve fitting will use some false data samples which can result in a line or curve that deviates from what it should be. Consequently, the calculation will lead to an incorrect pulse height. On the other hand, if the samples are eliminated for too long of a period, the level of the preamplifier output may drift or distort to lower or higher level from the leakage or noise. Hence, the calculated value of  $y'_0$  or  $y''_0$  becomes incorrect. The rise time must then be estimated to an appropriate length for a specific system of interest.

Because the pulse height calculation is implemented as an FIR filter, data points during the rise time can be eliminated by padding a number of zeros in the middle of the filter between two sets of coefficients for two line/curve fittings. When the signal is filtered, the data samples during the rise time will be multiplied with zeros and removed from the

calculation. The number of zeros in the filter  $k$  is determined by the sampling frequency and the length of the rise time, or

$$k = (\text{Rise time} * \text{Sampling frequency}) - 1$$

For example, if the rise time lasts 40  $\mu\text{s}$  and the samples are taken at 1 MHz, 39 zeros are required in the filter or  $k = 39$ .

#### 4.5.2 Time for line/curve fitting on each side of the event

Considering a case of line fitting, theoretically all the data points before and after the event will perfectly position on two fitted lines. Therefore, only two data points from each side of an event are enough to derive the line equation. The two samples can be taken at any time apart, so they can be close to each other and that still does not affect the accuracy of the equation. However, because data samples always inherit some system noise such as white noise or digitization noise, using only two points is not sufficient to find the true fitted line. The slope or the constant of the line equation can be inaccurate because one or both of the data points is affected by fluctuations. Therefore, data samples taken for a period of time before and after the event, referred to as  $t_a$  and  $t_b$ , respectively, are needed in the calculation in order to eliminate this data fluctuation and increase the accuracy of the line equation. These two time periods  $t_a$  and  $t_b$  are equal to keep a symmetrical duration around an event in the analysis. The times  $t_a$  and  $t_b$  relate closely to the sampling frequency and the number of coefficients  $c_i$  or  $N$ . The relationship between the three variables can be written as:

$$t_a = t_b = \frac{N}{\text{sampling frequency}} \quad (4.6)$$

For example, when the sampling frequency is 1 MHz, the samples are taken every 1  $\mu\text{s}$ . If the line is fitted to 128 samples before and 128 samples after an event, time period  $t_a$

taken to derive the line from the first sample  $y'_N$  to where the start of the event  $y'_0$  supposedly takes place is equal to  $128 \mu\text{s}$ . Similarly, the period between where the rising output from an event ends or  $y''_0$  and the last sample  $y''_N$  used in the line fitting calculation,  $t_b$ , is also  $128 \mu\text{s}$  long.

To investigate the effect of this variables, test pulses with a height of a DAC arbitrary unit of 8 were introduced to the system every 1 ms. Figure 22 shows a plot between this time and the FWHM of the filtered test pulses for the system. The preamplifier output was sampled at 1 MHz, and linear regression was used in the pulse processing. The FWHM on the y axis was normalized by the maximum counts. For a fixed sampling frequency at 1 MHz the time  $t_a$  and  $t_b$  is equal to the value of  $N$  on the x axis in microseconds, e.g. at  $N = 32$ ,  $t_a = t_b = 32 \mu\text{s}$  and so forth. From the plot, the most suitable time for  $t_a$  and  $t_b$  for this system is  $128 \mu\text{s}$  which is the lowest tip on the graph. When the time is too short, there is not enough samples to eliminate fluctuations in the data; therefore, the variation in the result is higher. On the other hand, the longer  $t_a$  and  $t_b$  can potentially include the samples that do not fit well on the derived line due to noise or distortion in the signal; hence, the FWHM is also wider than the optimum point.

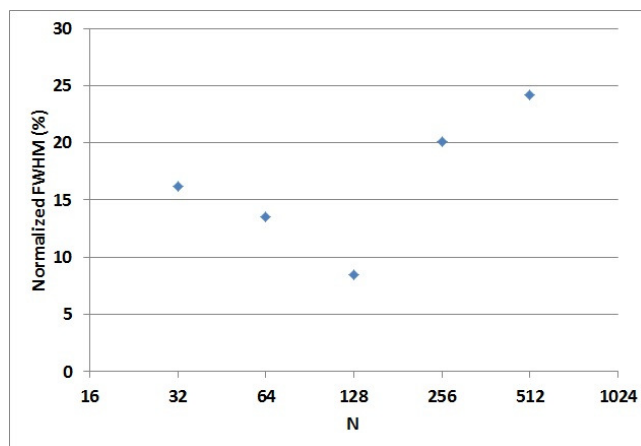


Figure 22 FWHM normalized by the maximum count versus the size of  $N$  at sampling frequency of 1 MHz

Choosing the best time for  $t_a$  and  $t_b$  does not depend only on the FWHM of the processed pulses, but also on the maximum count rate the system can be used. The total processing time to effectively resolve a pulse using this filtering technique is equal to the sum of  $t_a$ ,  $t_b$ , and the rise time. Because the rise time cannot be reduced, the maximum count rate is limited by the time used to fit the line/curve on each side of the pulse. Even though the long period of  $t_a$  and  $t_b$  may lower the FWHM, the system will not be able to work with a high count rate. The time separation between two successive events should be at least equal to the processing time in order to recognize a single pulse. For example, for a system having

- sampling frequency = 1 MHz
- rise time = 40  $\mu$ s
- $t_a = t_b = 128 \mu$ s

the time between pulses must be at least  $128 + 40 + 128 = 296 \mu$ s. The system can then operate only if the count rate is less than approximately 3400 counts/s or approximately

$113 \times 10^3$  counts/cm<sup>2</sup>/s if 3-mm<sup>2</sup> boron in the detector. If one in 1000 neutrons is detected, the maximum neutron flux is only as high as approximately  $1 \times 10^8$  neutrons/cm<sup>2</sup>/s. If the time  $t_a$  and  $t_b$  are shortened to 32  $\mu$ s, the maximum neutron flux will increase to approximately  $3 \times 10^8$  neutrons/cm<sup>2</sup>/s. The processing time of 100  $\mu$ s is comparable to the current analog shaping amplifier.

To allow the system to work at the high count rate with a shorter time in the line/curve fitting, degradation in FWHM can be compensated for by increasing the sampling frequency. The line or curve will be derived from a sufficient number of samples to eliminate the fluctuation in the data points.

#### **4.5.3 Sampling frequency**

Another important variable that affects the filter's performance is the sampling frequency. Raising the frequency at which the data is taken will increase the number of samples used in the line/curve fitting which will result in better elimination of the effect of fluctuation in the data. Consequently, the derivation of lines or curves will be more accurate. However, if the sampling frequency is sufficiently high and enough samples are already used in the algorithm, adding more samples to the calculation will provide no further improvement to the results. The plot in Figure 23 shows the FWHM of the test pulses when the sampling frequency increased. The time period in the line fitting was fixed at 32  $\mu$ s and the number of coefficients were changed corresponding to the sampling frequency. Sampling frequencies higher than 2 MHz did not show significantly improvement in the results. FWHM remained at 11% to 13% for the sampling frequencies of 2 MHz to 32 MHz. It was unclear from available information whether

FWHM increased toward higher frequencies. The changes were relatively small and possibly resulted from statistical variations. FWHM at 4 MHz was also strangely high. Causes of this anomaly could not yet be determined.

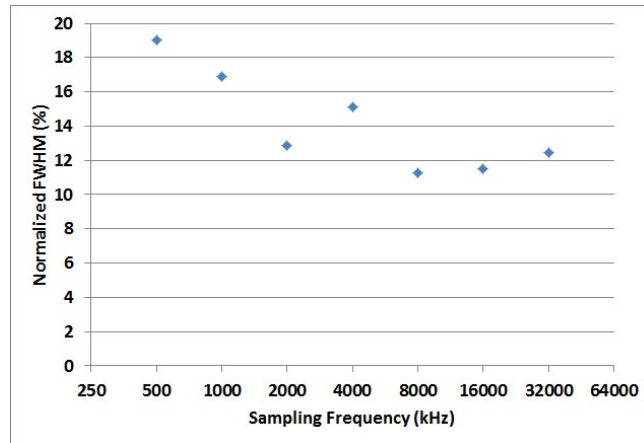


Figure 23 FWHM versus sampling frequencies for  $t_a$  and  $t_b$  of 32  $\mu$ s

According to Equation (4.6), if the time period in the line fitting is fixed, the number of coefficients  $c_i$  or  $N$  must be changed proportionally to the sampling frequency. For example, for the time period of 32  $\mu$ s before and after the rise in the calculation, if the sampling frequency is raised from 1 MHz to 16 MHz,  $N$  must be increased from 32 to 512 which will lead to more multiplication terms in the filtering process.

Although increasing the sampling frequency helps improve the FWHM, the downside is that more resources are required. Firstly, the data acquisition unit must be able to carry out the digitization at high sampling rate. Secondly, the more calculation in the filtering process will also require more processing power and resource.

#### **4.5.4 Length and type of filter**

The length of the filter is the total number of coefficients, which is equal to  $2 * N + k$ . Because the rise time is an unchanging factor for a given system,  $k$  is a constant. Thus, the filter's length depends on  $N$ . The longer filter has the larger number of  $N$  which means the longer length of time accounted for in the line/curve fitting (the sampling frequency is considered unchanged). This length of time may cause one type of filter to be more suitable to the characteristics of a signal more than another. When a short period of time is considered, data samples are more likely follow a line rather than a curve. Therefore, a filter with coefficients from the linear regression model are preferred to one with the coefficients from the quadratic regression model. When the time is extended longer, the signal taken in the calculation starts to bend from the low frequency noise. In this case, a filter with quadratic regression model will be more attractive.

#### **4.6 Design for real-time processing**

Although this system was designed for experimental data to be post-processed, this algorithm can be applied in a real-time application through implementation of an FIR filter. One of the FIR filter hardware designs is to implement distributed arithmetic technique on an FPGA, as discussed in reference [35]. According to Equation (4.5), an FIR filter is the sum of the multiplication terms between the data points and the coefficients. In other words, the FIR processing function is the Multiply and Accumulate (MAC) function which can be efficiently implemented by using Serial Distributed Arithmetic (SDA) technique on an LUT-based FPGA [35]. This technique utilizes shift registers or RAM-based shift registers to store digitized data samples which is the preamplifier's output. A new sample is loaded to a register after a number of clock that are equal to a number of bits in each sample, e.g. for 16-bit data points a new sample is

loaded every 16<sup>th</sup> clock. The number of shift registers in the design is equal to the length of the filter which is  $2 * N + k$ . A Look-up Table (LUT) in the design is made up of all possible partial sums of the filter coefficients  $b_j$  which are constant derived from line/curve fitting algorithm. Due to a large number of filter coefficients, multiple LUTs can be implemented to avoid a single large LUT which is quite costly. This implementation of the algorithm allows its performance to be enhanced by pipelining and parallelism if less processing time is required for real-time processing of the preamplifier's output.

In summary, a height of a radiation pulse can be directly derived from the digitized preamplifier's signal by using the line/curve fitting algorithm. The algorithm is expected to reduce the effect of microphonic noise which could propagate through a traditional analog shaping circuit. Variables in the algorithm must be chosen to match the characteristics of the signal and noise. Since the algorithm is mathematically equivalent to an FIR filter, it lends itself well to an FPGA implementation using distributed arithmetic technique if real-time pulse processing is needed.

## **5 PRELIMINARY EXPERIMENTAL RESULTS**

A number of experiments were performed during the initial study of the system to evaluate the system's operation and establish its capability. The detection system was tested in pulse mode with an alpha source, a gamma source, and outside of the reactor core. The first evaluation of the detection system was an alpha exposure. The purpose of the test was to verify whether the system was able to operate as an ionization chamber and identify a radiation event. Next, the system was tested with a gamma source in order to observe its sensitivity to gamma rays when operating in pulse mode with an unlatched reset. Finally, the system was tested in a dry PVC pipe located approximately 0.5 m from the TRIGA reactor. This set-up provided an opportunity to study the system in the environment similar to an in-core experiment but without assembly and installation complications. In this test, attention was given to the output of the shaping amplifier, because it provided the shaped and amplified signals that are amenable to digitization and analysis. The signal was digitized by the PX14400D2 digitizer card at a sampling rate of 20 MHz in the buffered mode. The data were transferred to the solid state drive for post-analysis using MATLAB.

### **5.1 Exposure to an alpha source**

When boron is used as a target material for neutron capture, one of the resulting products from the reaction is an alpha particle. Therefore, the first simple test to verify the function of the detector and the electronic system is to test directly to an alpha source. The objective was to identify whether electric pulses were generated from alpha particles and whether these pulses were amenable to the analysis. The experiment was

performed in two configurations: one was to maximize the path length of alpha particles in the detector volume and another was to direct alpha particles into the detector in the similar direction to actual alpha particles generated from the neutron capture by boron.

The actual alpha particle generated from the neutron-boron interaction has a maximum energy of 1.47 MeV, which loses approximately 200 keV per mm when travelling in air (which is also the gas used in the detector) [24]. The longest possible range an alpha particle with this maximum energy can travel in air is then equal to 7.35 mm, and it would lose all 1.47 MeV of energy inside the detector. However, due to the small size and the cylindrical geometry of the detector, a simple two-dimensional model, as shown in Figure 9(b), suggests that the longest path available, which is the diagonal length from the center of the 2-mm boron disc to the anode wire at the end of the active volume, is 6.55 mm long. Therefore, approximately only 1.31 MeV of energy is potentially the maximum energy that will be absorbed in the detector.

The alpha source used in the experiment was Americium-241 (Am-241), which emits 5.4-MeV alpha particles. Alpha particles at this energy lose approximately 100 keV per mm in air [24]. The source was placed in two different positions as shown in Figure 24: at the open end of the detector (a) and at the 2-mm hole in the middle of the active volume (b). The detector used in the experiment was the detector A which was made of pure copper without any boron. The external high voltage power supply provided a voltage of  $-300$  V to the detector. The preamplifier operated in pulse mode with the latched reset, i.e. the feedback resistor was connected.

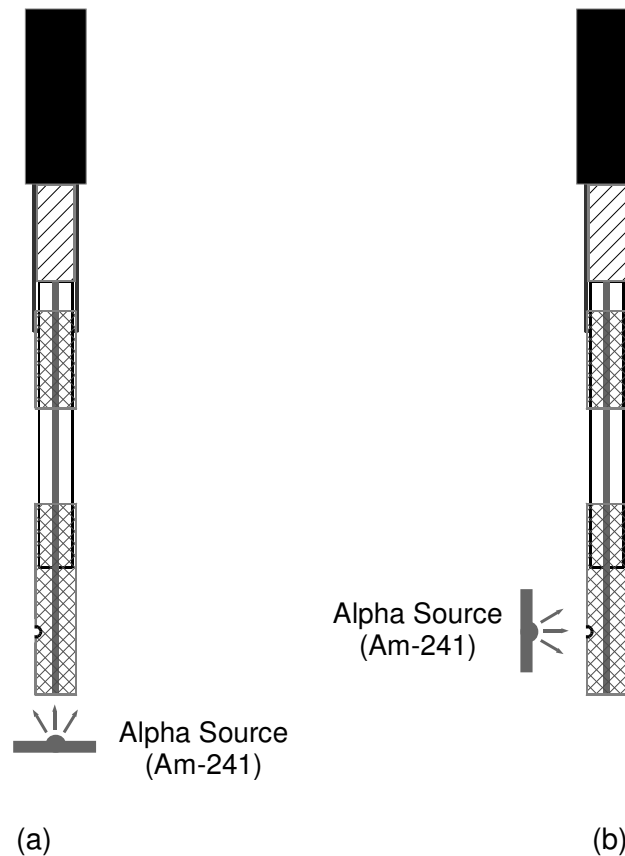


Figure 24 The alpha source, Am-241, was placed at two positions: (a) at the open end of the detector and (b) at the 2-mm hole in the middle of the active volume.

At the first position the alpha particles travel lengthwise inside the detector. The particles travelling in parallel to the detector's wall and reaching the full length of 12.7 mm lose 1.27 MeV in the detector. This energy is almost the same level as the potential maximum energy of the actual alpha particle released from the neutron capture process. Therefore, this test simulated the best case in which the highest amplitude pulse was expected from the neutron detector. Figure 25 shows an example of the preamplifier and the shaping amplifier output when the alpha source was placed at the open end of the detector. Ten seconds of data was collected and the pulse height distribution is shown in Figure 26. The threshold was set at ADC arbitrary unit of 24500 and the minimum

distance between consecutive pulses was 30  $\mu\text{s}$ . This threshold level eliminated most of the system noise in the shaped output.

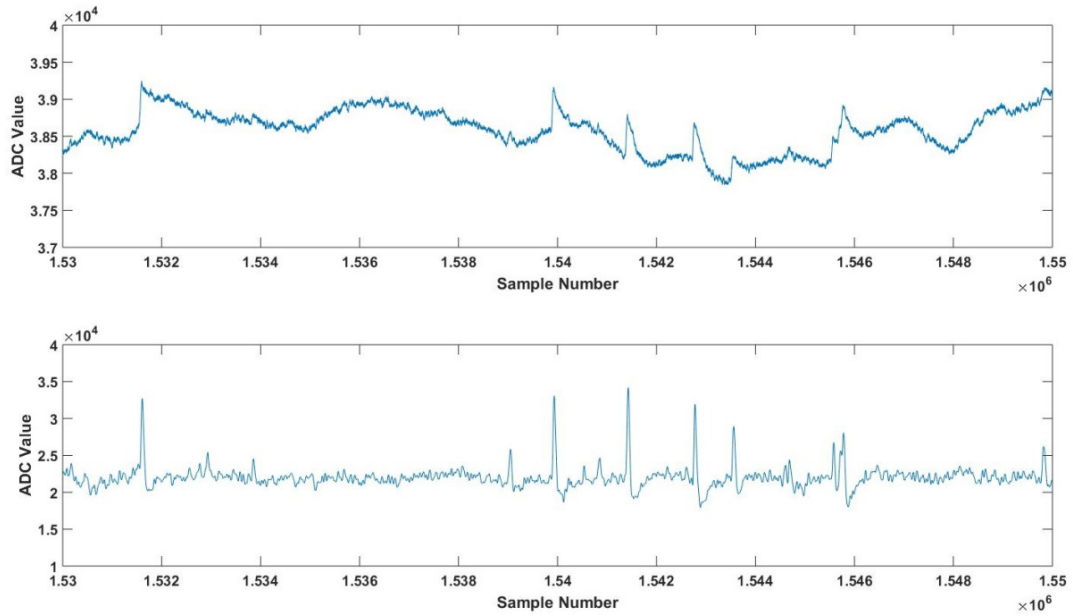


Figure 25 The output of the preamplifier (top) and the shaping amplifier (bottom) when the alpha particle travelled lengthwise inside of the detector.

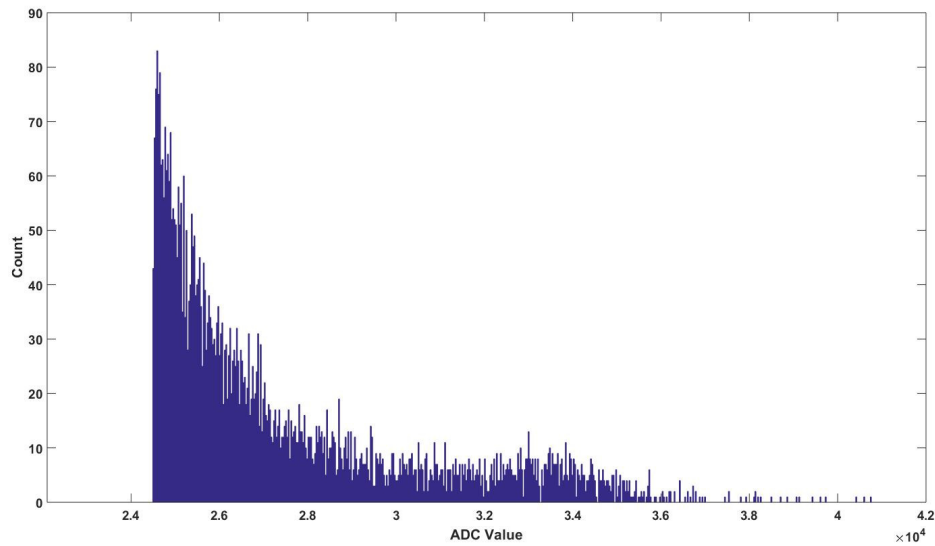


Figure 26 Pulse height distribution of the shaping amplifier output when the detector was exposed to the Am-241 alpha source. The source was placed at the open end of the detector.

When the alpha source was placed at the 2-mm hole of the detector, the alpha particles travel inside of the detector through the hole. This setup provides the closest test condition to the actual direction of the alpha particle emitted from the boron-neutron interaction; however, a smaller pulse size is expected for the same travel path due to the higher energy of the particle. An example of the outputs of the preamplifier and the shaping amplifier are provided in Figure 27. The pulse height distribution of the shaped output for 10-second test was also shown in Figure 28. The same criteria, i.e. threshold level and minimum time between consecutive pulses, were used in the pulse recognition process.

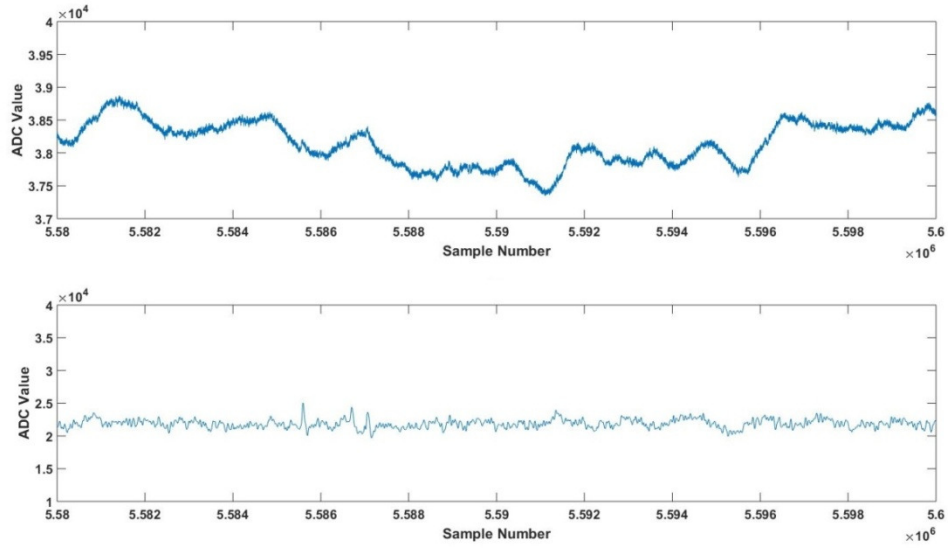


Figure 27 The output of the preamplifier (top) and the shaping amplifier (bottom) when the alpha source was placed to emit the particle through the 2-mm hole of the detector.

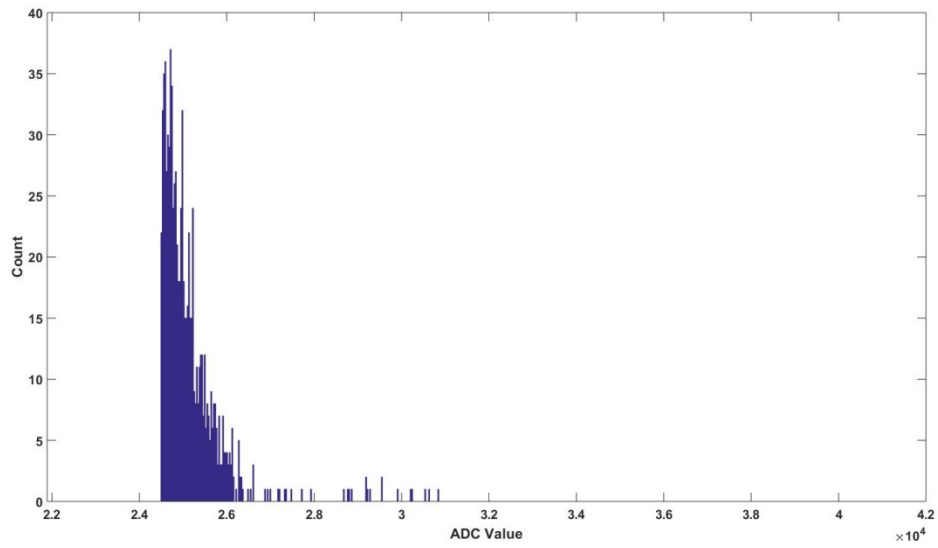


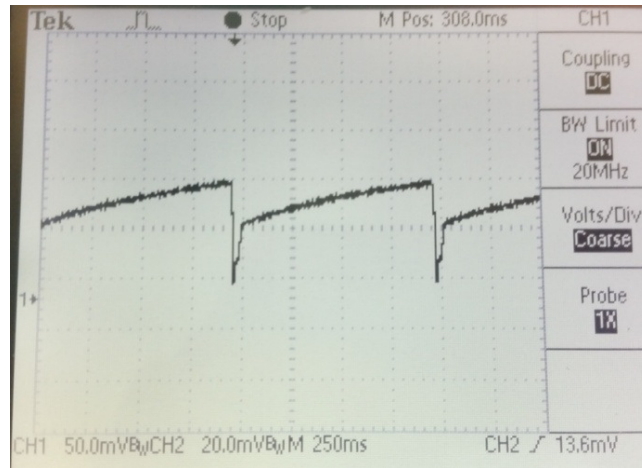
Figure 28 Pulse height distribution of the shaping amplifier output when the detector was exposed to the Am-241 alpha source. The source was placed at the 2-mm hole in the middle of the detector volume.

In conclusion, the detection system was able to identify the pulses generated by alpha particles emitted by the alpha source placed in both positions. Therefore, the system should also be able to detect alpha particles generated by the actual neutron conversion process.

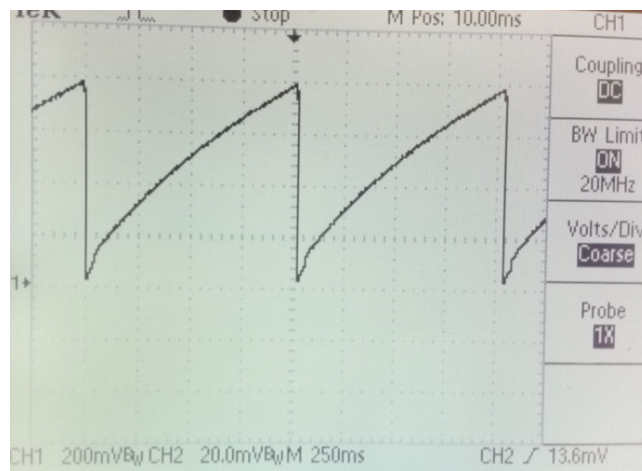
## **5.2 Exposure to a gamma source**

The purpose of the test with a gamma source was to evaluate the operation of the preamplifier when the reset mechanism was unlatched (the feedback resistor was not connected). It is then expected that when the detector was exposed to a gamma source, the secondary electrons would generate charges, producing an electronic signal that should be low in magnitude because of the low energy deposited in the detector compared to that of an alpha particle or a lithium recoil. In practice, the leakage in the preamplifier can cause an increased voltage that appears similar to that produced by gamma radiation. However, the output should be a lower-rate signal than when a gamma source is present.

A cesium-137 (Cs-137) source with an activity of 217.19 GBq (5.87 curies) were used in the experiment with detector B. Here, the preamplifier output was observed. Before exposure to the gamma source, the preamplifier output rose at a rate of 50 mV/s as a result of the leakage current. The rate increased to 600 mV/s when the source was present. Figure 29 (a) and (b) show the preamplifier output with and without the gamma source, respectively. During the test the preamplifier was set up to reset at an equal intervals of one second. The reset brought the output level back down to the baseline voltage.



(a)



(b)

Figure 29 The preamplifier output (a) when the gamma source was not present (b) when the detector was exposed to the Cs-137 gamma source.

The preamplifier output did not display a sign of sensitivity to the gamma source of this activity (217.9 GBq) when the reset mechanism was latched. When the source was present, the baseline of the output did not change.

### 5.3 Testing outside of the reactor core

One necessary step to test a system before acquiring measurements in a reactor core is to check its performance in a similar environment but outside the reactor core. Therefore, detector B and the electronics were placed in a large dry PVC tube located approximately 0.5 m from the edge of the core. This setup allowed the detector to be subjected to neutron and gamma fields that resemble those inside the core but a much lower intensity. Mechanical assembly failure and installation complications were also avoided. The detector was positioned at the bottom of the tube. The electronics was approximately 1.5 m above it. A long cable of 27 m connected the electronics to the data acquisition unit located further away at a safe distance from the reactor.

A high voltage of  $-350$  V was provided to the detector by the power supply (Tennelec TC950). The test was performed at several different reactor power levels. As the power increased, the detector would be subjected to higher rates of neutron and gamma ray exposures. However, the system was tested at low reactor power to allow the preamplifier to operate in pulse mode and prevent pulse pile-up as much as possible. In the prior experiments (not included in this thesis), it was found, by observing the height of the shaped output on the oscilloscope, that when the reactor operated at the power of 100 kW or higher, there were occasionally some pulses occurring on the tail of another pulse or pulses with much larger height than others. These pulses appeared more often as the reactor power increased. Therefore, the reactor power of 10 kW and 50 kW were chosen for the experiment to avoid these conditions. Table 6 lists the test conditions used in these experiments. The preamplifier with the unlatched reset was tested at 10 kW to find its operation in presence of neutron and gamma fluxes. However, in other out-of-core experiments, the preamplifier operated with latched reset to avoid saturation in

the output. The system was studied at both power levels, and the pulse height distributions were derived. The system noise were also investigated at both power levels. The test pulse generator was turned on in order to generate pulses with consistent height for analysis.

Table 6 Reactor power and modes of the system in the experiments outside of the reactor core

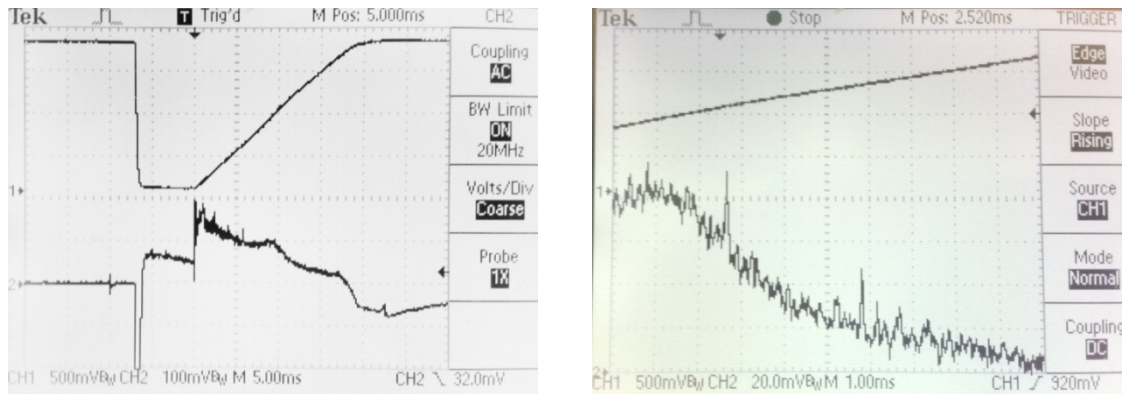
| Test no. | Reactor power | Preamplifier mode            | Test pulse generator |
|----------|---------------|------------------------------|----------------------|
| 1        | 10 kW         | Pulse mode – Unlatched reset | Off                  |
| 2        | 10 kW         | Pulse mode – Latched reset   | Off                  |
| 2'       | 50 kW         | Pulse mode – Latched reset   | Off                  |
| 3        | 10 kW         | Pulse mode – Latched reset   | On                   |
| 3'       | 50 kW         | Pulse mode – Latched reset   | On                   |

### 5.3.1 Results at steady-state power of 10 kW

The preamplifier operated in the unlatched mechanism during this test. The purpose was to examine whether this mode was able to detect neutrons in a high radiation environment and gamma background. The results are shown in Figure 30. The preamplifier and the shaping amplifier were on channel 1 (the top signal) and on channel 2 (the bottom signal), respectively. The reset command was issued by the microcontroller at a specific interval of 1 s to restore the preamplifier to its baseline potential. The reset time corresponded to the falling edge on the plot. After the reset the system started to respond to the neutron and gamma radiation as seen from the increasing voltage of the preamplifier. This slope was the result from the background gamma radiation found in the proximity of the reactor which made the preamplifier reach saturation quickly. Because the reset was performed at a specific period, the system provided no further information until the preamplifier was reset. One of the solutions to

avoid this issue is to implement the automatic reset mechanism which is triggered based on the level of the preamplifier output.

In the plots of Figure 30(a) the neutron event could not be identified from the preamplifier signal due to the scale of the display. However, with enlarged scale the shaping amplifier in the other channel, refer to Figure 30(b), showed that the neutron event was noticeable. This corresponded to the peaks in the plot after the reset was performed and before the saturation was reached.



(a)

(b)

Figure 30 Result from the test outside of the reactor operating at 10 kW. (a) Channels 1 and 2 shows the preamplifier and the shaping amplifier, respectively. (b) Close-up of the signals where the neutron pulses could be identified from the peaks in the shaping amplifier signal.

### 5.3.2 Results at 10 kW and 50 kW

The purpose of the test was to study the pulse-height distribution at different reactor power levels. During the test, a motor and pumps that circulate water in the reactor pool

to a heat exchanger were turned off except the diffuser to lessen the noise found in the output of the shaping amplifier which was used in the analysis. Since the analog shaping amplifier was not able to filter these noises, in future experiments it is recommended to test and evaluate the algorithm discussed in Chapter 4 as an alternative method to generate a radiation pulse directly from the digitized preamplifier. With the motor and pumps turned off, cooling was provided by natural convection [36]. With approximately 400 m<sup>3</sup> of water in the reactor pool, the pool temperature will increase at a rate of 4 degree Fahrenheit per hour at 1 MW reactor power [36].

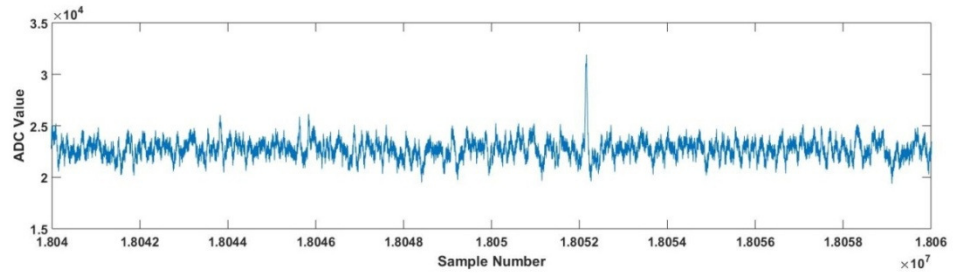
Due to high gamma background radiation, the preamplifier operated in the latched reset in order to avoid saturation. The outputs were recorded by the PX14400D2 digitizer under the settings shown in Table 7. Channel 1 was connected to the preamplifier output, and channel 2 was connected to the shaping amplifier output.

Table 7 PX14400D2 settings for the test outside of the reactor core at 10 kW and 50 kW

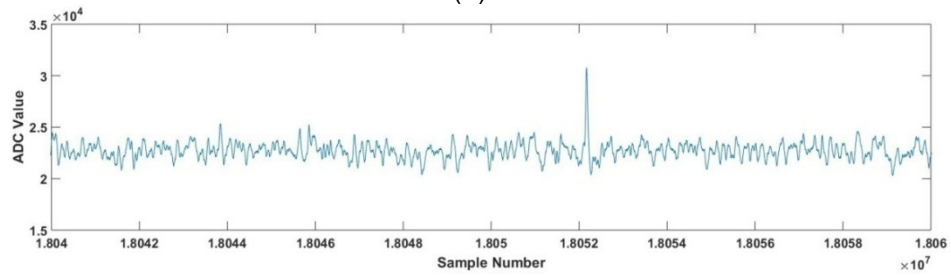
| Setting            | Value   |
|--------------------|---|
| Sampling frequency | 20 MHz  |
| Input range        | Channel 1, 2: 200 mV <sub>p-p</sub>                                       |
| DC offset          | Channel 1, 2: 1791 ADC units  |
| Trigger            | Channel 2 at the level of 25500 ADC units<br>Post trigger with no segment |
| Acquisition mode   | RAM-buffered mode with a sample block size of 134,214,728 samples.        |
| Total duration     | 30 seconds  |

Before analyzing the output of the shaping amplifier, the data were down sampled from 20 MHz to 1 MHz using MATLAB by preserving every 20<sup>th</sup> sample of the output and discarding others. Following the pulse processing steps described in Appendix A, the shaped output was first filtered by an 32-tab running average to smooth out the high

frequency component, such as white noise. A portion of the original and filtered signals taken at 10 kW and 50 kW is shown in Figure 31 and Figure 32, respectively.

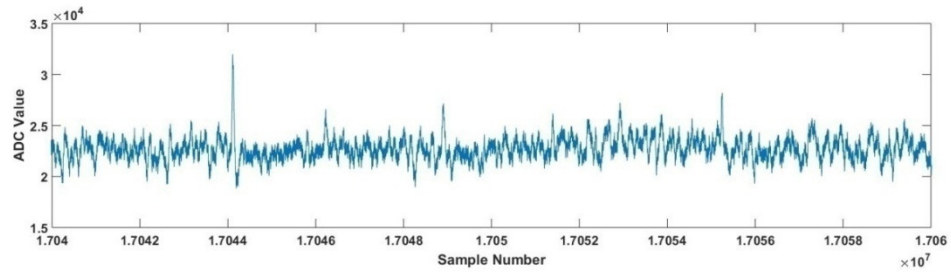


(a)

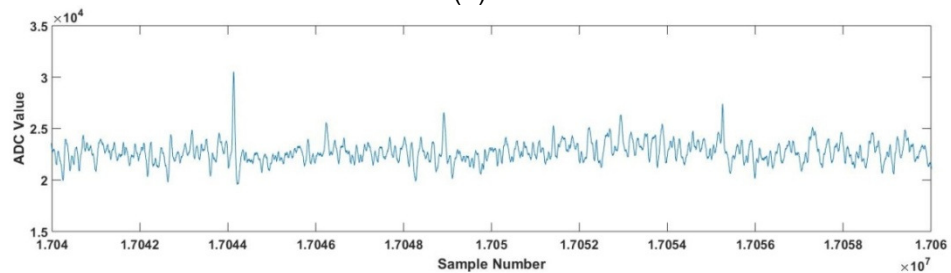


(b)

Figure 31 Shaping amplifier signals at 10 kW (a) original output (b) filtered output



(a)



(b)

Figure 32 Shaping amplifier signals at 50 kW (a) original output (b) filtered output

The second step was to identify pulses. Using a built-in function in MATLAB, *findpeaks()*, the pulses were identified using two criteria:

- the height of the pulse had to be greater than or equal to a threshold of 24500 ADC units to provide a wide spectrum as a starting point, and
- the time from the neighbouring pulses had to be greater than or equal to 30  $\mu$ s for the output of the shaping amplifier circuit with a time constant of 10  $\mu$ s.

The spectrum was then created from the identified pulses. The ADC voltage range between 20000 and 50000 ADC units were equally divided into 1000 intervals. Depending on the height of the pulse, the count in the corresponding bin was incremented. The spectra or the pulse height distributions for the 30-second test at 10-kW and 50-kW are shown in Figure 33. The two spectra exhibited similar characteristics, two of which were the numerous counts in the low pulse height region and the pulses with the height greater than 26000 ADC units.

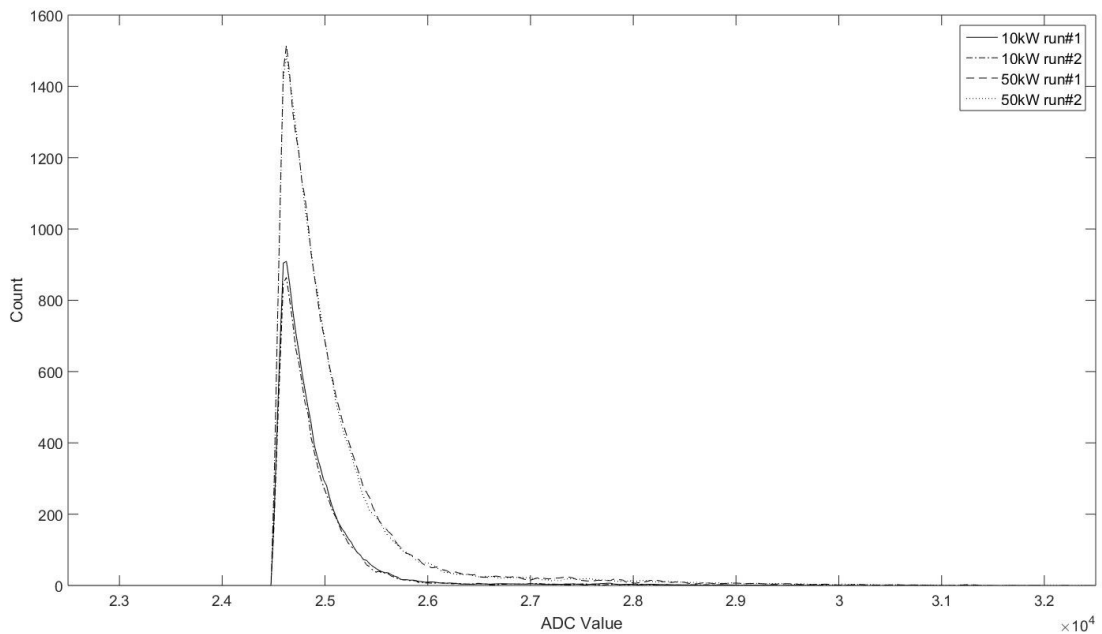


Figure 33 Pulse height distribution at 10 kW and 50 kW

The number of pulses with low pulse height increased with the power reactor. For example, there were approximately 900 pulses with the height of 24700 ADC unit when the reactor operated at 10 kW. The number increased to approximately 1500 pulses when the power was raised to 50 kW. The assumption is these pulses were produced by gamma rays. Even though the system operating in the latched reset mode was not sensitive to a caesium source of 217.9 GBq (5.81 curies), according to section 5.2, it could be affected by a much stronger and a wider range of energy of gamma fluxes in the reactor. An example of gamma spectrum in the reactor generated by MCNP simulations by Jan Vermaak is shown in Figure 34 [37]. Because gamma rays are generated by the reactor, the higher the power is, the more gamma rays are detected. However, fission in the reactor is not the only source of gamma rays. They can also be generated from decay of fission products and activated elements in the reactor core. As

a result, the number of gamma pulses were not increased by the same factor as the reactor power. This assumption was later investigated during the in-core experiment discussed in section 6.4.

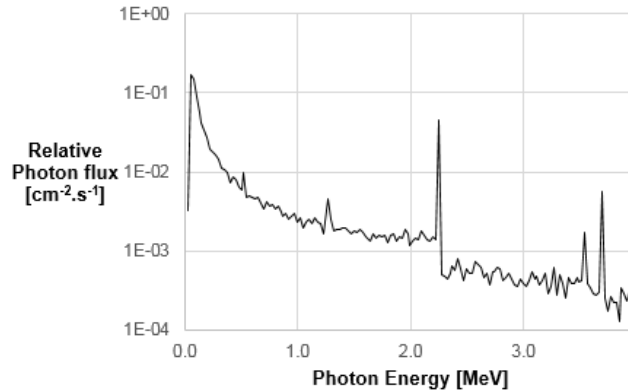
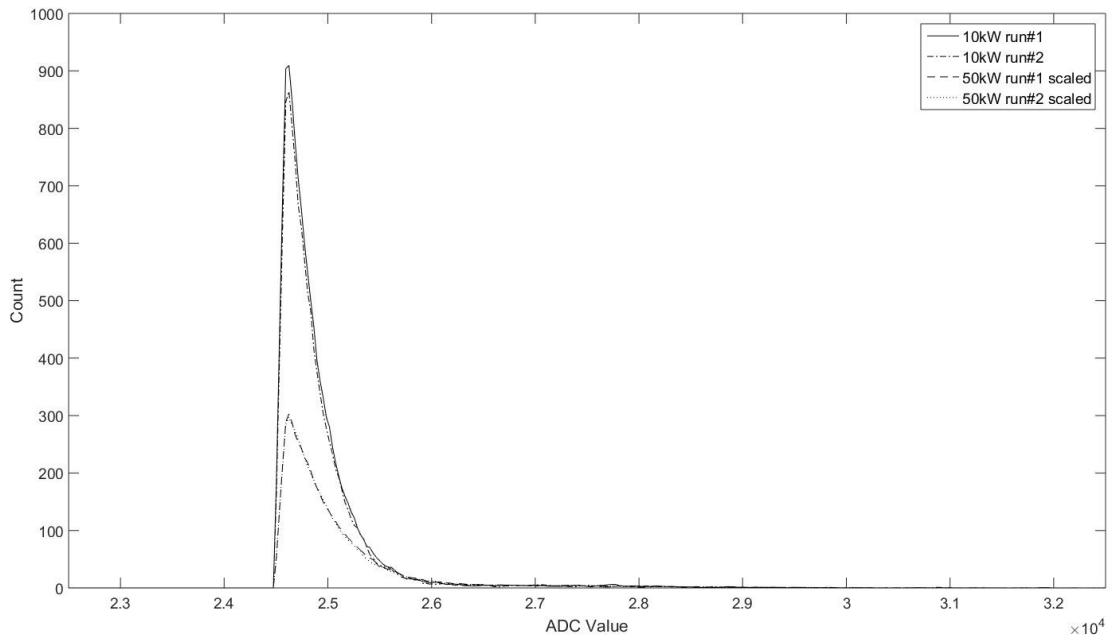
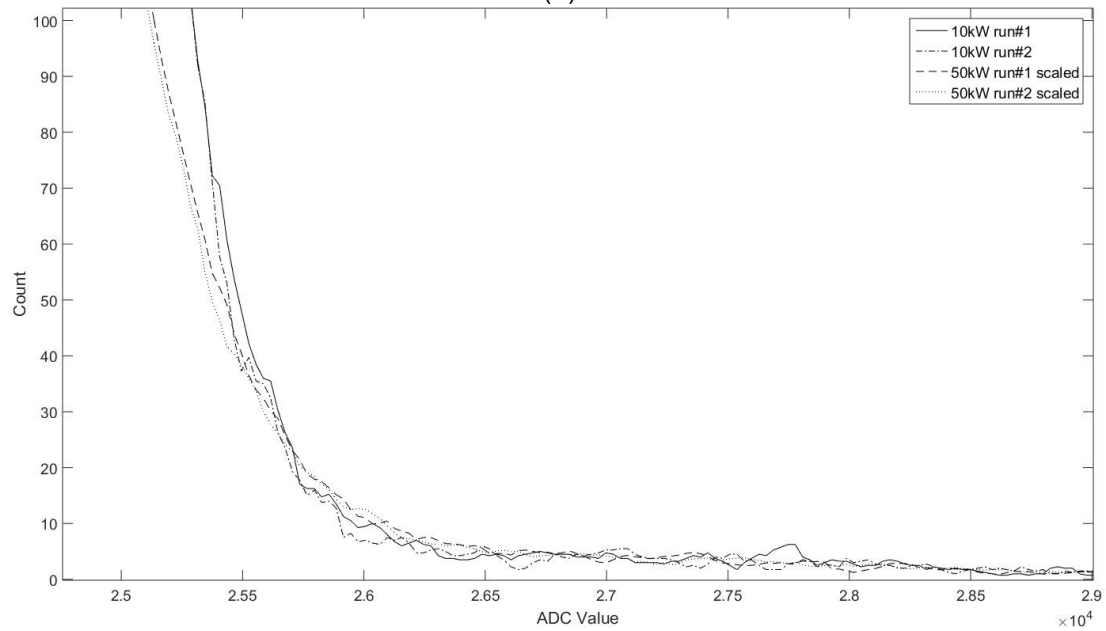


Figure 34 Reactor gamma spectrum from MCNP simulations [37]

The higher amplitude pulses in the region greater than 26000 ADC units mostly resulted from neutron events. The number of neutrons generated in the reactor is proportional to the reactor power. In other words, when the reactor power is raised from one level to another, the number of neutron pulses increases by the same factor. Figure 35 shows the pulse height distribution at 50 kW when it was scaled by 5 (divided the entire spectrum by 5) in comparison with the result at 10 kW. The higher portion of the two distributions matched very well down until the region where the gamma contribution dominated the neutron pulses. This is because the shape of the spectrum is related to the energy of the alpha particle or lithium recoil absorbed by the detector. Therefore, the spectrum in this region retains its shape regardless the reactor power. Only the number of counts is changed.



(a)



(b)

Figure 35 Comparison of the results at 10 kW and at 50 kW when scaled by a factor of 5

Because the full spectrum contained a large number of pulses from the gamma event, the total number of neutron pulses, referred to as  $n_{exp}$ , could not be derived directly by

adding all the counts from every bin in the pulse height distribution. However, we could take a look at a portion of the spectrum where only neutron pulses were present. Since the shape of the spectrum in this area should be the same regardless the power of the reactor, the total count of all the bins only from this area, referred to as  $n'_{exp}$ , stays proportional to the reactor power. For example, when the power was increased from 10 kW to 50 kW, the count at 50 kW should be 5 times greater than that at 10 kW or  $n'_{exp_{50kW}} = 5 * n'_{exp_{10kW}}$ . According to the pulse height distributions in Figure 35, the threshold was set at 26500 to eliminate the count from the gamma radiation in both power levels. The average total neutron count at 10 kW from both runs or  $n'_{exp_{10kW}}$  was equal to 273.5 while the average count at 50 kW or  $n'_{exp_{50kW}}$  was 1392.5 which was 5.09 times higher as expected.

### 5.3.3 System inherent noise

Electronic detector noise should be independent of reactor power because such noise is not generated by gamma-ray or neutron events. In order to validate this hypothesis, a number of test pulses with the same specific height were introduced to the system while the reactor was generating 10 kW and 50 kW of power. The height of the test pulses was set to 2.5 times the size of the typical neutron pulses to separate the output in response to the test pulses to a different region on the distribution plot. The exact same test setup and pulse processing algorithm in the experiment at 10 kW and 50 kW in section 5.3.2 were used in this test.

Figure 36 shows the pulse height distribution of the result at 10 kW with the test pulse generator turned on. A group of pulses in the higher region was the output resulted from

the test pulses. The pulses were centered at approximately 46200 ADC units. The noise level is generally determined by the width of the distribution. More specifically the full width at half maximum (FWHM), which is the width of the distribution measured at half of the maximum count, was approximately equal to 1500 ADC units.

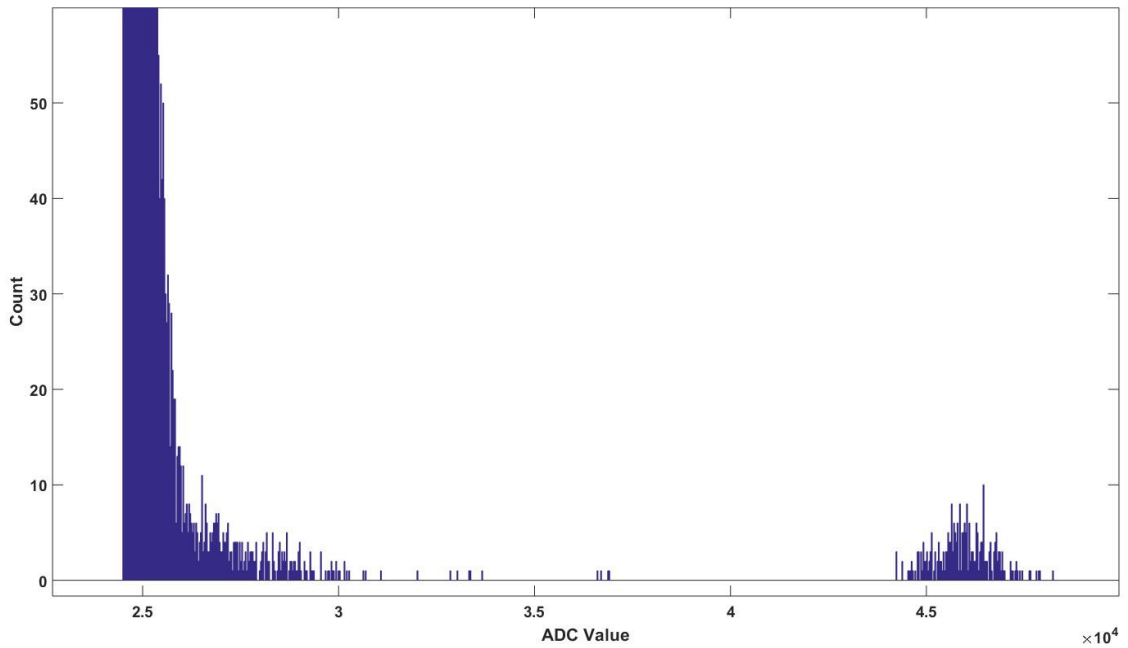


Figure 36 Pulse height distribution of the test at 10 kW with the test pulse generator turned on.

A pulse height distribution of the test at 50 kW is shown in Figure 37. The test pulse was set to the same height as the previous test at 10 kW. The test at 50 kW had a similar result. The center and the FWHM of the output from the test pulses were at approximately 46000 and 1800 ADC units, respectively.

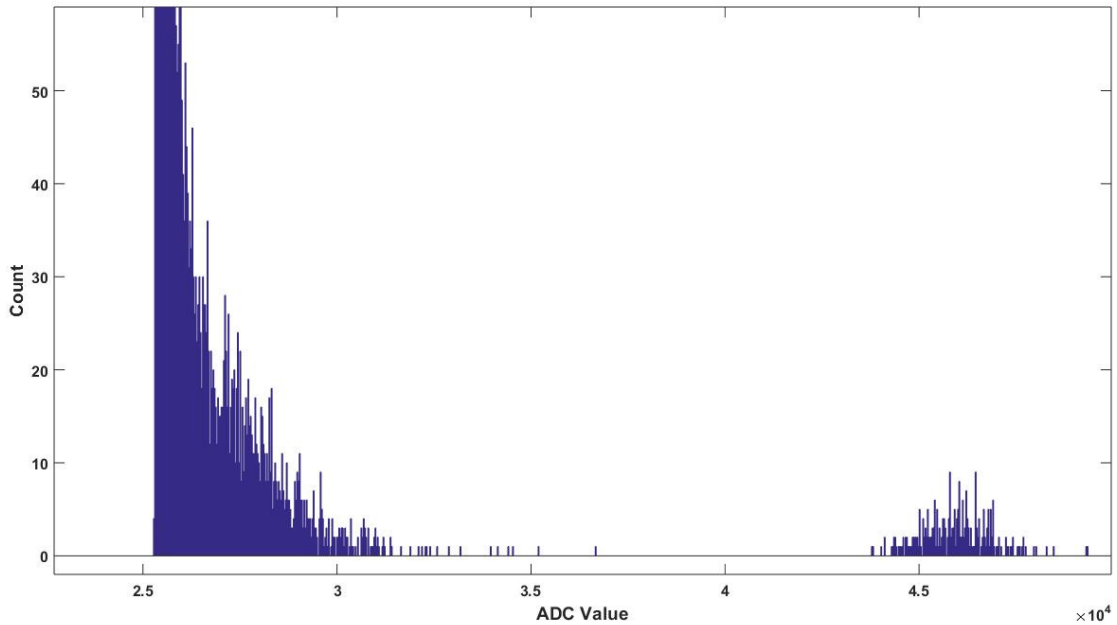


Figure 37 Pulse height distribution of the test at 50 kW with the test pulse generator turned on.

## 5.4 Conclusion

Preliminary study of the system was conducted through experiments with an alpha source and a gamma source, and through testing outside of the reactor core. Alpha particles were introduced to the detector in the direction which maximized their path length in the detector and in the direction which resembled that of the alpha particles from the neutron-induced reaction in the detector with boron. In both cases, the system was able to detect alpha particles and generate observable electric pulses.

The operation of the unlatched reset mechanism of the preamplifier was studied with a gamma source. The voltage of the preamplifier output, which rose at the rate of 50 mV/s from the leakage current, increased at the rate of 600 mV/s when the detector was

exposed to a gamma source with an activity of 217.19 GBq.

When the unlatched reset was used in the test outside of the reactor core at 10 kW reactor power, neutron events were observed on the oscilloscope. However, the preamplifier quickly reached saturation due to the strong background gamma radiation. Therefore, the preamplifier was operated in the pulse mode with the latched reset for the rest of the experiments outside of the core at the reactor power of 10 kW and 50 kW. The results showed the large number of gamma events were detected at both power levels. The number of gamma pulses increased with the reactor power. However, it did not increase by the same factor. On the other hand, the results showed that the number of neutron pulses, which had higher pulse heights, increased by a factor of 5.09 when the power was raised from 10 kW to 50 kW.

Inherent electronic noise were determined by introducing test pulses to the system. The results showed that the electronic noise was independent of the reactor power. The FWHM of the test pulses were 1500 and 1800 ADC unit at the reactor power of 10 kW and 50 kW, respectively. Some results from this chapter were presented at the American Nuclear Society (ANS) winter meeting 2015 [38].

## 6 IN-CORE MEASUREMENTS

This chapter explains the use of the detection system for acquiring measurements within the reactor core including the mechanical assembly, the installation process, the test procedure, the data analysis, and the result and discussion. The purpose of these in-core measurements was to map the neutron count at several locations, in axial direction, of the reactor core. As shown in Figure 38, each location was 25.4 mm (1") apart and referred to by number starting from 0, which was at the bottom surface of the core. The center of the reactor is at position 18 and 19, and the reactor's top surface is at position 37. Data were collected from 19 locations in the top half of the core only, starting at the top surface of the core toward the inside, since the reactor core is symmetrical. These were position 37 down to 19. The measurements were taken at low reactor power in order to reduce gamma rays produced by the reactor.

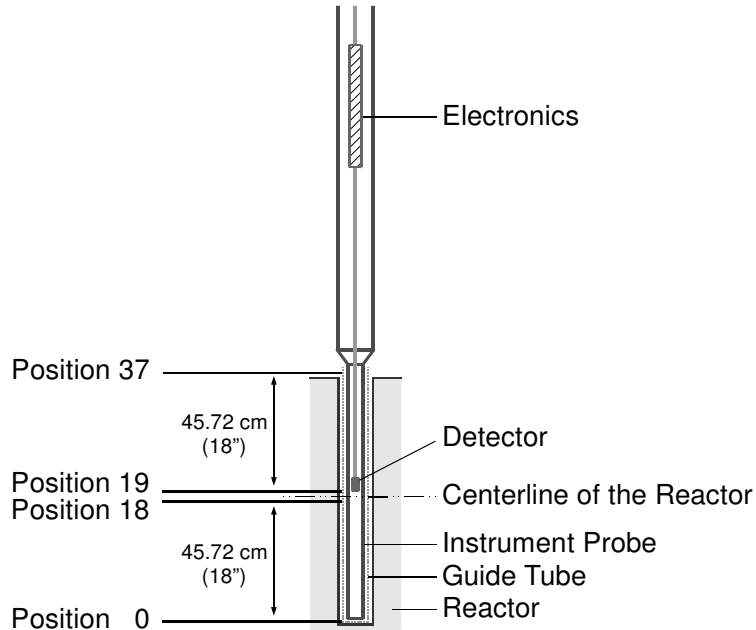


Figure 38 Reference diagram of the positions in the core (drawing is not to scale)

## 6.1 Mechanical assembly

For safety and minimal disturbance to the reactor's operation (previously discussed in section 2.1), the detector holder was inserted in the small space in between a group of four bundles of fuel and control rods. To be more specific, refer to the core diagram in Figure 2 in section 2.1, the exact location in the core was between row B and C and between column 6 and 7. The detector and the electronics were shielded in a waterproof holder consisting of two main parts: the 0.91 m (36") tip and the 9.14 m (30") long pipe.

The tip was the part that housed the detector. It was 0.91 m (36") long and made of an aluminum tube, as shown in Figure 39, with an outer and inner diameter of 8.255 mm (0.325") and 7.747 mm (0.305"), respectively. The detector was vertically centered. One end of the tube was welded shut to prevent water from leaking into the tube and the

other end was threaded to screw into another pipe section. Thread seal tape (polytetrafluoroethylene or PTFE tape) and an O-ring were used in the connection for better sealing. For the in-core measurement the tip was slid in to the guide tube installed in the reactor core. Because the detector was located at the center, when the tip section was inserted all the way down into the guide tube, the position of the detector was at position 19 in the diagram shown in Figure 38.

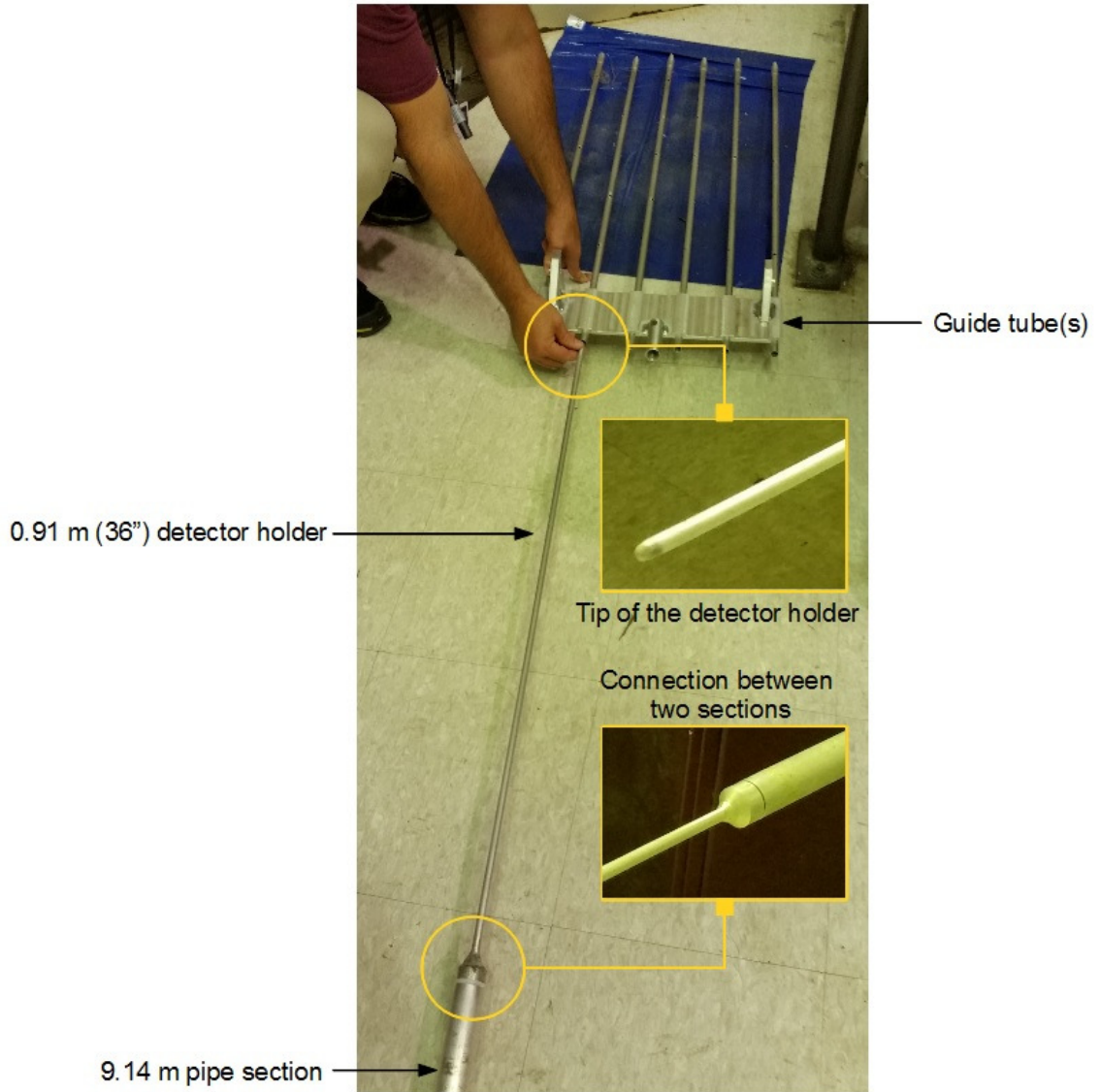


Figure 39 The 0.91 m (36") tip in which the detector was located and the guide tube (in original color)

The guide tube is also shown in Figure 39. Each prong lined up with the position of the small hole located between the row and column of the fuel and/or control rods. These were the locations available to place the detector into the core.

The 9.14 m (30') pipe was the part in which the electronics resided. It was made from the same material as the tip section. The bottom end of the pipe had an internal thread for the tip to be fastened to. This long pipe was actually composed of multiple shorter sections that were welded together. A simple pressure test was done to check for leaks before installing the instrument and putting it into the reactor pool.

To connect the electronics back to the data acquisition unit which was situated at a distant location, the cables with SubMiniature version A (SMA) connectors were used. This made the electronics detachable from the long cable and easier to install in the pipe. On the other hand, the detector output and the high voltage were hardwired to the electronics. The detector and the cable were fed to the pipe from the top side of the pipe. When it reached the correct position, the cable was secured at the top of the pipe while the electronics were free hanging inside. No other support was required. The detector was then inserted in the tip and the last step was screwing the tip to the pipe to complete the assembly process. The final product, referred to as the instrument probe, was a long waterproof aluminum pole with the detector and the electronics encapsulated. No radiation shielding of the electronics was necessary because the reactor operated at the low power during the experiment.

A few problems occurred during the assembly of the instrument probe.

- The custom-built input capacitor, shown in Figure 40, was damaged. The inner wire of the capacitor broke off when the electronics was pulled through the pipe and got stuck at one of the welding joints. The wire was replaced by a small magnet wire which positively resulted in a lower capacitance and higher charge-to-voltage gain.

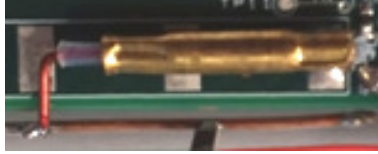


Figure 40 A custom-built input capacitor made from a small magnet wire, a Teflon insulator, and a brass tube (in original color)

- One of the welding joints on the 9.14 m (30') pipe had a leak. The detector, the electronics, and some parts of the cables were submerged under water for a few days. This caused a short circuit in the DC/DC power supply and also the reed relay of the preamp reset circuit. As a result, the unlatched mode was no longer working. All the in-core measurements were performed in pulse mode with permanent latched reset. Water trapped in the cable could also affect the measurements. Its high dielectric constant could lead to the fluctuation in cable's capacitance and resistance to ground. The cables were heated for 24 hours to eliminate as much moisture as possible.
- A minor leak was also found at the pointy end of the tip. However, because the detector was positioned at the vertical center, the slow leak should not have a big impact on the measurement.

## 6.2 Installation process

The installation of the measurement system in the reactor core was a two-step process. The guide tube was first installed in the core of the reactor. This was accomplished by lowering the tube until all the prongs were in the correct place. Figure 41 shows the photographs taken from the underwater VDO camera (a) when the guide tube was inserted into the core and (b) when it was fully installed. Figure 41(c) shows the guide

tube in which the instrument probe was to be placed.



(a)



(b)



(c)

Figure 41 Photographs showing the guide tube in the core of the detector (a) before the prong was inserted (b) the guide tube was completely installed (c) the close up of the guide tube once installed in the reactor.

The second step in the process was to insert the fully-assembled instrument probe into the guide tube at the position between columns 6 and 7 and rows B and C in the diagram in Figure 2. When the detector was at the desired axial position, the probe was

locked in place at the top. Since the detector was positioned at the center of the vertical length of the detector holder tip, when the probe was placed all the way down, the detector was at position 19 which was the lowest position in this setup and corresponded to the center position of the core. The manufacturing of the mechanical parts and the installation of the instrument was accomplished with the support of the NSC staff.

### **6.3 Test procedure**

The test at all 19 positions followed the same procedure.

#### **6.3.1 Settings**

##### *Reactor settings:*

Results from the out-of-core measurements in section 5.3.2 showed that the gamma contribution to measurements can be very high. Therefore, to lower the number of gamma pulses and possibly obtain neutron information, the reactor was operated at low power, 50 W, for the in-core experiments. However, such a low power level was very difficult to control and keep it stable for a prolonged period of time. Thus, the operating power had to be corrected over the course of the experiment by adjusting the control rods. With the correction the power still drifted by 10-20%. For example, the reactor power meter from time to time read 45 to 60 W for a nominal 50 W power. This issue had not come up in the test outside of the core as the reactor operated at much higher power at 10 kW and 50 kW.

The cooling system was shut down during the test to eliminate some noise, as discussed in section 5.3.2. It is important to note that this was possible only because the reactor was operating at very low power and for a short period of time.

*High voltage generator settings:*

The external high voltage power supply provided a voltage of  $-350$  V to the detector. During the experiment it was found that the voltage was dropped to  $-300$  V. From the experiment previously performed at UOIT in November 2014 using a detector with a similar geometry and dimensions to detector B (not included in this thesis), rise time and size of the output pulses were in the same range when the high voltage was varied from  $-300$  V to  $-500$  V. Therefore, the high voltage was not corrected. The tests at position 37 down to 24 were performed at  $-350$  V, and the tests at position 23 down to 19 were performed at  $-300$  V. This voltage drop could possibly have resulted from the wetness of the cable. An end section of the cable was wet from the water leaked into the instrument probe a few days before the measurements were taken. Wet lead and insulation could cause varied capacitance and resistance of the high voltage line and resulted in the unstable high voltage.

*PX14400D2 settings:*

The same settings used in the out-of-core measurement in Table 7 was also applied to the in-core test at all positions. The digitizer card PX14400D2 was set to RAM-buffered recording mode in which the data were taken, transferred, and stored in blocks for a total time of 30 seconds. The range of the input was  $200 \text{ mV}_{\text{p-p}}$ .

### **6.3.2 Procedure**

*Test steps:*

1. The reactor was first shut down and the cooling system was turned off to prepare for the installation of the instrument.

2. The guide tube and the fully-assembled instrument probe were installed in the reactor. To start with, the detector was positioned at position 37 before the probe was secured at the top.
3. The high voltage generator was turned on to provide the voltage of  $-350$  V to the detector. A waiting period (minutes) was required for the high voltage to stabilize.
4. The reactor started to operate. The power was brought up to 50 W.
5. The data acquisition started when the power reached the desired level. Three 30-s worth of data were recorded. The files were stored on the SSD for post-processing. As mentioned earlier during data acquisition the reactor power could increase or decrease by 10-20% since the power at low level was difficult to control and keep stable.
6. After three acquisitions were finished, the detector was moved to the next location which was one position lower.
7. Step 5 and 6 were repeated until the data from the last position, position 19, was acquired.
8. When the reactor power drifted too far from the desired level, correction was necessary. During power correction, the data acquisition was paused. It was resumed once the power was back within the acceptable range.

*Data analysis steps:*

To start with, a simple analysis was applied to the collected data to derive information about neutron flux in various locations in the core. Offline data processing followed the same methodology as the analysis of the out-of-core measurement results in section 5.3.2. The preliminary analysis ran on MATLAB and was based on the shaping amplifier output. Only one data file was processed at a time; in other words, the data collected

from different positions were processed separately. The procedure was as follows:

1. The shaped output was first passed through a 32-point running average filter to remove the high frequency noise.
2. The pulses were located and registered if they met the height and time criteria.
3. The positively identified pulses were counted based on their heights to create a pulse-height distribution.
4. The total number of detected neutron events at one location was the sum of the counts of all heights above the threshold which was set sufficiently high to eliminate as much gamma pulses as possible.

The total count from step 4 was included in the plot between the detected count and the detector's location. This plot was compared to the MCNP model of the core, performed independently by Jan Vermaak [39].

## **6.4 Results and discussion**

Figure 42 shows the pulse height distribution when the detector was located at position 37, the top surface of the reactor core. The spectrum had the same characteristics as the out-of-core spectrum shown in Figure 33. The low height pulses were from gamma events, and the pulses with pulse heights greater than approximately 28000 ADC units were neutron events. In order to support this conclusion, a measurement was taken when the reactor was shut down (0 W power). In this condition, the reactor did not generate any neutrons; however, gamma rays could still be present due to the decay of fission products and other activated material in the core. As a result, a large number of pulses were detected, as shown in a pulse height distribution in Figure 43, even though the reactor was shut down and did not generate any power.

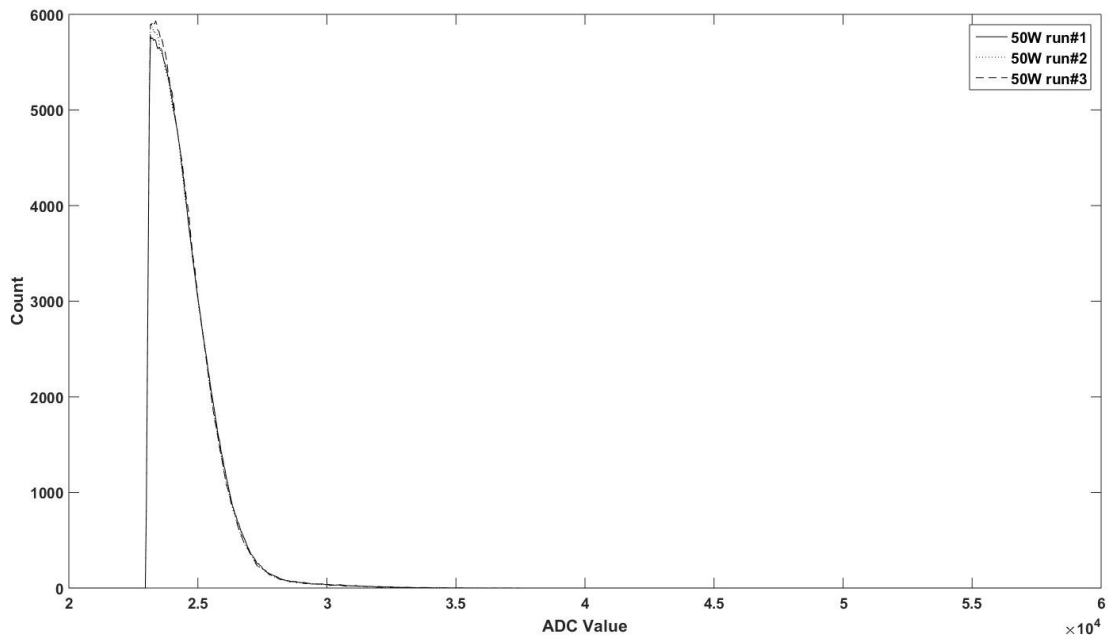


Figure 42 Pulse height distribution at 50 W power at position 37

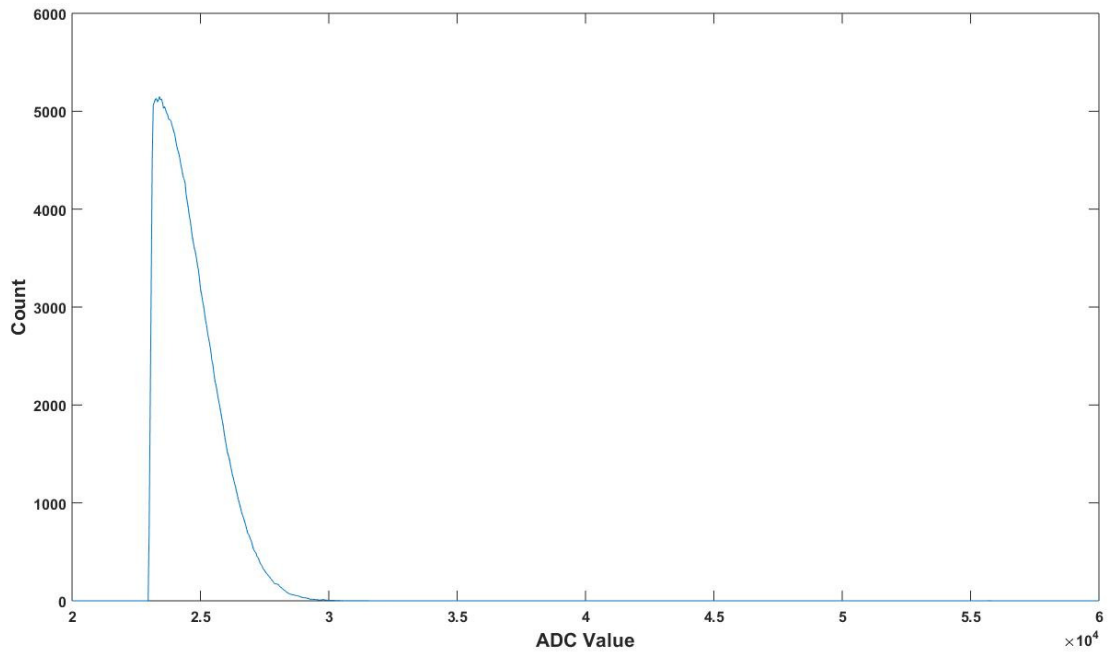
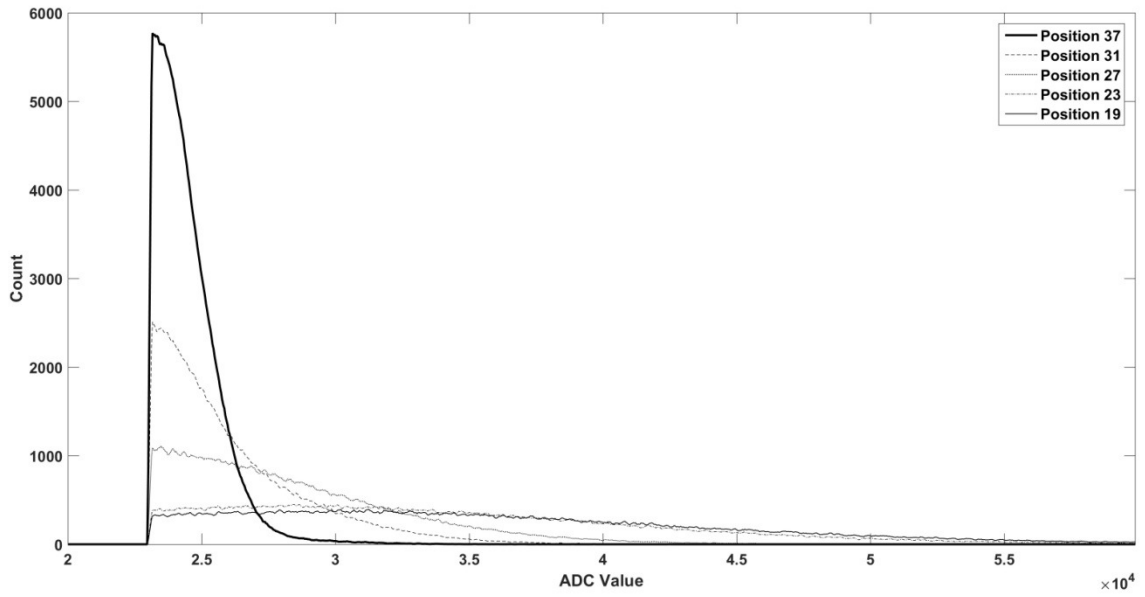
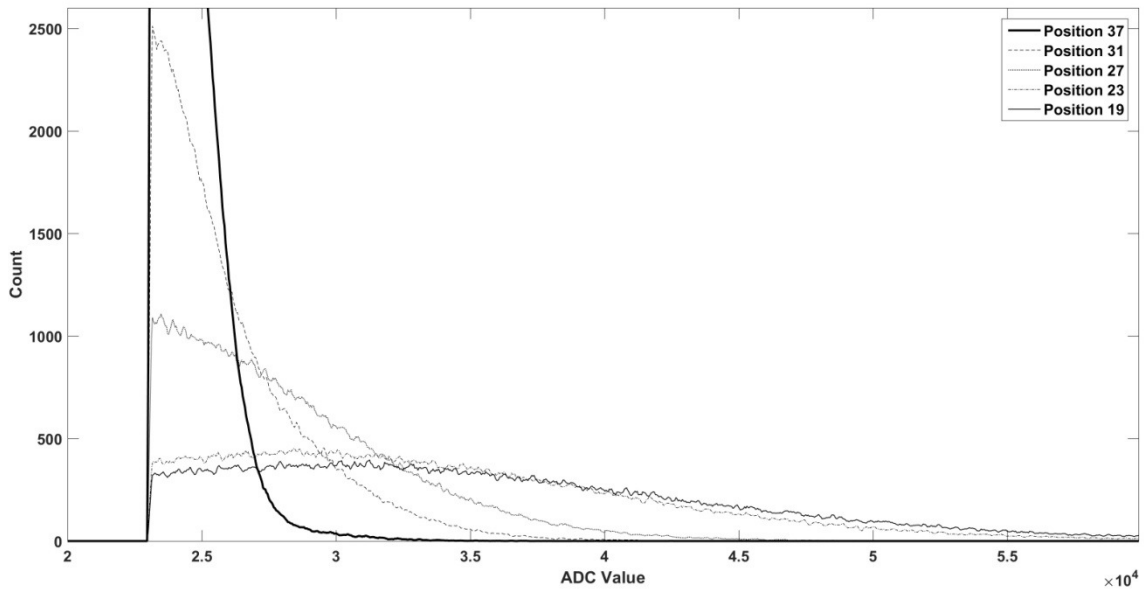


Figure 43 Pulse height distribution at 0 W power at position 37

Figure 44 shows the spectrum at 50W power at position 37 in comparison with positions 31, 27, 23, and 19. As the detector was moved to the positions further toward the center of the core, there were more gamma pulses with the higher pulse heights which led to the wider gamma peak in the spectrum. The gamma peak also had less counts. For example, the number of pulses with the height of 23000 ADC value was approximately 5800, 2400, 1100, 400, and 300 for position 37, 31, 27, 23, and 19, respectively.



(a)



(b)

Figure 44 Pulse height distribution when the detector was located at position 37, 31, 27, 23, and 19 (a) full spectrum of all positions (b) close-up for the range from 0 to 2600 pulses

When the number of pulses from every bin at each position of the detector was integrated, the total number of pulses decreased as the detector was moved closer to the center of the core, as shown in Figure 45. The relative counts on the vertical axis represent the total number of pulses with the height above 23000 ADC unit at that position normalized by the maximum count of all positions.

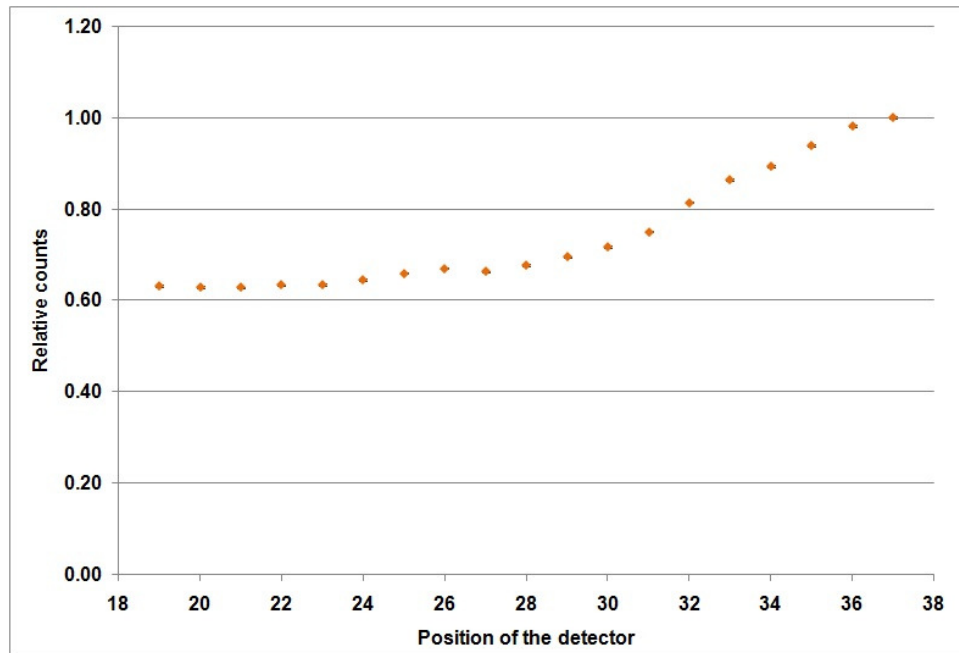


Figure 45 Plot of the number of all the pulses with the height above 23000 ADC unit versus the detector's location in the reactor core

Decrease in number of gamma pulses but increase in their pulse height when the detector was moved closer to the center of the core led to a conclusion that at the inner location the gamma flux was very high resulting in pile-up of gamma pulses. Two or more gamma pulses were recognized as one pulse with a larger pulse height. If there were many gamma pulses with a high enough pulse height, the spectrum due to gamma

events could bleed into the region of neutron pulses. Therefore, to determine neutron flux at each axial location, a threshold was set at a higher level than that used in out-of-core measurements to discriminate gamma pulses. Unlike out-of-core analysis, the spectrum could not be scaled by a specific factor to determine threshold for neutron pulses because the factor was unknown. Consequently, a few values were used in the analysis. Figure 46 shows a plot between sum of the number of pulses with a height greater than 37000, 38000, and 39000 ADC units (a threshold of 26500 ADC units was applied in the out-of-core analysis). The results were similar in all three cases. Due to the high thresholds, there were not many pulses with higher pulse heights, either from neutron events or gamma events, at the locations around the edge of the core, i.e. position 37 down to 32. On the other hand, at inner locations of the core, numbers of counts above the thresholds increased as the detector was moved toward the center. The increase in rates was very high from position 25 down to 21. These outcomes suggested a high radiation flux at the center of the core; however, a significant number of counts were still from gamma events. High thresholds excluded the peaks of the gamma pulses in the distributions from the analysis. Consequently, the results were different from ones when all the pulses were included in Figure 45.

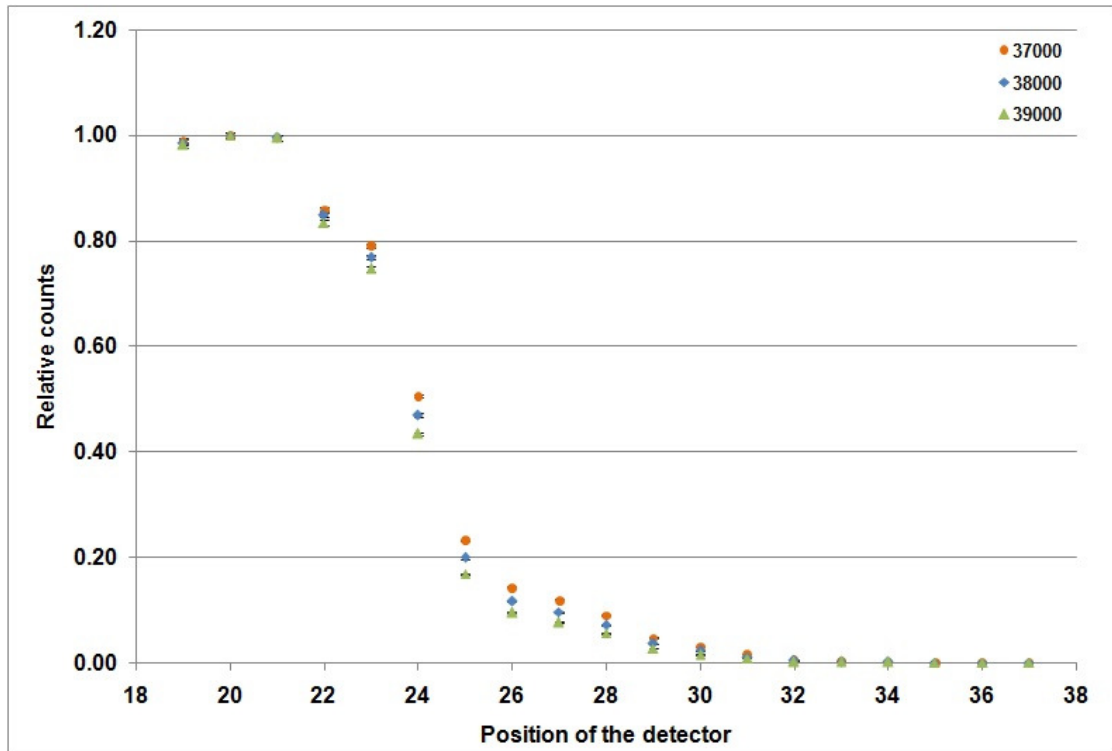


Figure 46 Plot of the number of pulses with the height above 37000, 38000, and 39000 ADC units versus the detector's location.

Experimental results were compared to the MCNP simulations performed by Jan Vermarrk [39] as shown in Figure 47. Experimental data were the number of counts above a threshold of 37000 ADC units. Results from the experiments were not in full agreement with simulations due to a large number of gamma events were included in the experimental results, especially at the position closer to the center of the core. The peak in the simulation at position 26 corresponded to the location where active fuel elements met a graphite layer in the core.

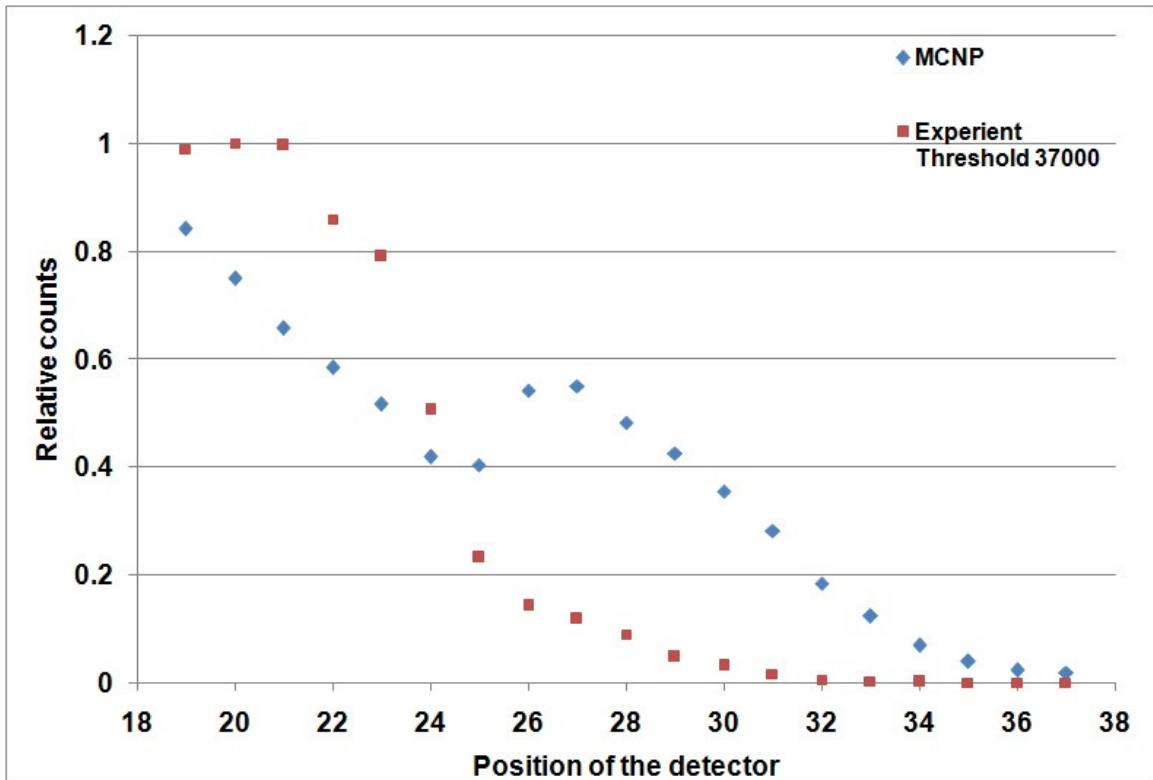


Figure 47 Plot of the number of events versus the detector’s location from experiments (square marker) and the simulation (diamond marker)

The results indicated the detector was very sensitive to high gamma flux in the reactor core. Consequently, it is difficult or not possible to identify neutron events in the spectrum unless the impact of gamma rays is reduced or characterized. An attempt to characterize shape of the pulse height distribution of the gamma pulses was made. However, the analysis method, described in Appendix B, did not prove conclusive for the current data and detector configuration.

## 6.5 Conclusion

The detection system was installed in the reactor core, and measurements were taken at 19 different axial locations from the top surface to the center of the core. There were

practical issues in the mechanical assembly of the instrument probe including the difficulty in the assembly process and repeated leaking of the aluminum holder. Modifications to the design of the holder and the connection of detector and the electronic systems are required to ease the assembly process and avoid damaging the detector and the electronic circuits.

The pulse height distribution of the measurement at the surface of the core had a similar characteristics to the out-of-core measurement results. As the detector was moved to positions closer to the center of the core, gamma pulses were found to have higher pulse height and total counts of all the pulses in the spectrum decreased. These results indicated the number of gamma pulses was very high and started to pile-up leading to lower counts but higher pulse heights. Consequently, pulses from gamma events, which was only present in the low pulse height region in the pulse height distributions of the out-of-core measurement and at positions near the surface of the core, also appeared in the same region of the spectrum as pulses from neutron events. As a result, neutron information could not be observed or derived from the spectrum.

## 7 CONCLUSIONS

The work present is the initial step in a research program that aims at measuring the thermal neutron flux during a reactor's transient operation. The system were designed, constructed, and tested with test pulses, isotopic sources, off-core radiation fields, and within the core of the TRIGA research reactor. The detection system consisted of a boron-lined ionization chamber, associated electronics, and data acquisition sub-systems. The focus of the thesis involves development of the first two components. The data acquisition and storage unit and the post-processing software are set-up in the simplest way. System's functions were tested to evaluate their performance.

An algorithm to directly analyse the digitized preamplifier signal was developed and tested with test pulses. The algorithm's variables were investigated. Since these variables could be tailored to the characteristics of the preamplifier and noise, the algorithm is expected to effectively remove microphonic noise in future experiments. An alpha source was used to test the detector's operation as an ionization chamber by using the detector without boron. The system was able to detect alpha particles travelling in similar directions as ones to be generated by boron-neutron interactions in the detector with boron. Also, alpha particles which lost their energy in the detector in the same range as maximum energy lost by ones to be generated by boron-neutron interactions were detected. A response of the preamplifier in unlatched reset mode to gamma rays was studied. As expected, the preamplifier output rose at a higher rate compared with the output when no gamma source was present. The system was tested outside the core of the reactor at 10 kW and 50 kW power. The results showed that both

gamma and neutron events increased with reactor power, and the number of neutron events were proportional to the reactor power.

System's configurations and installation and test procedure for in-core experiments were established. Measurements were taken at several axial locations in the top half of the reactor core. During this in-core trial run, problems in the design and analysis methodology were identified. Three main suggestion modifications deal with the mechanical assembly of the system, the compensation for the detected gamma signal, and an additional test to improve the analysis for better test results.

## **7.1 Mechanical parts and assembly**

Assembly and installation of the instrument probe for the in-core experiments encountered some challenges, two of which were the recurring leak of the instrument probe and damages to the electronics during assembly process. In the current system the long aluminum tube in which the electronics reside was made from multiple short pipes that were welded together and the tip section which encapsulated the detector was a narrower pipe with a welded round tip. It is critical that the casing is waterproof to protect the detector and the electronics. Although the probe was pressure tested prior to the assembly of the instrument in the pipe, leaks were found once it was placed in the reactor's pool most likely from the tiny crack of the welded tip and the joints. Harsh environment near the core may further weaken the joints.

It is recommended that in the future, a laser beam welder should be used to improve the quality of the welding especially at the tip of the detector holder. Also a helium leak test, one of the standard methods to identify very small leaks [40], should be performed after

the probe is fully assembled (with the instrument inside). If necessary the probe should be air-tight sealed and be put under pressure during the operation to keep the water out.

The current system used long cables (over 27 m) to connect the electronics back to the data acquisition unit. Only one connection was made through SMA connectors located only 0.6 m from the electronics which was difficult to be detached during the probe assembly. As a result, to install the instrument in the probe the detector and the electronics were fed through the full length of the aluminum pipe from the top end to the other end. The process then required a high amount of care and risked damaging the detector and the electronics. To ease the assembly, the connection should be easily disconnected and another connection should be made at the top of the aluminum probe. These connections should be detached during the assembly process, and cables should be pulled through the pipe from the bottom side up. This method minimizes the risk of damaging the detector and the electronics. The comparison of the current and the proposed cable connections are shown in Figure 48.

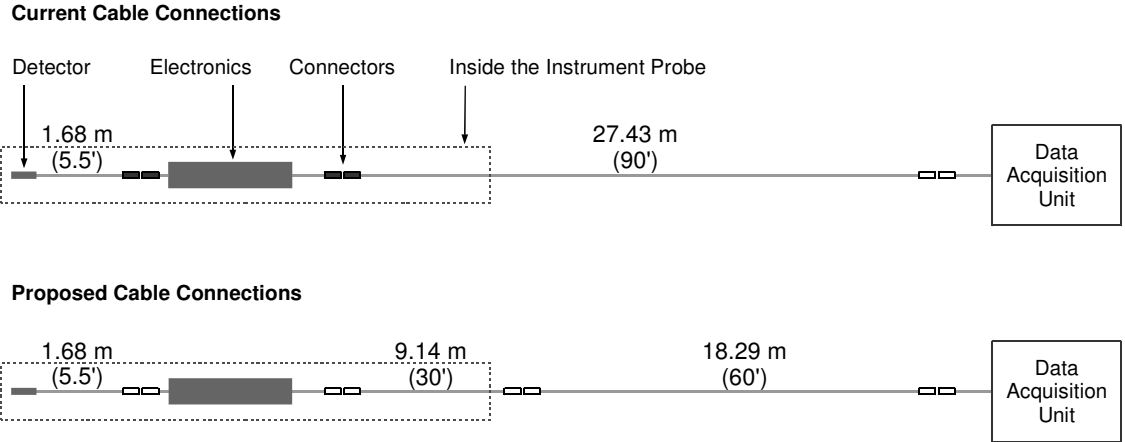


Figure 48 Current and proposed cable connections

Another minor change is to replace the hardwire connection of the high voltage line from the electronics to the detector with a connector. This allows full detachment of the detector from the electronics. Both of the changes in cable connection will make the system more convenient to install while remain easy to debug and check.

## 7.2 Gamma compensated detector

According to the results in Chapter 6, the gamma radiation present in the core was too high to derive the neutron information from the pulse height distribution. All the charges generated in the detector in this work were collected whether they were from neutron events or gamma events. A gamma compensated detector will help lower the gamma effect by subtracting the charges created by gamma events to permit the recording only of neutron information. This is especially needed when the preamplifier operates in current mode, where pulse-shape discrimination is not possible.

A gamma compensated detector should consist of two separate ionization chambers

that share the same anode wire. The two chambers should have identical geometry and material except only one of which contains boron-10 to capture thermal neutrons. The sketch of the detector is shown in Figure 49. The first chamber has the same structure as the original detector, with a small hole covered with a boron-lined copper piece. The wall of this chamber is to be connected to a negative high voltage. The two chambers share the same anode wire, which is in turn to be connected to the preamplifier. The wall of the second chamber, however, is connected to a positive high voltage, while the other detector remains connected to a negatively biased high voltage. The two chambers are to be separated by a ceramic insulation in order to keep the opposite biased walls apart. Another ceramic tube should be used at the end of the detector to align the long anode wire with the center of the detector.

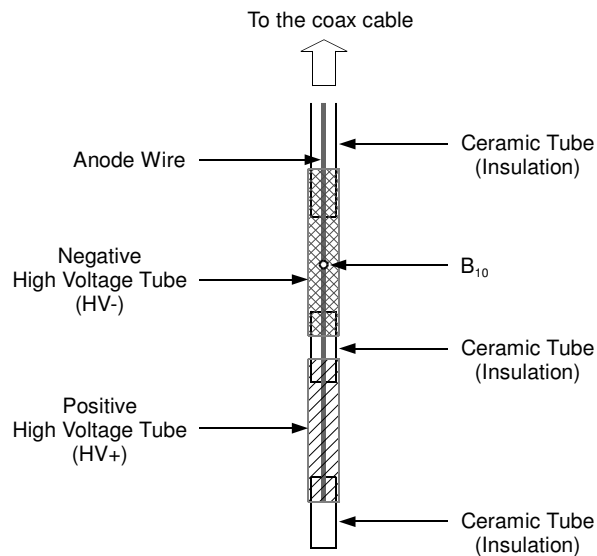


Figure 49 A sketch of a conceivable gamma compensated detector

Due to the identical geometry of the two chambers and their proximity to each other, the number of charges generated due to gamma events should be nearly equal. However, the opposite polarity of the high voltage potentials that are connected to the walls causes

electrons and negative ions to drift to the opposite electrodes. In one chamber they drift toward the anode wire, while in the other chamber they move toward the wall. Therefore, charges from gamma events cancel each other out, and only charges resulting from neutron events are collected at the anode wire.

One of the design constraints of a detector is its size, especially its diameter, since a detector is to be encapsulated in the detector holder with an inner diameter of 7.747 mm (0.305"). The proposed design has the same diameter dimension as the current detector, except that it has an additional wire carrying a positive high voltage to the second chamber. A 28 AWG wire is thin enough to fit in remaining space in the detector holder.

### **7.3 Pulse height distribution of gamma events**

As demonstrated in section 6.4, a large number of gamma pulses made it difficult to identify neutron events in the pulse height distribution. A gamma compensated detector, as discussed in section 7.2, should reduce the number of gamma pulses. In addition to a gamma compensated detector, derivation of neutron counts from a pulse height distribution would be easier if a spectrum due to gamma events of the same measurement is known. In an experiment, measurements should be taken with both detector A (without boron) and detector B (with 2-mm boron). Detector A provides information about gamma events which can be used to eliminate gamma contribution in a pulse height distribution from detector B. This method was not yet implemented. One of the reasons is that swapping the detector in the current assembly and cable connection of the instrument probe is time consuming and risks damaging the detector and the electronics.

## REFERENCES

- [1] M. Adams, “Phenomena-based Uncertainty Quantification in Predictive Coupled-Physics Reactor Simulations.” NEUP U.S. Department of Energy, Oct-2011.
- [2] J. Vermaak and A. Marvin, “Development of In-Core Detector Devices for Steady-State and Transient Measurements,” *Transactions*, vol. 113, no. 1, pp. 1061–1064, Oct. 2015.
- [3] “About TRIGA®,” *General Atomics*. [Online]. Available: [www.ga.com/about-triga](http://www.ga.com/about-triga). [Accessed: 11-Aug-2014].
- [4] “TRIGA Reactor | The Nuclear Science Center at Texas A&M University.” [Online]. Available: <http://nsc.tamu.edu/products-and-services/triga-reactor/>. [Accessed: 08-Feb-2016].
- [5] “Research Capabilities | The Nuclear Science Center at Texas A&M University.” [Online]. Available: <http://nsc.tamu.edu/products-and-services/research-capabilities/>. [Accessed: 08-Feb-2016].
- [6] J. Vermaak, private communication, May-2015.
- [7] J. Vermaak, S. Pongpun, M. Adams, and T. Conroy, “In-Core Neutron Detectors for Characterizing High Temporal-Resolution Reactor Transients,” *Proceedings of PHYSOR 2016*, to be published.
- [8] G. F. Knoll, *Radiation Detection and Measurement*, 4th ed. John Wiley & Sons, 2010.
- [9] M. B. Chadwick, M. Herman, P. Obložinský, M. E. Dunn, Y. Danon, A. C. Kahler, D. L. Smith, B. Pritychenko, G. Arbanas, R. Arcilla, R. Brewer, D. A. Brown, R. Capote, A. D. Carlson, Y. S. Cho, H. Derrien, K. Guber, G. M. Hale, S. Hoblit, S. Holloway, T. D. Johnson, T. Kawano, B. C. Kiedrowski, H. Kim, S. Kunieda, N. M. Larson, L.

- Leal, J. P. Lestone, R. C. Little, E. A. McCutchan, R. E. MacFarlane, M. MacInnes, C. M. Mattoon, R. D. McKnight, S. F. Mughabghab, G. P. A. Nobre, G. Palmiotti, A. Palumbo, M. T. Pigni, V. G. Pronyaev, R. O. Sayer, A. A. Sonzogni, N. C. Summers, P. Talou, I. J. Thompson, A. Trkov, R. L. Vogt, S. C. van der Marck, A. Wallner, M. C. White, D. Wiarda, and P. G. Young, "ENDF/B-VII.1 Nuclear Data for Science and Technology: Cross Sections, Covariances, Fission Product Yields and Decay Data," *Nucl. Data Sheets*, vol. 112, no. 12, pp. 2887 – 2996, 2011.
- [10] V. F. Sears, "Neutron scattering lengths and cross sections," *Neutron News*, vol. 3, no. 3, pp. 29–37, 1992.
- [11] T. Crane and M. Baker, "Neutron detectors," in *Passive Nondestructive Assay of Nuclear Materials*, Washington, DC: Nuclear Regulatory Commission, Washington, DC (United States). Office of Nuclear Regulatory Research, 1991, pp. 379–406.
- [12] E. Hussein, *Handbook on Radiation Probing, Gauging, Imaging and Analysis - Volume I: Basics and techniques*. Dordrecht London: Kluwer Academic, 2003.
- [13] "MPPC and MPPC module for precision measurement." Hamamatsu Photonics K.K., Mar-2016.
- [14] "MPPC (SiPM) | Hamamatsu Photonics," 25-May-2016. [Online]. Available: <http://www.hamamatsu.com/us/en/product/category/3100/4004/4113/index.html>. [Accessed: 25-May-2016].
- [15] "Fission Chambers for In-Core Use | PHOTONIS," 08-Feb-2016. [Online]. Available: <https://www.photonis.com/en/product/fission-chambers-core-use>. [Accessed: 08-Feb-2016].
- [16] M. F. Ohmes, A. S. M. S. Ahmed, R. E. Ortiz, J. K. Shultis, and D. S. McGregor, "Micro-Pocket Fission Detector (MPFD) Performance Characteristics," in *IEEE Nuclear Science Symposium*, 2006.

- [17] M. F. Ohmes, “Micro-Pocket Fission Detector (MPFD) Development for the Kansas State University TRIGA Mark-II Nuclear Reactor,” Kansas State University, 2006.
- [18] “Introduction to Amplifiers.” [Online]. Available: <http://www.ortec-online.com/Products-Solutions/Modular-Electronic-Instruments-Amplifiers.aspx>. [Accessed: 10-Feb-2016].
- [19] *DOE Fundamentals Handbook Nuclear Physics and Reactor Theory*, vol. 1, 2 vols. Washington, D.C.: U.S. Department of Energy, 1993.
- [20] S. Zimmermann, “Active microphonic noise cancellation in radiation detectors,” *Nucl. Instrum. Methods Phys. Res. Sect. Accel. Spectrometers Detect. Assoc. Equip.*, vol. 729, pp. 404 – 409, 2013.
- [21] M. K. Schultz, R. M. Keyser, R. C. Trammell, and D. L. Upp, “Improvement of spectral resolution in the presence of periodic noise and microphonics for hyper-pure germanium detector gamma-ray spectrometry using a new digital filter,” *J. Radioanal. Nucl. Chem.*, vol. 271, no. 1, pp. 101–106, 2007.
- [22] J. L. Lacy, A. Athanasiades, N. N. Shehad, R. A. Austin, and C. S. Martin, “Novel neutron detector for high rate imaging applications,” in *Nuclear Science Symposium Conference Record, 2002 IEEE*, 2002, vol. 1, pp. 392–396 vol.1.
- [23] W. J. Gordon, “Analysis of Microphonic Noise Genesis and Mitigation in a Boron Carbide Detector System,” Texas A&M University, 2015.
- [24] *Radiological Health Handbook*. Washington, DC: U.S. Department of Health, Education, and Welfare, 1970.
- [25] J. Vermaak, “Detector Spectrum.”, private communication, Sep-2015.
- [26] B. Bylsma, D. Cady, A. Celik, L. S. Durkin, J. Gilmore, J. Haley, V. Khotilovich, S. Lakdawala, J. Liu, M. Matveev, B. P. Padley, J. Roberts, J. Roe, A. Safonov, I. Suarez, D. Wood, and I. Zawisza, “Radiation testing of electronics for the {CMS}

- endcap muon system,” *Nucl. Instrum. Methods Phys. Res. Sect. Accel. Spectrometers Detect. Assoc. Equip.*, vol. 698, pp. 242 – 248, 2013.
- [27] D. A. Landis, F. S. Goulding, R. H. Pehl, and J. T. Walto, “Pulsed Feedback Techniques for Semiconductor Detector Radiation Spectrometers,” *Nucl. Sci. IEEE Trans. On*, vol. 18, no. 1, pp. 115–124, Feb. 1971.
- [28] D. A. Landis, C. P. Cork, N. W. Madden, and F. S. Goulding, “Transistor Reset Preamplifier for High Rate High Resolution Spectroscopy,” *Nucl. Sci. IEEE Trans. On*, vol. 29, no. 1, pp. 619–624, Feb. 1982.
- [29] T. Straume, L. Braby, T. Borak, T. Lusby, D. Warner, and D. Perez-Nunez, “Compact Tissue-equivalent Proportional Counter for Deep Space Human Missions,” *Health Phys.*, vol. 109, no. 4, pp. 277–283, Oct. 2015.
- [30] J. H. McClellan, R. W. Schafer, and M. A. Yoder, *DSP First*, 2nd ed. Prentice Hall, 2015.
- [31] “Product Information Sheet PX14400D2.” DynamicSignals LLC, 29-May-2013.
- [32] J. Lawley, “Understanding Performance of PCI Express Systems.” Xilinx, 28-Oct-2014.
- [33] “Samsung SSD 850 PRO.” Samsung Electronics America, Inc., 2014.
- [34] “Constellation ES.3 Serial ATA Product Manual.” Seagate Technology LLC, 14-Jan-2014.
- [35] G. R. Goslin, “A guide to using field programmable gate arrays (FPGAs) for application-specific digital signal processing performance,” in *SPIE 2914*, 1996, pp. 321–331.
- [36] J. Vermaak, private communication, Feb-2016.
- [37] J. Vermaak, “Investigation Report: In-core detector Physics Simulations.”, unpublished.

- [38] S. Pongpun, M. L. Adams, and T. J. Conroy, "In-Core Neutron Measurement System for Pulsed TRIGA Reactor Experiments," *Transactions*, vol. 113, no. 1, pp. 190–193, Oct. 2015.
- [39] J. Vermaak, "MCNP simulation of in-core neutron and gamma fluxes.", private communication, Sep-2015.
- [40] "Helium or Air? Leak Testing Realities, Economics and Opportunities." [Online]. Available: <http://www.qualitymag.com/articles/91438-helium-or-air-leak-testing-realities-economics-and-opportunities>. [Accessed: 25-Feb-2016].

## APPENDIX A: Analysis of shaping amplifier output

Analysis of the output of the shaping amplifier consists of three steps:

Step 1: Filter the shaped output with a running average filter

Considering the original signal of the shaping amplifier in Figure 50(a), the signal contains high frequency noise causing the small variation in the voltage which needs to be eliminated or reduced before further processed. A running average filter was used as a low-pass filter which will smooth out the signal. Figure 50(b) shows an example of the same shaped output when using an 8-point running average filter. This process prevented identifying multiple peaks for a single pulse in the peak finding algorithm in the next step.

Step 2: Identify the pulse

A pulse was positively identified if it complies with two following criteria:

- Minimum pulse height. The height of the pulse must be higher than a threshold set to discriminate against noise. The threshold level was adjustable to match the varied noise level in each experiment.
- Minimum time separation between two peaks. To be recognized, a pulse must have a certain separation from the adjacent pulses. This requirement was to avoid registering a single pulse more than once typically due to a small spike in the signal even though the smoothing filter was applied earlier. Because the current shaping amplifier had a 10- $\mu$ s time constant, a second pulse was discarded if it occurred less than 30  $\mu$ s after the previous positively identified pulse.

In Figure 50(c) the downward triangles point at the pulses that fall under the criteria above. The small pulses or ones that were too close to the previous one are not considered as a positive pulse; therefore, they were excluded from further pulse processing.

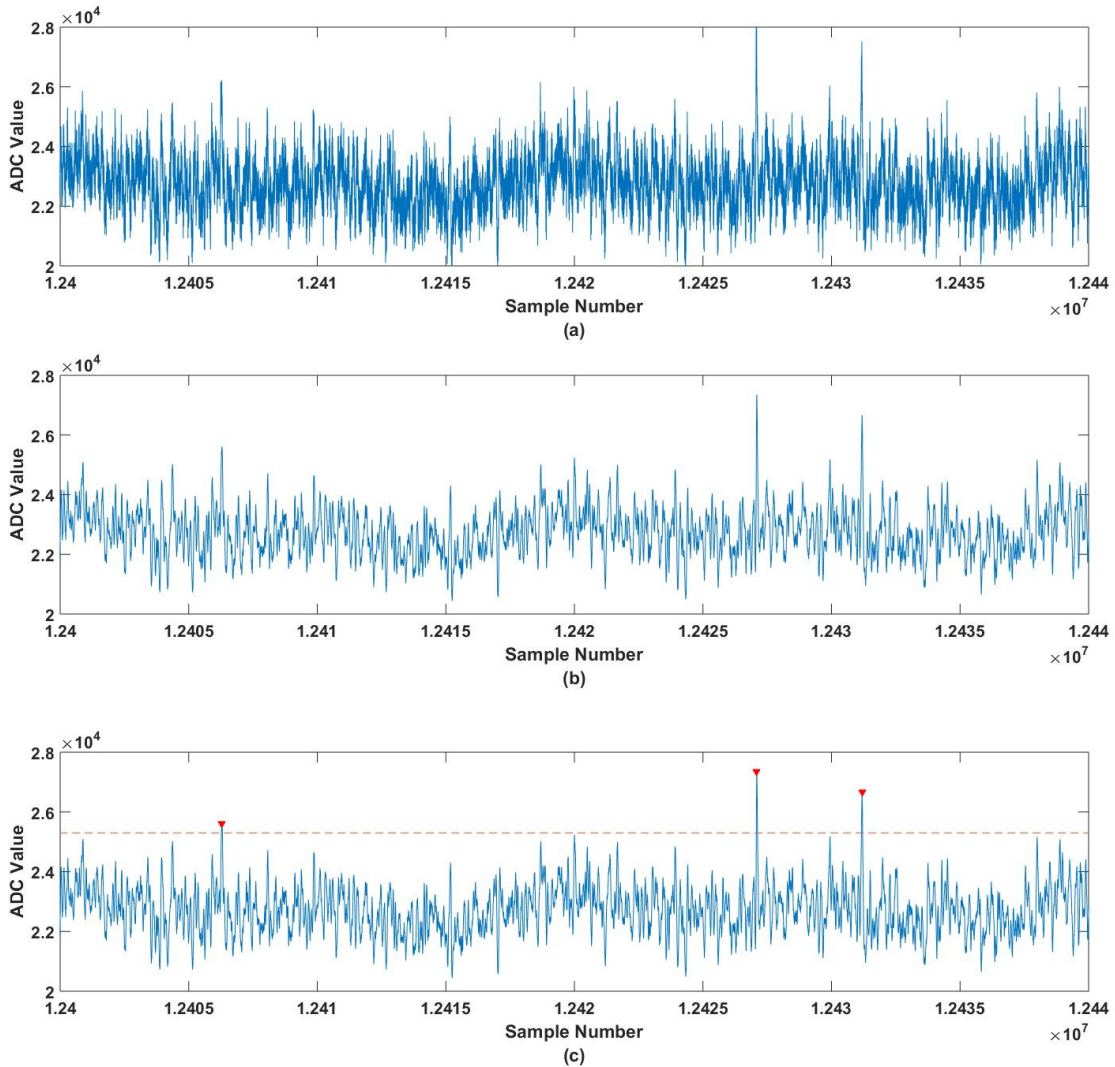


Figure 50 The shaping amplifier output (a) raw data taken at 1 MHz (b) output with the running average (c) peak identification on the output from (b)

Step 3: Create a spectrum or calculate the total count

A pulse-height spectrum is a distribution plot showing the number of pulses or the relative counts over a range of their amplitudes. It was created similar to the method that a multichannel analyzer uses. A range of pulse height was divided into a fixed number of bins, which was 1000 bins in this work. Each of the identified pulses from the previous step added a count to the bin that corresponded to its height. Because the height of the pulse is directly proportional to the amount of energy deposited in the detector by the secondary particles generated from a boron-neutron interaction, the spectrum gives a very useful piece of information in the study of the detector response. The shaping amplifier output in the previous example (Figure 50(a)) results in a spectrum illustrated in Figure 51.

The total count is the area under the spectrum or the sum of counts in all of the bins that have pulse height above the set threshold. This number is used to calculate the reaction rate.

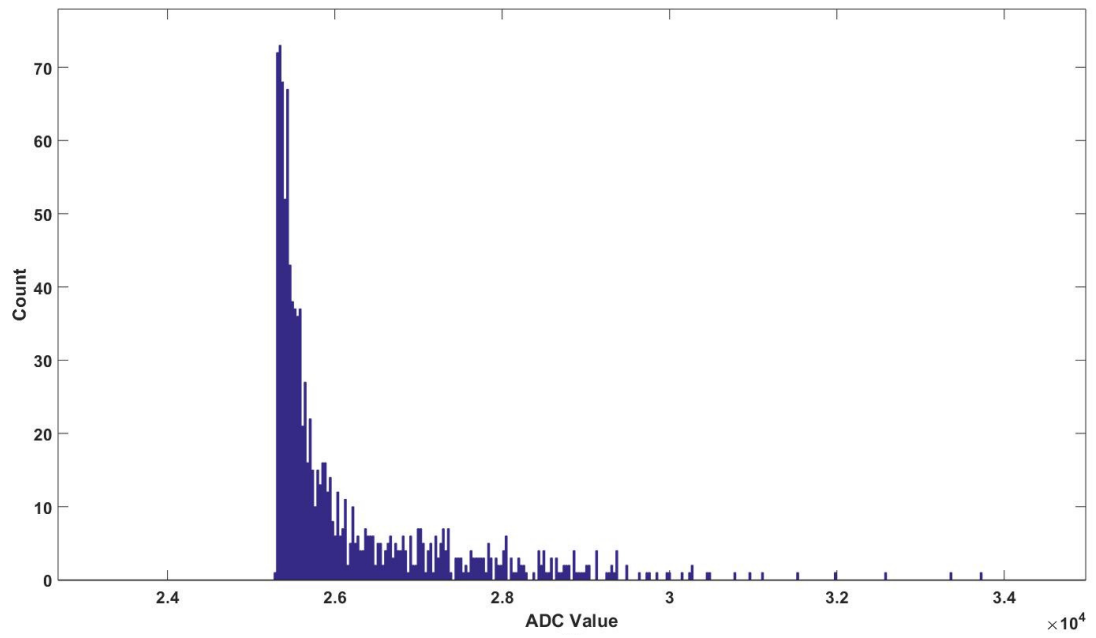


Figure 51 The spectrum of the shaping amplifier output

## APPENDIX B: Characterizing pulse height distribution of gamma events

Analysis of in-core measurements in section 6.4 showed that a large number of pulses from gamma rays dominated the pulse height distributions. Neutron events could not be identified in these distributions. This section discusses an additional analysis method to estimate a shape of the distributions of gamma events in an attempt to derive neutron information.

The spectrum of the in-core measurements, as shown in Figure 44, shows that the distribution of the gamma pulses in the low amplitude area tends to have a shape of a partial Gaussian distribution. These distinct characteristics can be made useful in the analysis. If we know or can estimate the shape of the distribution, it is possible to strip the gamma pulses off the spectrum. The equation of the Gaussian function (normalized) is

$$f(x) = ae^{-\frac{(x-b)^2}{2c^2}}$$

where  $a = \frac{1}{\sigma\sqrt{2\pi}}$ ,  $b = \mu$ , and  $c = \sigma$ . The parameters  $\mu$  and  $\sigma$  refer to expected value and standard deviation, respectively. The expected value determines the center of the peak of the distribution, and the standard deviation affects the width of the curve. Because  $a$  is a reciprocal of the parameter  $\sigma$  multiplied by a constant, the Gaussian function essentially depends on two variables:  $\mu$  and  $\sigma$ . With the proper values for  $\mu$  and for  $\sigma$  a Gaussian function is used as an estimate for the gamma pulses in the spectrum. The anomaly in the spectrum departing from the Gaussian estimate is consequently the

neutron pulses. Figure 52 shows the pulse height distribution of the in-core measurement at position 27 overlaid with the Gaussian function. Note that the variables of the function may not yet be the best values in data fitting.

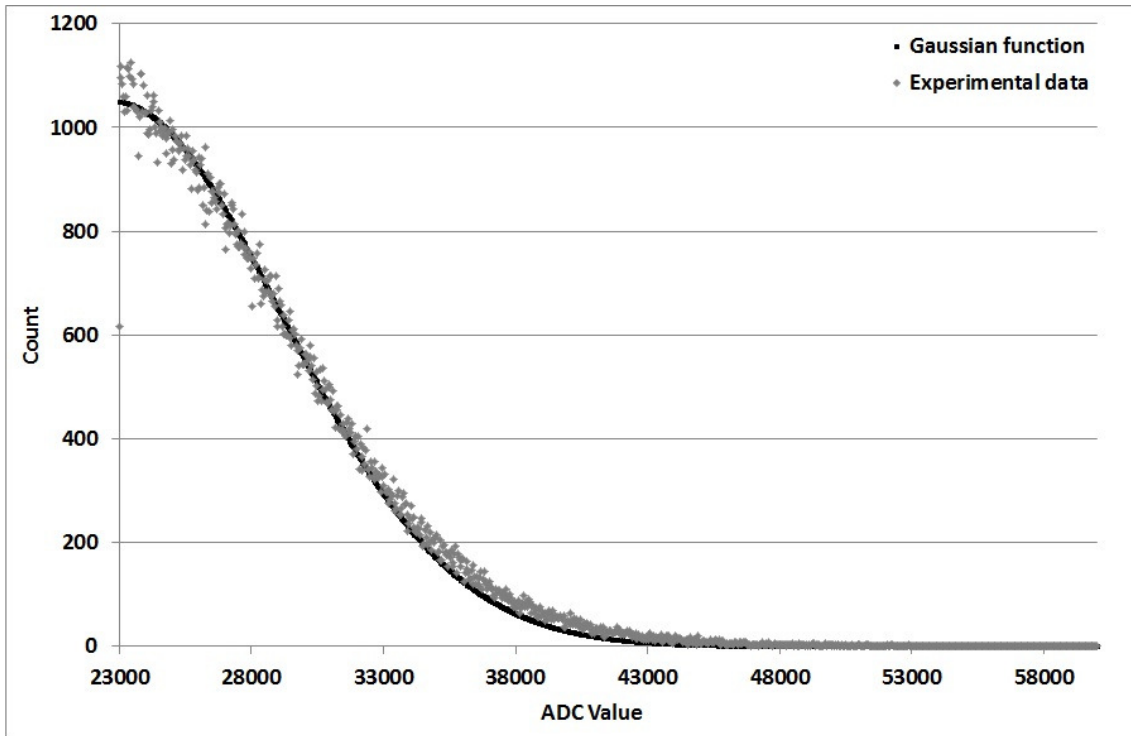


Figure 52 A Gaussian function overlaid on the top of the spectrum of the in-core measurement at position 27

The proposed analysis method is then as follows:

1. The first step in the analysis is to find a Gaussian function which fits the spectrum the best. The function depends on three variables: the expected value, the standard deviation, and the normalization gain. To choose the values that will give the best fit to the spectrum, the simple regression and the least squares method can be used to monitor the fit.

- To get the neutron information, the Gaussian function is subtracted from the spectrum. The result of the subtraction in the previous example in Figure 52 above is shown in Figure 53.

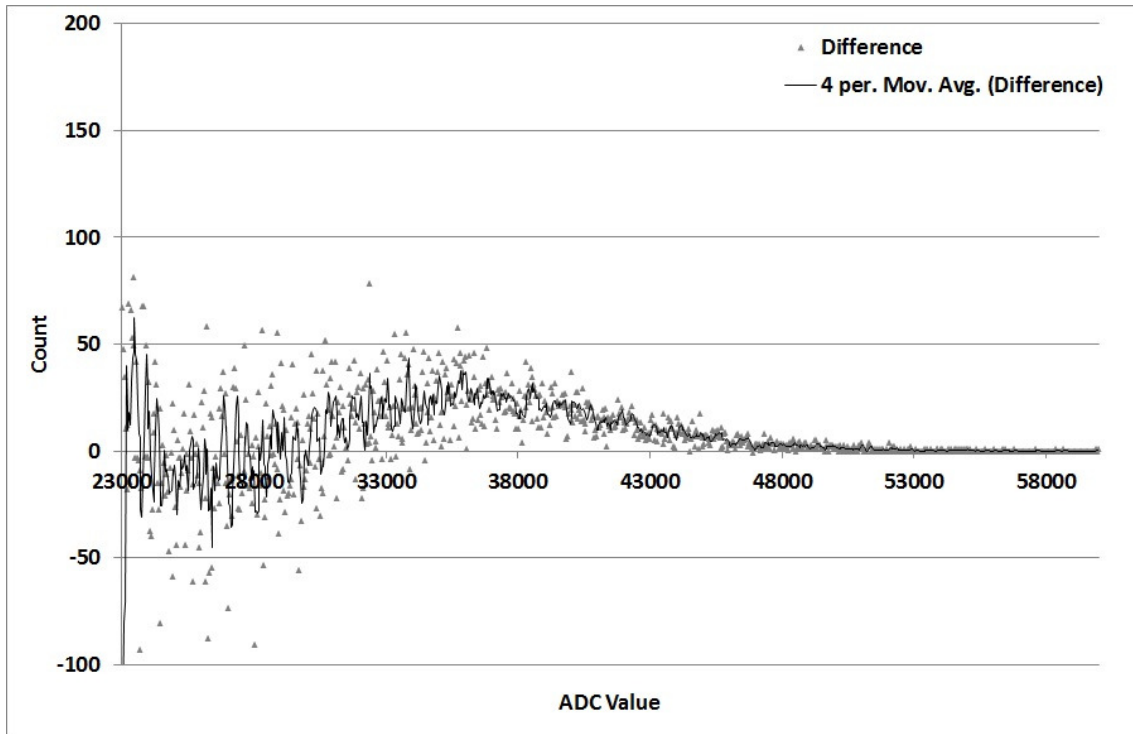


Figure 53 The spectrum at position 27 after the Gaussian function is subtracted off.

For a simple analysis or a quick check of the system, the number of neutron pulses can be calculated by adding the resulting differences of all pulse height intervals similar to the analysis in the previous chapters. Any negative difference will be adjusted to the value of zero. Nonetheless the data can be further processed to obtain more detailed information about the number of detected neutrons.

- To find the total counts from the experiment  $n_{exp}$ , instead of using the number of

pulses from all the bins directly, the distinct point in the spectrum can be used in the calculation. Consider the spectrum of the detector from the MCNP simulation in Figure 54, the total counts from the simulation, referred to as  $n_{sim}$ , is the sum of all the counts. If the low amplitude pulses are excluded, the shape of the spectrum looks like a trapezoid. The distinct point in the spectrum (point A) is the crossing point between the approximate lines of the top base side (line A) and of the lateral side (line B).

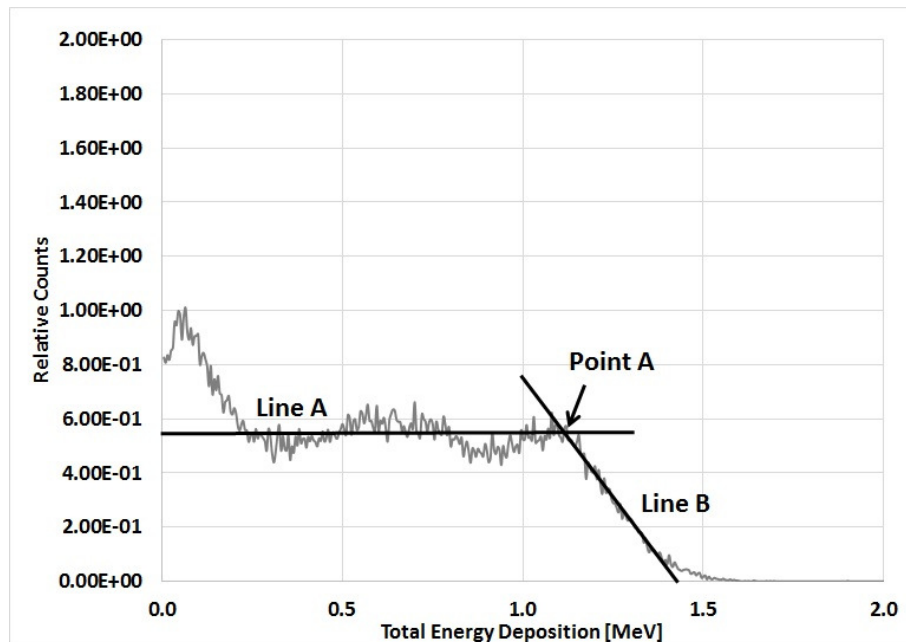


Figure 54 The spectrum of the detector from the MCNP simulation. The shape is close to a trapezoid. Lines A and B are the approximation of the top side and the lateral side of the trapezoid, respectively.

The spectrum is then simplified to a rectangular shape which has point A as a reference corner. The estimate of the total counts in the simulated spectrum, referred to as  $n'_{sim}$ , is now the product of the number of counts at point A (or the y value) and the number of

bins whose amplitude is lower than or equal to the x value of point A. Knowing  $n_{sim}$  and  $n'_{sim}$ , we can find the ratio of the estimate count to the actual count or  $R_{sim} = \frac{n'_{sim}}{n_{sim}}$ .

4. The same process can be applied to the experimental data. The ratio of the estimate count to the actual count or  $R_{exp}$  is equal to  $\frac{n'_{exp}}{n_{exp}}$ . Because this ratio should be equal to one derived from the simulation, the total counts from the experiment  $n_{exp}$  can be calculated.

$$\frac{n'_{exp}}{n_{exp}} = R_{exp} = R_{sim} = \frac{n'_{sim}}{n_{sim}}$$

Therefore,

$$n_{exp} = \frac{n_{sim}}{n'_{sim}} * n'_{exp} = \frac{1}{R_{sim}} * n'_{exp} \tag{B.1}$$

5. The next step in the analysis is to determine the estimated number of the neutron pulses or  $n'_{exp}$  from the spectrum after the gamma pulses is removed. Point A in the spectrum from the experiment is first to identified as it will be used as a reference point. Similarly, this point is the crossing point between the flat line and the declining slope of the spectrum. For example, point A in the previous example is shown in Figure 55.

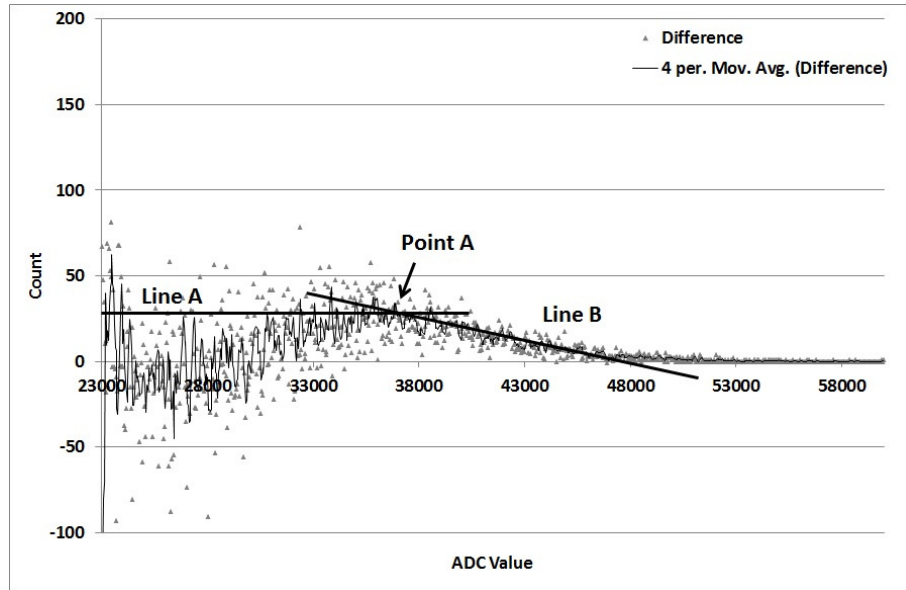


Figure 55 The reference point (point A) which is used in the calculation of  $n'_{exp}$ .

6. The total number of neutron pulses detected by the system or  $n_{exp}$  is found by using Equation (B.1).

This proposed analysis methodology has not yet been applied to the data. Gamma contribution in the current dataset was so large that determining accuracy of this technique was not yet possible. Further studies are required, especially in step 1 and 2, preferably on a new set of data taken from a gamma compensated detector previously described in section 7.2 in order to determine accuracy and usefulness of the analysis method in improving the result of in-core experiments.